University of
Strathclyde
Glasgow

# Development of a Rubidium Spin Exchange Relaxation Free Magnetometer

**Edward Irwin**

Experimental Quantum Optics and Photonics

Department of Physics

May 8, 2024

*Submitted in partial fulfillment for the degree of Doctor of Philosophy*

# Declaration

This thesis is the result of the author's original research. It has been composed by the author and has not been previously submitted for examination which has led to the award of a degree.

Edward Irwin

May 8, 2024

# Acknowledgements

Looking back at my time as a PhD student, I'd like to take this opportunity to thank those that invested time and energy in supporting me during this period of my life.

To my supervisors, Paul Griffin and Erling Riis. Griff, for bearing with me and my grammar for so long, but also for your help and guidance, not just in writing my thesis, but throughout my PhD. Erling, for your casual nuggets of wisdom that made so many issues seem so trivial.

To the SERF team: Carolyn O'Dwyer, Marcin Mrozowski and Rachel Dawson. For not only sharing a lab, but an office as well for three years. Our chats, hours at the whiteboard and on Zoom, bouncing ideas of each other and constant laughs had a profound effect on my time and research as a PhD student. It would be amiss not to mention Stuart Ingelby for his technical and theoretical support as well as the rest of the magnetometry group.

To my viva committee, Antonio Hurtado and Fedja Oručević, for a relaxed, enjoyable and interesting discussion as well feedback on my research.

Lastly, to all those that supported me outside of university, my friends and family, for time and time again asking ”so when do you finish uni?”, I knew it meant you cared. With a special mention to my colleagues at No. 81, for always being around (not that you could go anywhere else) for good food, drinks and a PowerPoint or two.

In memory of Mr B. Smalls

# Abstract

This thesis describes the design, construction and optimisation of a rubidium spin exchange relaxation free magnetometer using only a single beam. The experiment is used to look at high bandwidth sensors which will ultimately inform a more compact version used for biomagnetic field detection.

The optimisation of the sensor is discussed in detail highlighting the battle between magnetometry cell temperature, laser power and laser detuning, but also the effects the modulation parameters can have on the sensitivity. Two detection methods are used in this thesis: absorption and optical rotation. The differences in how these two methods operate are highlighted and how these differences affect the final result in the sensitivity. With both of the these methods reaching equal sensitivities above 10 Hz, the choice was made to progress further with the absorptive detection method due to its superior sensitivity in the lower frequency range.

Limitations of the experimental setup are discussed with them being reached in various components. The limiting noise sources are thought to be the DAQ unit and vibrations introduced by the shield. A sensitivity of 35 $\mathrm{fT}/\sqrt{\mathrm{Hz}}$ with a bandwidth that extends out to 420 Hz is achieved, while clear areas for improvement are highlighted. Overcoming some of these limitations ultimately lead to a sensor with an improved noise performance of sub 20 $\mathrm{fT}/\sqrt{\mathrm{Hz}}$. It is pointed out that the Johnson noise of the mu-metal shield is not far below the sensitivity reached here.

# Publications

- R Dawson, C O'Dwyer, M S Mrozowski, E Irwin, J P McGilligan, D P Burt, D Hunter, S Ingleby, P F Griffin, and E Riis. Portable Single-Beam Caesium Zero-Field Magnetometer for Biomagnetic Sensing. *Journal of Optical Microsystems*, **3(04)**:044501, (2023)
- R Dawson, C O'Dwyer, E Irwin, M S Mrozowski, D Hunter, S Ingleby, E Riis, and P F Griffin. Automated Machine Learning Strategies for Multi-Parameter Optimisation of a Caesium-Based Portable Zero-Field Magnetometer. *Sensors*, **23(8)**:4007, (2023)

# Contents

# Chapter 1

# Introduction

Within the animal kingdom magnetoreception has been used for directional purposes in migratory animals for millions of years. The migrations were first recorded by the Ancient Greeks such as Aristotle and Homer. Migratory animals included fish, reptiles and birds where the exact magnetoreceptive process happens is still unclear [1]. Humans have been taking advantage of the phenomenon of Earth's magnetic field over the past few thousand years for directional purposes also. Compasses were first used in the Qin dynasty in China (221 - 206 BCE) [2]. Early compasses were created with the use of lodestones suspended by silk threads. These early compasses were known to align to the magnetic pole. The first recorded proposal that the Earth produced a magnetic field was not until William Gilbert described this in his work ”De Magnete” in 1600 [3, 4]. Over 200 years later Carl Fredreich Gauss measured the strength of the Earth's field in 1832 [5]. During the same period contributions to the field from physicists such as Charles Coulomb, Hans Christian Oersted, André-Marie Ampère and Michael Faraday can not be overlooked. These discoveries include the force of attraction and repulsion between charged bodies by Coulomb [6, 4]. Later, Oersted showed that electric current in wires causes a nearby needle to deflect from magnetic north [7, 4]. Following this Ampère and Faraday were to lay the bases for classical electromagnetism. In 1821 Ampère discovered that current flowing in the same direction in parallel wires creates an attraction between the wires, and Faraday's discovery of induction in 1831 [8, 9, 4]. James Clerk Maxwell unified these theories to give a single set of equations in 1865 [10].

Faraday's contributions did not end with induction. What we know as the Faraday effect was discovered in 1845 [11]. The Faraday effect was witnessed by passing linearly polarised light through a piece of glass with a magnetic field present, the change in the optical polarisation was monitored showing that both the glass and light possessed magnetic properties. Pieter Zeeman followed on from Faraday's work and observed that by introducing a magnetic field the spectral lines of an atom broaden, discovering the magnetic Zeeman sublevels [12]. With this discovery of magnetic sublevels within the atom, the ability to measure magnetic fields based on the spectral splitting was enabled. For his discovery Zeeman was awarded the Nobel Prize in which he made reference to Faraday's work [13]. Twenty years later Wilhelm Hanle showed the change in fluorescent light polarisation from decaying electrons with changing magnetic field [14]. At the time it was thought that Hanle's discovery was in fact a Zeeman effect and was not fully accepted for a few years. Hanle's observation was not the first time this effect has been observed, with the first record of it being in 1912 by Robert Williams Wood [15]. Both the Faraday and Hanle effect are relevant in this thesis and discussed further in the next chapter.

Another process discussed and used heavily in this thesis is that of optical pumping. Optical pumping is the use of resonant light to create non-equilibrium states within a medium. This efficient method of controlling the internal states of atoms even allows population inversion to be achieved. With the discovery of optical pumping by Alfred Kastler in 1950 a new and exciting area of physics was uncovered [16]. One of the areas where the technique of optical pumping was harnessed was optically pumped magnetometers (OPMs). Bell and Bloom experimentally demonstrated the first OPM in 1957 [17, 18]. The Bell-Bloom magnetometer is a DC magnetometer measuring the magnitude of a magnetic field. The field is detected by modulating the pump beam in either intensity or frequency to match that of the Larmor frequency and detects an increase in signal amplitude when resonant [19]. The Larmor frequency, $\omega_L$, is the frequency at which an atom processes around a magnetic field and is related to the magnetic field by:

$$\omega_L = \gamma B, \tag{1.1}$$

where $\gamma$ is the atoms gyromagnetic ratio and $B$ is the magnitude of the measured field, shown in Fig 1.1a. The Larmor frequency matches the Zeeman shift in the low field regime where they both increase linearly with the magnetic field experienced. Fig 1.1b shows the Zeeman sublevels degeneracy being lifted when in a magnetic field with the sublevels moving from the solid lines by $\omega_L$. The on-resonance optical transition is also denoted by $\omega_0$.

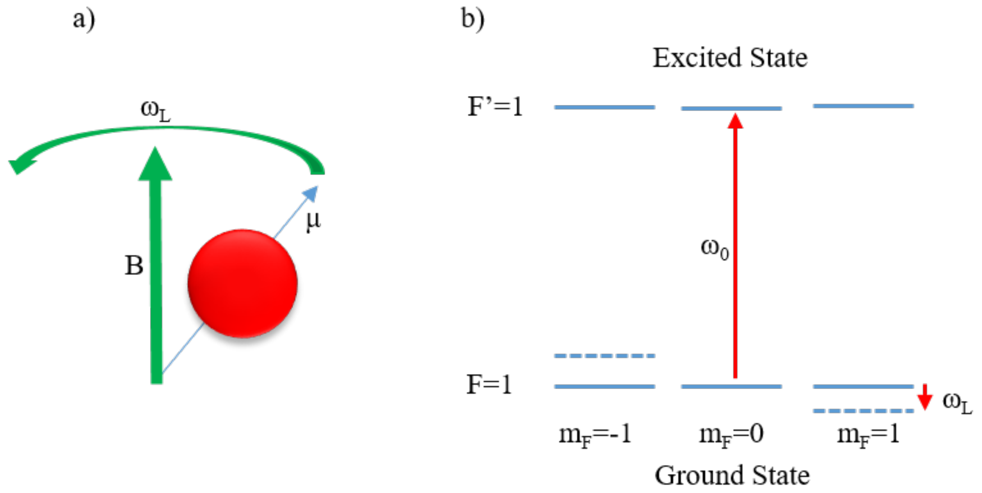

*Figure 1.1: a) An atom precessing in a magnetic field, B, at the Larmor Frequency, $\omega_L$ and $\mu$ showing the atoms magnetic moment. b) A representation of how a magnetic field shifts the magnetic states within the atom by the same amount, shown by the levels moving from the solid line to the dashed line. The on-resonance transition frequency is shown by $\omega_0$.*

In this thesis, spin exchange relaxation free (SERF) OPMs will be discussed. SERF systems work by eliminating a form of magnetic re-equilibrisation following optical pumping, known as spin exchange relaxation. To reach the SERF regime the sample of alkali atoms is heated to 100°C - 200°C depending on the alkali species that is being used in order to increase the density to achieve the required collisional regime. This increase in density increases the rate of spin exchange (SE) collisions far beyond the Larmor frequency, which is required to enter the SERF regime. This technique was first realised and used for magnetic resonance narrowing in the 1970's [20, 21].

The magnetic resonance describes the response of the atoms to a change in magnetic field. Its shape is broadened by relaxation mechanisms and quantified in two parts:

$$\Gamma_2 = \Gamma_1 + \Gamma_{SE} \ . \tag{1.2}$$

Here $\Gamma_2$ is the total magnetic linewidth or transverse relaxation rate, while $\Gamma_1$ is the longitudinal relaxation rate, or the spin destruction collision rate, and $\Gamma_{SE}$ is the rate of SE collisions. By suppressing SE the magnetic linewidth is narrowed becoming only dependant on the spin destructive collisions that limit $\Gamma_1$. Since the 1970's, when the SERF technique was first used in magnetometry, it has been used to provide some of the most sensitive measurements of magnetic fields that have been carried out to this day [22, 23]. The recent combination of decreasing size, increasing performance and flexibility in design has allowed OPMs to become an increasingly common method of biomagnetic field detection [24, 25].

Within the medical industry there are a number of different areas of magnetic field study such as the brain (magnetoencephalography or MEG), heart (magnetocardiography or MCG) as well as fetal cardiac signals (fetal magnetocardiography or fMCG), spine (magnetospinography or MSG), gastric (magnetogastrography or MGG) and muscle (magnetomyography or MMG). For example, MEG can be used for mapping magnetic field strength and frequencies produced by the brain, producing signals in the region of 10 fT - 1 pT [26]. Brain signals are also categorized into five frequency bands: delta ($\delta$) 0.2 Hz - 3 Hz, theta ($\theta$) 4 Hz - 7 Hz, alpha ($\alpha$) 8 Hz - 13 Hz, beta ($\beta$) 14 Hz - 31 Hz and gamma ($\gamma$)

32 Hz - 100 Hz [27, 28, 29, 30, 31]. These field strengths and frequencies outline operational requirements for a MEG sensor. MCG signals on the other hand tend to be in the range up to around 50 Hz and as large as 100 pT [32]. The first measurements of MEG signals were recorded in 1968 by David Cohen at the University of Illinois using an inductive pickup coil [33]. As with almost all measurements still today they were carried out in a magnetically shielded room (MSR) to attenuate large background fields, the largest of which typically is the Earth's geomagnetic field. Four years later Cohen carried out new measurements using an improved MSR and superconducting quantum interfering device (SQUID) [34]. The SQUID sensor had been invented a few years earlier by Ford Scientific Laboratories in Michigan [35]. One of the drawbacks of SQUIDs for some applications is that to create superconducting circuits cryogenic cooling is needed. For this a dewar to house the equipment and cryogenic liquid are required, which makes the system not only large but expensive to install and maintain [36, 37]. These drawbacks also mean that the SQUID sensors are static with a one size fits all approach to the sensors position. OPMs on the other hand can be worked into any size helmet allowing for much more freedom in design. This means experiments can accommodate movement of sensors, with appropriate active field control, and flexible placement with respect to the head and more suited to children and patients with epilepsy or schizophrenia [38].

The work carried out in this thesis is funded by the UK Quantum Technology Hub for Sensors and Timing. The goal of the UK Quantum Programme is to design and develop quantum technology within the UK. This project's ambition is to understand how to build a SERF sensor with noise performance that would allow it to be used for biomagnetic field detection. The information gathered and techniques used here will help inform a more portable version with the long term goal of being able to be used as an array of newly designed and built sensors.

From here Chapter 2 will go on to discuss the theory behind OPMs and more specifically a SERF magnetometer. Chapter 3 goes on to discuss the experimental setup of a single beam SERF OPM. In this first instance measurements are taken via an absorption signal using a single photodiode and the characterisation and optimisation are discussed in Chapter 4. The discussion then moves on to the design and operation of an optical rotation based sensor in Chapter 5. Chapter 6 discusses the comparison between the two operation modes of the sensor and limitations reached within the experimental set up. Chapter 7 will conclude the thesis and highlight key results and briefly discusses the improvements made to the experiment after this thesis was completed using the improvements suggested here to overcome limitations.

# Chapter 2

# Theory of Optically Pumped Magnetometers

This chapter is going to discuss the theory necessary for understanding the operation of an atomic magnetometer. The discussion will start with the atomic structure of alkali atoms. The alkali atom atomic structure is closely related to the optical lineshape produced by the allowed transitions. The importance of this is covered when discussing the absorption of light and how this affects the atom as well as how electrons move between magnetic sublevels. Optical pumping creates magnetisation in an ensemble of atoms and leads to discussion about the atomic magnetic resonance. Factors that have an effect on the magnetic resonance will also be discussed. The last points of discussion in this chapter will be around magnetic effects such as optical rotation and sensitivity measurements. The concepts discussed in this chapter are used extensively throughout this thesis.

## 2.1 Atomic Physics

### 2.1.1 Atomic Numbers

Atoms are made up from three building blocks: protons, neutrons and electrons. Protons have a positive charge, with a value of $1.602 \times 10^{-19}$ C, while neutrons are neutral. The electrons, on the other hand, have a negative charge of the same magnitude as the protons. The nucleus is a combination of protons and neutrons giving it an overall positive charge and the electrons form a negatively charged cloud around the nucleus.

What makes each element different from one another is the amount of protons in its nucleus. Different isotopes of an element can be formed by having varying numbers of neutrons. The general form of writing these numbers is: ${}^{A}_{Z}E$ where $E$ is the element, $Z$ is the number of protons and $A$ the number of protons and neutrons as given in Table 2.1 for potassium, rubidium and caesium.

| Element (E) | Mass Number (A) | Atomic Number (z) |
|---|---|---|
| K | 39 | 19 |
| Rb | 87 | 37 |
| Cs | 133 | 55 |

*Table 2.1: Atomic numbers for particular isotopes of potassium, rubidium and caesium.*

The electrons are arranged in shells and sub-shells surrounding the nucleus. Each sub-shell can hold a different amount of electrons as follows: $s - 2, p - 6, d - 10, f - 14$ and $g - 18$. Rubidium has electron shells which can be described as: $1s^2 2s^2 2p^6 3s^2 3p^6 4s^2 3d^{10} 4p^6 5s^1$ or shortened to $[\mathrm{Kr}]5s^1$ as the electron shells are the same as krypton, but with one extra electron in the outer shell. Other alkali atoms follow similar patterns. With one valance electron the alkali atoms behaviour is easier to model. This is because a photon can excite only a single electron, not multiple electrons in the same shell. Having a single outer electron makes the atoms hydrogenic [39, 40].

### 2.1.2 Quantum Numbers

Using the example of rubidium, we can now ignore the full sub-shells and focus on the one remaining electron. The coarsest of the quantum numbers is the principal quantum number, $n$. The principal quantum number describes the size of the atom in the simple Bohr model. The next character denotes the angular momentum of the shell. This is referred to as $\ell$: s = 0, p = 1, d = 2 and so on.

The orbital angular momentum, $L$, the next number to be considered, is a vector sum of the occupied $\ell$ states. In the case of alkali atoms, $L = 1$. As with $\ell$, $L$ is related to S, P and D, therefore $L = 1 \implies S$. The last quantum number needed now is $J$, the ground state angular momentum. $J$ is a vector sum of $L$ and $S$, where $S$ is the spin angular momentum. Combining the quantum numbers here the ground state term takes the form $n\ell\ {}^{2S+1}L_J$. For rubidium the ground state term is $5s\ {}^2S_{\frac{1}{2}}$ [41, 42].

### 2.1.3 Fine and Hyperfine Structure

The next level of complexity to consider is the fine structure. From the ground state the outer electron can be excited by resonant light through a number of transitions. This level of structure is caused due to spin-orbit coupling:

$$\Delta E_{S-O} = \frac{\beta}{2}(J(J+1) - L(L+1) - S(S+1)). \tag{2.1}$$

Here $\Delta E_{S-O}$ refers to the energy shift of a particular $J$ state where $\beta$ is the fine structure constant [43]. In the $5p$ manifold this results in no splitting in the ground state as $L = 0$. In the excited state there is a splitting between $5p\ {}^2P_{\frac{1}{2}}$ and $5p\ {}^2P_{\frac{3}{2}}$ as $L = 1$. There are two commonly used transitions in alkali atoms known as the D1 and D2 transitions. The D1 transition has an excited state with angular momentum the same as the ground state, and therefore hyperfine states the same as the ground state. However, the D2 transition excites to a level where the angular momentum is larger than the ground state, creating more hyperfine states. In this thesis we will focus mainly on the D1 transition, exciting from the ground state, $5s\ ^2S_{\frac{1}{2}}$, to the excited state, $5p\ ^2P_{\frac{1}{2}}$, for Rb.

The fine structure splits further into what is the hyperfine structure. The value of the hyperfine states, $F$, is calculated by $F = I \pm J$, where $I$ is the nuclear spin of the atom. Since for Rb $I = \frac{3}{2}$ and $J = \frac{1}{2}$ the hyperfine levels of $F = 2$ and $F = 1$ are found. The shift of a particular hyperfine level is, $\Delta E_{hfs}$, is given given by:

$$\Delta E_{hfs} = \frac{A_{hfs}}{2}(F(F+1) - J(J+1) - I(I+1)), \tag{2.2}$$

where $A_{hfs}$ is the hyperfine structure constant [43]. The levels discussed so far here are shown for rubidium-87 in Fig 2.1.

In order to resolve any further sublevels from here the application of a magnetic field is needed. Only when this is the case are the magnetic sublevels or Zeeman sublevels able to be resolved. The number of Zeeman sublevels is obtained by $2F + 1$ with the individual $m_F$ states being $m_F = -F, -F+1, ..., F-1, F$. This gives five magnetic levels for $F = 2$ hyperfine level in rubidium with $m_F = -2, -1, 0, 1, 2$. The $m_F$ state describes the projection of the hyperfine state on to the quantisation axis. Where $m_F$ is equal to the extreme values (-2 and 2) it is maximally aligned to the quantisation axis and when it is equal to 0 it is perpendicular to the quantisation axis. When these sublevels experience small magnetic fields their degeneracy is lifted and the shift of a particular energy level is:

$$\Delta E_z = g_F \mu_B m_F B_Z, \tag{2.3}$$

where $\Delta E$ is the energy shift in $J$, $\mu_B$ the Bohr magneton, $m_F$ the magnetic sublevel being affected and $B_Z$ is the strength of the field in T. The hyperfine $g$-factor, $g_F$, is

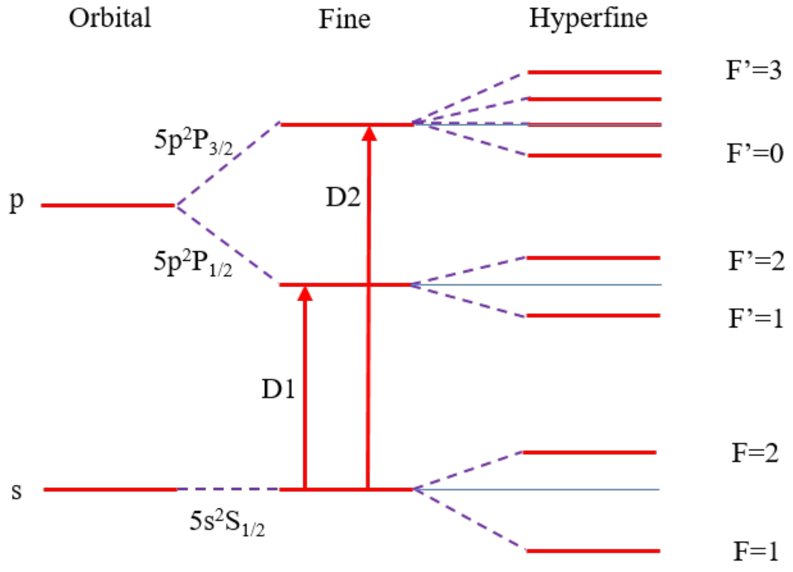

*Figure 2.1: Atomic structure schematic for rubidium-87 (not to scale). The splitting of the fine structure can be seen, allowing both D1 and D2 transitions. The hyperfine structure is also shown for both the excited states:* $J = \frac{1}{2}$ *and* $J = \frac{3}{2}$.

found using the expression:

$$g_F = g_J\left(\frac{F(F+1)+J(J+1)-I(I+1)}{2F(F+1)}\right) + g_I\left(\frac{F(F+1)-J(J+1)+I(I+1)}{2F(F+1)}\right), \tag{2.4}$$

where $g_J$ and $g_I$ are the angular momentum $g$-factor and nuclear spin $g$-factor respectively. The splitting between each individual magnetic sublevel relates to the Larmor frequency, $\omega_L = \frac{\Delta E_z}{\hbar}$. The hyperfine $g$-factor for each of the upper and lower hyperfine states of the ground manifold is approximately opposite, thus giving opposite splittings to the $m_F$ states of the same value in opposing hyperfine structures. Another effect of the opposite sign of $g_F$ is that atoms in similar $m_F$ sublevels precesses in opposite directions [43].

## 2.2 Optical Resonance

### 2.2.1 Collisional Broadening

When atoms absorb resonant photons, they are optically pumped. The probability of absorbing a photon is determined by the optical resonance lineshape. This section will go in to detail on how to model such lineshapes due to their importance in this thesis. A complete picture was not easily found during the time of research so a model was created pulling information from multiple sources. The starting point for the optical resonance is the natural linewidth which is measured in Hz:

$$\Gamma_N = \frac{1}{2\pi\tau_N}, \tag{2.5}$$

where $\tau_N$ is the natural lifetime of the excited state in seconds. The complete profile can be obtained by:

$$L(v - v_0) = \frac{1}{\pi}\frac{\frac{\Gamma_N}{2}}{(v - v_0)^2 + \left(\frac{\Gamma_N}{2}\right)^2}, \tag{2.6}$$

where $v$ and $v_0$ are the laser frequency and resonance frequency respectively [44]. A resonance of this shape is what is expected if an atom was to have no interaction with any other particles. The transitions themselves can be affected by many factors broadening, narrowing and even shifting them. Collisional broadening in the system is provided by collisions with quenching gas (discussed in Section 2.5) removing excited electrons from the excited state faster than they would spontaneously decay. This is a homogenoeous broadening mechanism of the form [45]:

$$\Gamma_C = \frac{1}{2\pi\tau_C}, \tag{2.7}$$

where $\tau_C$ is the time between collisions in seconds. Since collisional broadening is a homogeneous process it provides a Lorentzian distribution. The convolution of two

Lorentians is simply the sum, meaning that the resulting linewidth can be written as,

$$\Gamma_L = \Gamma_N + \Gamma_C. \tag{2.8}$$

Taking Eq 2.6 the absorption cross-section of the profile can calculated:

$$\sigma_L(v) = \pi r_e c f L(v - v_0), \tag{2.9}$$

where $r_e$ is the electron radius, $c$ the speed of light and $f$ the oscillator strength. Eq 2.9 can be simplified to an on-resonance form:

$$\sigma_L(v_0) = \frac{2 r_e c f}{\Gamma_L}. \tag{2.10}$$

### 2.2.2 Doppler Broadening

As atoms move around they will have varying components of velocity along the beam's propagation axis. This in turn leads to atoms seeing the laser frequency at different detunings from that of the frequency of the laser used in the lab. As this is different for many of the atoms due to their motion, this is an inhomogenous type of broadening and results in a Gaussian profile [45]. The linewidth of Doppler broadened resonances can be obtained through:

$$\Gamma_D = \sqrt{\frac{8 k_B T \ln 2}{m c^2}} v_0, \tag{2.11}$$

where $k_B$ is the Boltzman constant, $T$ the temperature in K and $m$ the mass of the atom. The full Doppler broadened resonance profile can be obtained from the Maxwell-Boltzmann distribution [46]:

$$G(v - v_0) = \frac{\sqrt{\frac{4 \ln 2}{\pi}}}{\Gamma_D} \exp\left(\frac{-4 \ln 2 (v - v_0)^2}{\Gamma_D^2}\right), \tag{2.12}$$

and similarly to the Lorentzian, the absorption cross-section at any detuning:

$$\sigma_D(v) = \pi r_e c f G(v - v_0), \tag{2.13}$$

and simplified when on-resonance:

$$\sigma_D(v_0) = \frac{2 r_e c f \sqrt{\pi \ln 2}}{\Gamma_D}. \tag{2.14}$$

### 2.2.3 Voigt Profile

As both the Gaussian and Lorentzian parts contribute to the overall optical resonance a Voigt profile is used to best describe the resonance shape. This is done by taking the convolution of the two profiles [47, 48]:

$$V(v - v_0) = L(v - v_0) * G(v - v_0). \tag{2.15}$$

This can be approximated by a pseudo Voigt, which returns the shape to an accuracy within 1%:

$$V(v - v_0) = \eta L(v - v_0) + (1 - \eta) G(v - v_0), \tag{2.16}$$

where $\eta$ is:

$$\eta = 1.36603\left(\frac{\Gamma_L}{\alpha}\right) - 0.47719\left(\frac{\Gamma_L}{\alpha}\right)^2 + 0.11116\left(\frac{\Gamma_L}{\alpha}\right)^3 \tag{2.17}$$

and where $\alpha$ is:

$$\begin{split}\alpha = (\Gamma_D^5 + 2.69269(\Gamma_D^4 \Gamma_L) + 2.42842(\Gamma_D^3 \Gamma_L^2) + \\ 4.47163(\Gamma_D^2 \Gamma_L^3) + 0.07842(\Gamma_D \Gamma_L^4) + \Gamma_L^5)^{\frac{1}{5}}.\end{split} \tag{2.18}$$

The absorption cross-section of the resonance can once again be obtained by:

$$\sigma_V(v) = \pi r_e c f \mathrm{Re}[V(v - v_0)]. \tag{2.19}$$

Working in the case where there is very little collisional broadening and the Doppler broadening is much larger, a Gaussian profile provides a good estimate of the absorption profile. The opposite can be said for when the collisional broadening is much larger than the Doppler broadening where a Lorentzian would also be a good approximation.

To calculate the total absorption cross-section at a particular frequency the sum of all the individual resonances is needed:

$$\sigma_T(v) = \pi r_e c f \Sigma_{F,F'} A_{F,F'} \mathrm{Re}[V(v - v_{F,F'})], \tag{2.20}$$

where $A_{F,F'}$ is the relative strength of the transition:

$$A_{F,F'} = \frac{(2F+1)(2F'+1)}{2I+1} \begin{Bmatrix} J & J' & 1 \\ F' & F & I \end{Bmatrix}^2, \tag{2.21}$$

with $F, F'$ showing the ground and excited hyperfine states of the transition being considered (D1 transition values given in Table 2.2 calculated using Eq 2.21). The curly brackets denote a Wigner-6j symbol. Using Eq 2.20 the total absorption cross-section of an atom can be modelled including all allowed transitions as shown in Fig 2.2 [49].

| Transition | $I = \frac{3}{2}$ | $I = \frac{5}{2}$ | $I = \frac{7}{2}$ |
|---|---|---|---|
| $F_L \rightarrow F'_U$ | $\frac{5}{16}$ | $\frac{35}{108}$ | $\frac{21}{64}$ |
| $F_L \rightarrow F'_L$ | $\frac{1}{16}$ | $\frac{5}{54}$ | $\frac{7}{64}$ |
| $F_U \rightarrow F'_U$ | $\frac{5}{16}$ | $\frac{7}{27}$ | $\frac{15}{64}$ |
| $F_U \rightarrow F'_L$ | $\frac{5}{16}$ | $\frac{35}{108}$ | $\frac{21}{64}$ |

*Table 2.2: Relative D1 transition strengths calculated using Eq 2.21. $F_L$ refers to the lower hyperfine ground state and $F_U$ the upper hyperfine ground state. $F'_L$ refers to the lower hyperfine excited state with $F'_U$ the upper hyperfine excited state. The relative transition strengths have been calculated for three different nuclear spins $I = \frac{3}{2}, \frac{5}{2}, \frac{7}{2}$*

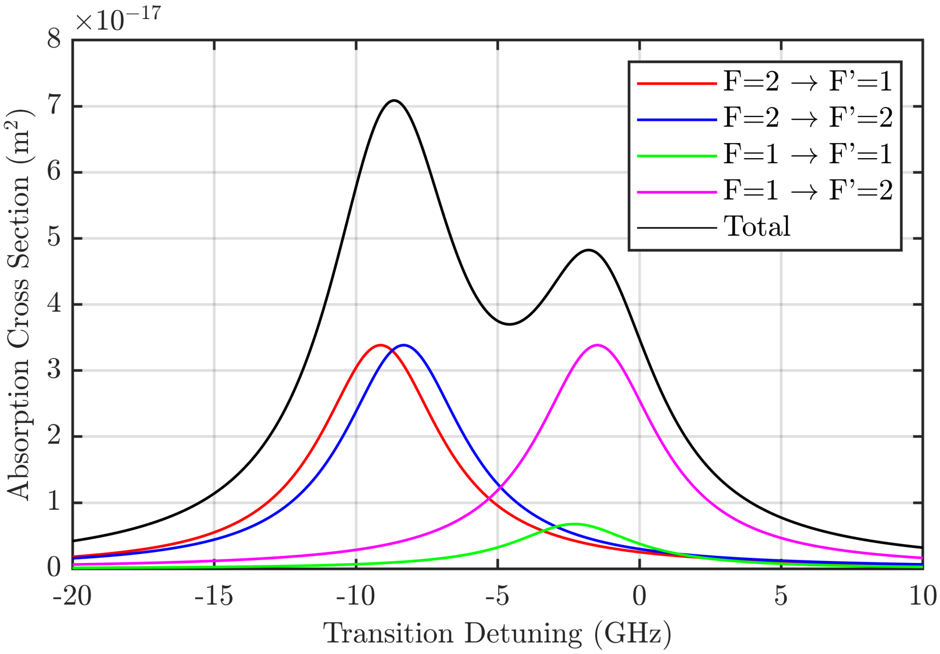

*Figure 2.2: Modelled absorption cross-sections of $^{87}$Rb D1 line with 200 Torr of nitrogen quenching gas. Each of the individual hyperfine transitions are shown as well as the total absorption cross-section experienced by light of varying detuning.*

### 2.2.4 Power Broadening

The last factor to calculate to complete the resonance profile is power broadening. This is achieved by calculating the saturation parameter, $\kappa$, which is found by scaling the intensity of the laser being used to the saturation intensity:

$$\kappa = \frac{I}{I_S}, \tag{2.22}$$

where $I_S$ is:

$$I_S = \frac{\pi h c \Gamma}{3\lambda^3}. \tag{2.23}$$

Here $h$ is Planck's constant, $\Gamma$ the full-width-half-max of the resonance, $\lambda$ the resonant wavelength, $I$ the beam intensity and $I_S$ the saturation intensity of the resonance. The saturation intensity is dependant on how long electrons spend in the excited state. This means the saturation intensity varies with the decay rate from the excited state by the addition of quenching gases and other factors which aid this removal.

The power broadening of the optical resonance scales with $\kappa$ and shown here as $\Gamma_{PB}$ [50, 51]:

$$\Gamma_{PB} = \Gamma\sqrt{\kappa + 1}, \tag{2.24}$$

where $\Gamma$ represents both $\Gamma_D$ and $\Gamma_L$ being the Doppler and Lorentzian linewidths as calculated by Eq 2.11 and Eq 2.8 respectively. The power broadened linewidths can then be used to model the optical resonances where the incident light is above the saturation parameter as shown in Fig 2.3.

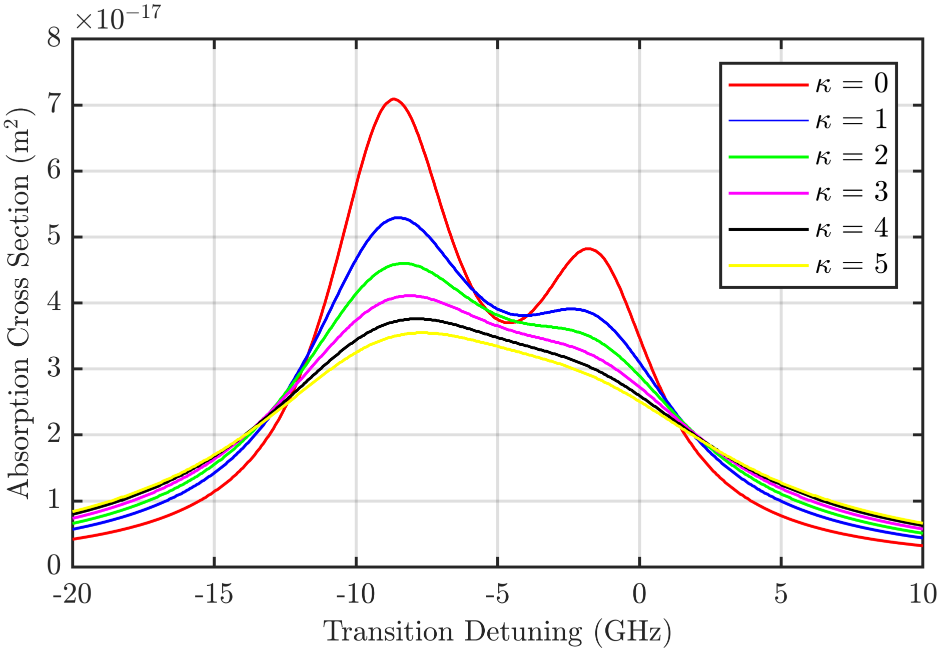

*Figure 2.3: Modelled power broadened absorption cross-sections for* $^{87}$*Rb D1 line with 200 Torr of nitrogen quenching gas. Here only the total absorption cross-section is shown but for varying laser intensities beyond saturation.*

## 2.3 Light Polarisation

To move the outer electron between the ground and excited state near resonant light is used. Light comes in three forms of polarisation: circular, linear and elliptical. The polarisation refers to how the electric field of the light oscillates. Linearly polarised light oscillates back and forth on a single axis while for circularly polarised light the field rotates in either left or right handed motion. Elliptical is a combination of both linear and circular. Assuming the quantisation axis, $B$ in this case, is parallel to the k-vector of the light, this would allow linear light to excite a $\pi$ transition and circular light to excite either a $\sigma^+$ or $\sigma^-$ transition.

The polarisation of the light will determine how the electron moves between the Zeeman sublevels, $m_F$. As the light is absorbed, so too is angular momentum of the light's polarisation. During this process there are selection rules which limit where the electron can move to: $\Delta\ell = \pm 1$, if $\Delta F = 0$ then $\Delta m_F = \pm 1$ and if $\Delta F = \pm 1$ then $\Delta m_F = 0, \pm 1$. The $m_F$ selection rules are determined by the light's polarisation where $\pi$ results in $\Delta m_F = 0$ and $\sigma^+$ and $\sigma^-$ returns $\Delta m_F = 1$ and $\Delta m_F = -1$ respectively with schematics of this shown in Fig 2.4. Fig 2.4a shows right circularly polarised light being used and shown by the red arrow and $\sigma^+$ while in Fig 2.4b linear light is used, again shown by the red arrow and $\pi$. The dashed yellow arrows show the possible routes the decaying electron can follow. The decaying electron follows the same set of rules that the excited electron is governed by with three variations of decay available being $\sigma^-$, $\pi$ and $\sigma^+$ again.

## 2.4 Rate Equations

The optical pumping rate can be obtained using the absorption cross-sections already calculated in Section 2.2. This is done by multiplying the cross-section by the photon flux, $\Phi$, giving an absorption rate of photons and allows the pumping rate at any

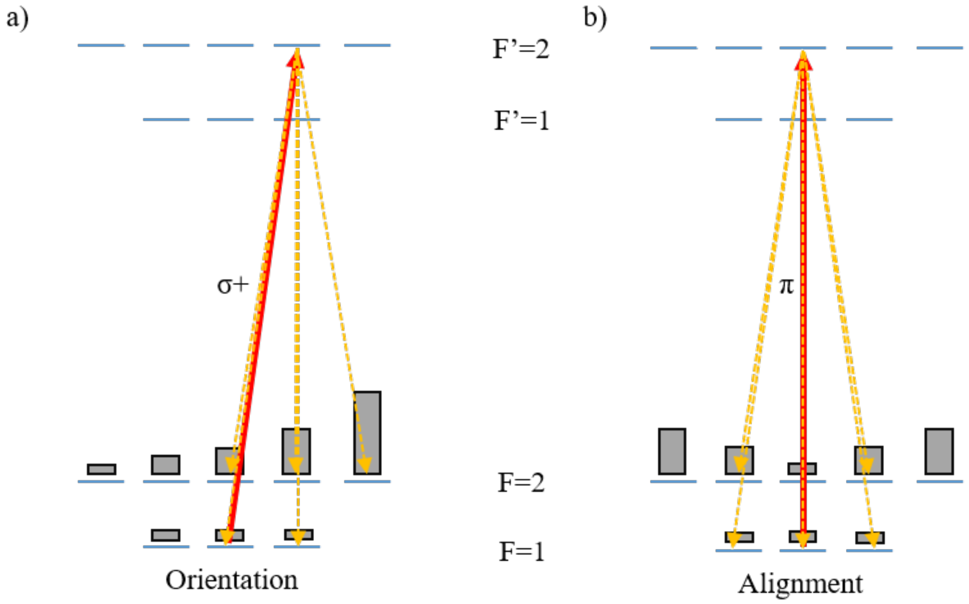

*Figure 2.4: Optical pumping schematic for both a) circular and b) linear polarisations where B is parallel to k. The use of circular light moves the population to a stretched Zeeman sublevel creating an orientation moment while linear light moves the population out to both extreme Zeeman sublevels creating an alignment moment.*

detuning to be obtained:

$$\Gamma_{OP} = \sigma_V \Phi. \tag{2.25}$$

To understand how the electron moves between different sublevels and calculate the population probability, transition strengths are needed:

$$T_S = (-1)^{F-m_F} \begin{pmatrix} F' & 1 & F \\ -m'_F & q & m_F \end{pmatrix}^2 \langle F||er||F'\rangle, \tag{2.26}$$

where the circular brackets show a Wigner-3j symbol, the ket is the initial state that the operator acts upon, and the bra is the final state.

Upon the electrons decay back to the ground state there will be a similar effect where multiple transitions are allowed but are weighted differently. All the branching ratios ($B_R$) from a particular excited magnetic sublevel must equal one [52]:

$$B_R = (2J'+1)(2F+1)(2F'+1) \sum_{q=-1,0,1} \begin{pmatrix} F' & 1 & F \\ -m'_F & q & m_F \end{pmatrix}^2 \begin{Bmatrix} F & 1 & F' \\ J' & I & J \end{Bmatrix}^2 . \tag{2.27}$$

By combining these values the rate of change, $\dot{\rho}$, of any sublevel can be calculated [53]:

$$\dot{\rho}_{F,m_F} = -\Gamma_{OP}\, T_S + \sum_{F}^{-F} \sum_{m_F=F}^{m_F=-F} \Gamma_{OP}\, T_S\, B_R. \tag{2.28}$$

Using Eq 2.28 the probability of population in each Zeeman sublevel can be calculated

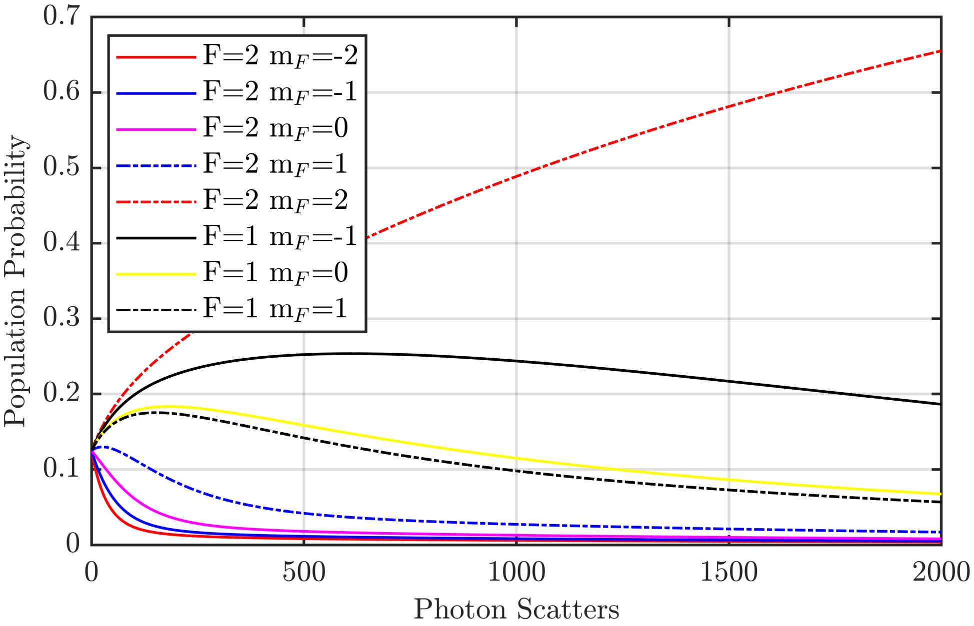

*Figure 2.5: Modelled population movement based on photon scatter for the F=2→F'=1 transition of $^{87}$Rb D1 line with 200 Torr of nitrogen quenching gas. Circularly polarised light has been assumed here with the population build up happening in the stretched state.*

after each photon scatter. By running multiple photon scatters the probability of the electron occupying a particular magnetic sublevel can be modelled. Showing how the probability changes in each Zeeman sublevel for a collisionally broadened $F = 2 \rightarrow F' = 1$ transition is shown in Fig 2.5. The three remaining transitions

$F = 2 \rightarrow F' = 2$, $F = 1 \rightarrow F' = 1$ and $F = 1 \rightarrow F' = 2$ are shown in Appendix A. Circularly polarised light has been used in this model and the population can be seen to continually build up in the $F = 2$, $m_F = 2$ sublevel. It is interesting to see how the lower ground state populations evolve where they initially gain population before slowly loosing it. This is due to the fact that they are not fully on-resonance, but there is still a small probability of absorption due to the broadening of the optical resonances. Atoms initially fall in to this faster than they are being removed until the point where a large degree of polarisation is built up in the stretched state and fewer atoms are decaying into the lower ground state.

## 2.5 Buffer and Quenching Gas

As has been discussed already in Section 2.2.1, the linewidth, and therefore the absorption cross-section, can be affected by collisional broadening. A process that can induce this effect is using buffer and quenching gases. When using gasses in cells the atoms are moving around at high speeds due to their temperature meaning they can undergo collisions with the cell walls frequently. The purpose of a buffer gas is to reduce the rate of wall collisions the alkali atoms experience by causing elastic collisions between the alkali atoms and the buffer gas. Wall collisions have a large chance of depolarising the electron (discussed in Section 2.7.3), so reducing these types of collisions in certain circumstances is beneficial. A second reason for using buffer gases is that alkali-alkali collisions which occur when the electron is in the ground state. These ground state collisions are spin destructive collisions and discussed further in Section 2.7.2 and values for the collisional cross-section given in Table 2.6 [54]. The chance of a spin destructive alkali-buffer gas collision happening is small due to their collisional cross-section and is given in Table 2.3. This provides a small chance of depolarisation removing the electron from the stretched state. There are other ways of reducing the wall collisions, namely by using an anti-relaxation coating on the cell walls. This is most commonly done by applying a layer of paraffin [55]. Buffer gas comes in many different forms from helium to nitrogen, neon and argon to name just a few [56]. Combinations of these gases might be used to balance the shifts experienced by certain gases (shifts for nitrogen shown in Table 2.4) as well as some gases also being used as a quencher as well as a buffer [49].

The buffer gases that can act as a quencher are in molecular form. This is because molecules can absorb energy from the excited alkali atoms into their vibrational modes, allowing the atom to decay without releasing a resonant photon. The benefit of not releasing a resonant photon when decaying is that the photon will have a randomised polarisation and direction. The photon can not then go on to be reabsorbed by a neighbouring atom, destroying its spin polarisation. This process is known as radiation trapping [57]. The excited state collisions between the alkali and quencher can also cause excited state mixing of the alkali atom. As there are no selection rules for the excited state mixing, a resonantly excited atom has equal probability of the electron occupying any of the excited states if there is sufficient quenching gas pressure. This has an effect on the optical pumping as it becomes extremely hard to create and maintain polarisation in the ground state. The excited state redistribution tries to repopulate the opposite hyperfine ground state that is having the population removed by optical pumping. As has been previously mentioned in Section 2.5, collisions between atoms broaden the Lorentzian profile with the broadening factor for nitrogen given in Table 2.4. The quenching process has the largest effect on the optical lineshape as its collisional cross-section is orders of magnitudes larger than that of a spin destructive collision and also provided in Table 2.3. The broadening of the optical resonance can be calculated by:

$$\Gamma_Q = \sigma_Q n_q \bar{v}, \tag{2.29}$$

where $\sigma_Q$ is the quenching cross-section and $n_q$ is quenching gas density.

By using the values shown in Table 2.3 in conjunction with the Eq 2.20, a model

| Collision | Q Cross-section ($m^2$) | SD Cross-section ($m^2$) |
|---|---|---|
| K-$N_2$ | $3.5\times10^{-19}$ | $7.9\times10^{-27}$ |
| Rb-$N_2$ | $5.8\times10^{-19}$ | $1\times10^{-26}$ |
| Cs-$N_2$ | $5.5\times10^{-19}$ | $5.5\times10^{-26}$ |

*Table 2.3: Buffer gas quenching and spin-destructive cross-sections for nitrogen and potassium, rubidium and caesium [58]*

| Collision | $\Delta\Gamma$ (MHz/Torr) | $\Delta\delta$ (MHz/Torr) |
|---|---|---|
| K-$N_2$ | 34.9 | -6.8 |
| Rb-$N_2$ | 32.6 | -7.4 |
| Cs-$N_2$ | 32.7 | -7.7 |

*Table 2.4: Broadening and shift values for nitrogen gas and potassium, rubidium and caesium [59, 60, 61, 62, 63, 64]*

describing the broadening and shift experienced for different quenching gas pressures can be created and is shown in Fig 2.6. It can be seen that with only 100 Torr of nitrogen quenching gas there are two clear peaks. The left peak being the $F = 2 \rightarrow F' = 1/2$ transition and having the largest absorption cross-section and the right peak being $F = 1 \rightarrow F' = 1/2$ transition. As the amount of quenching gas is increased the hyperfine transitions broaden, reduce in amplitude and shift further from the 0 GHz point. Once at 1000 Torr there is just a single peak with a half-width-half-max (HWHM) of nearly 15 GHz.

## 2.6 Light Shift

As the optical resonances broaden from increased amounts of quenching gas more than just the optical pumping can be impacted, with phenomenon such as light shift also being affected. Light shift is a ″fictitious″ magnetic field seen by the atoms that is caused by an electric dipole interaction between the light's electric field which is perpendicular to the k-vector. The field which is caused by the light's oscillating electric field adds on to any already present static fields.

There are two parts to light shift which add together to provide the full

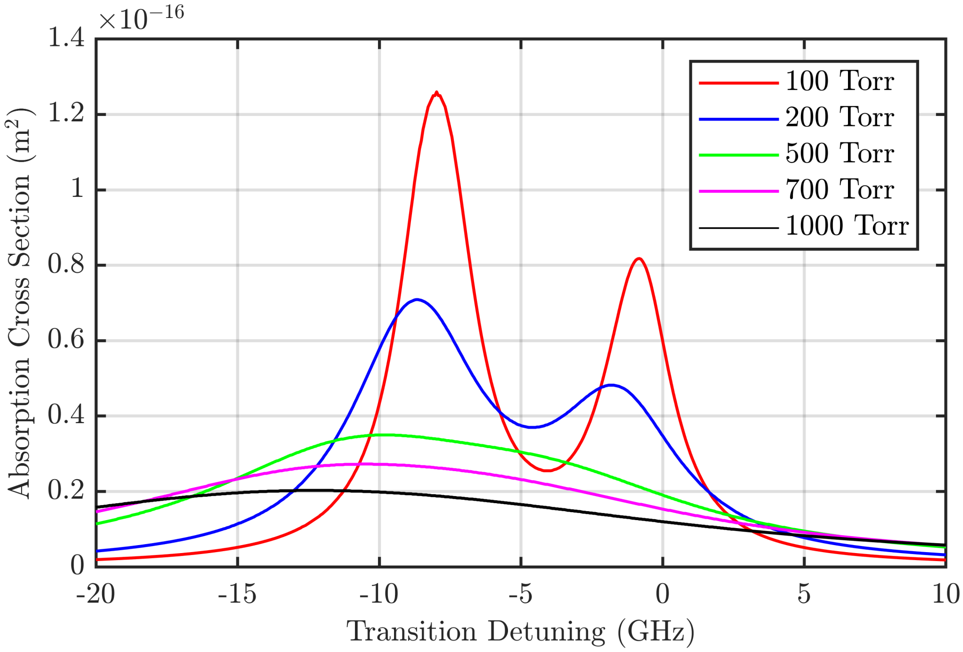

*Figure 2.6: Modelled quenching gas broadened absorption cross-sections for $^{87}$Rb D1 line. Different amounts of nitrogen quenching gas have been used to show how the optical resonances total absorption cross-section varies with increasing pressures.*

fictitious field perceived by the atoms. These are the effects caused by real transitions and the effects caused by the virtual transition. The real transitions are the transitions in which light can excite atoms. While in the excited state atoms experience some decoherence from those in the ground state. This is caused by the fact that the gyromagnetic ratios of the ground and excited states differ. The difference in gyro magnetic ratios means that an electron in an excited state will precess at a different frequency to those in the ground state and no longer be in phase with each other [65].

The virtual part is not caused by a transition, but rather anomalous dispersion of the light [66]. This dispersion is due to the imaginary part of the profile. Physically this represents the change of refractive index of the medium with changing detuning, $\Delta$. The real and imaginary parts are connected through the Kramer-Kronig relations. The imaginary part of a real data set can also be obtained by taking a Hilbert transform which applies a 90° phase shift, shown in Fig 2.7 [67]. This in turn creates a plot called a dispersive where the real part decays as a function of $1/\Delta^2$ and the imaginary part as

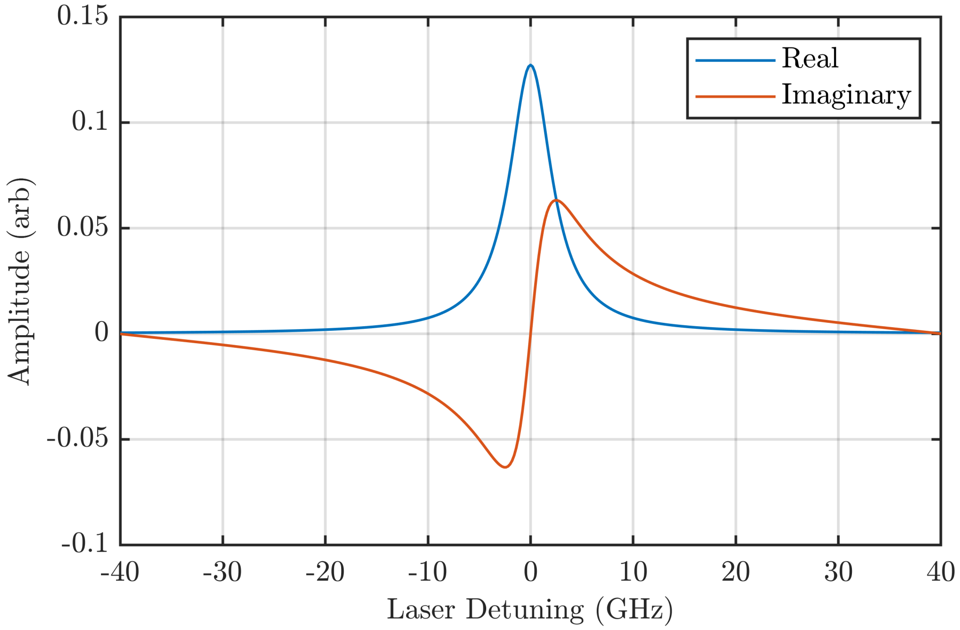

*Figure 2.7: Real and imaginary parts of a Lorentzian profile. The real part is a standard Lorentzian while the Imaginary part has been Hilbert transformed which shifts the phase by 90°.*

$1/\Delta$. When the light is off-resonance some photons are not absorbed but interact with the atoms causing a shift in the Zeeman sublevels [68].

The real contribution to the overall shift is usually negligible in comparison to the virtual, so the total shift can be well approximated by [65, 66]:

$$B_{LS-I} = \frac{-\pi r_e c f \Phi}{\gamma} \mathrm{Im}[V(v - v_0)]s. \tag{2.30}$$

Here $\Phi$ is the photon flux and Im refers to the imaginary part of the Voigt profile. Light polarisation is represented by $s$, where circularly polarised light has a value of $\pm 1$ and linearly polarised light $s = 0$. When modelling the light shift, it can be seen how much it varies with detuning in Fig 2.8. Here it can be seen how the shifts of the four individual transitions add and subtract from each other with the largest effects being seen when the light is detuned away from the resonance peak and closer to the steepest part of the resonance wings. Comparing Fig 2.8 with Fig 2.2, the steepest point of the absorption cross-section is around -11 GHz, which is where the largest light shift is experienced.

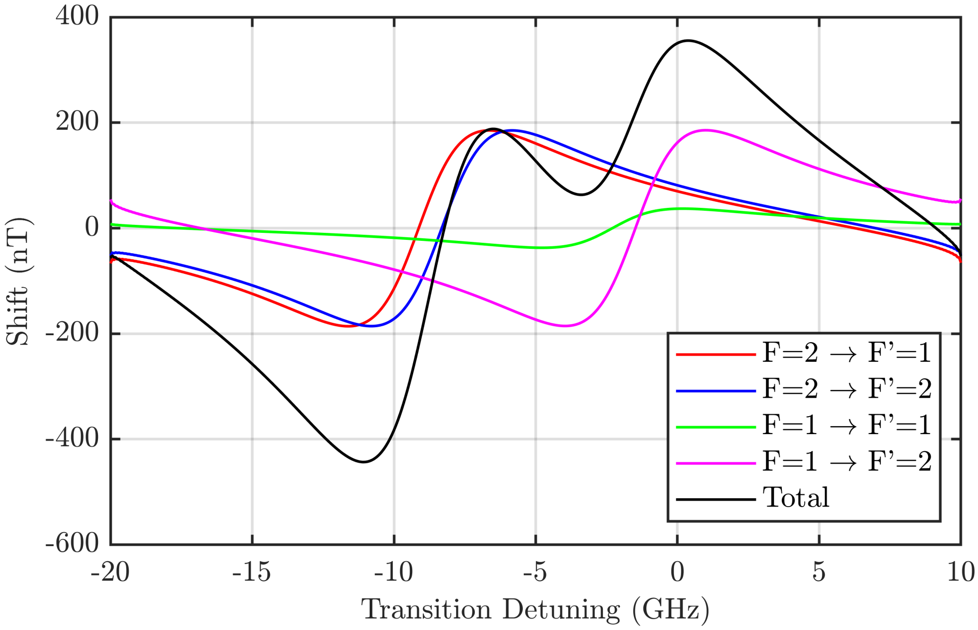

*Figure 2.8: Modelled magnetic field that light shift produces when using a 6 mW beam on a cell with* $^{87}$*Rb and 200 Torr of nitrogen quenching gas. The shift of each of the four D1 allowed transitions are shown as well as the total shift.*

## 2.7 Magnetic Resonance

### 2.7.1 Relaxation Mechanisms

As discussed in Section 1, atoms precess around magnetic fields. The Larmor frequency is described in Eq 1.1, where $\gamma$ is the gyromagnetic ratio:

$$\gamma = \frac{g_F \mu_B}{\hbar}, \tag{2.31}$$

and $\mu_B$ the Bohr magneton:

$$\mu_B = \frac{e\hbar}{2m_e}. \tag{2.32}$$

This phenomenon is caused by torque trying to align the magnetic dipole moment of the atom with the magnetic field:

$$\tau = \mu B \sin\theta. \tag{2.33}$$

The transverse relaxation rate of the magnetic resonance, $\Gamma_2$, is made up of two parts:

$$\Gamma_2 = \frac{1}{T_2} = \Gamma_1 + \Gamma_{SE}, \tag{2.34}$$

Here $T_2$ is the time between collisions and $\Gamma_{SE}$ is the rate of spin exchange collisions between alkali atoms and will be discussed more in Section 2.7.4. The longitudinal relaxation rate, $\Gamma_1$, encompasses all spin destructive collisions ($\Gamma_{SD}$) as well as cell wall collisions ($\Gamma_{WC}$):

$$\Gamma_1 = \Gamma_{SD} + \Gamma_{WC}. \tag{2.35}$$

The total magnetic relaxation rate of a nitrogen buffer gas cell with rubidium for changing temperature and buffer pressure is shown in Fig 2.9a. In the lower temperatures (50°C - 100°C) a dip is present in the data. A extract of this is shown in Fig 2.9b, showing how the individual relaxation mechanisms change with buffer gas pressure for a single temperature and will be discussed further in the next sections. In the higher temperatures (> 100°C) the landscape is linear with increasing buffer gas pressure increase. This is because at these temperatures the SE relaxation mechanism has become dominant.

Spin destructive collisions include destructive collisions with other alkali atoms and buffer gas. As the temperature rises so does the velocity, $\bar{v}$, of the atoms:

$$\bar{v} = \sqrt{\frac{8k_BT}{\pi M}}, \tag{2.36}$$

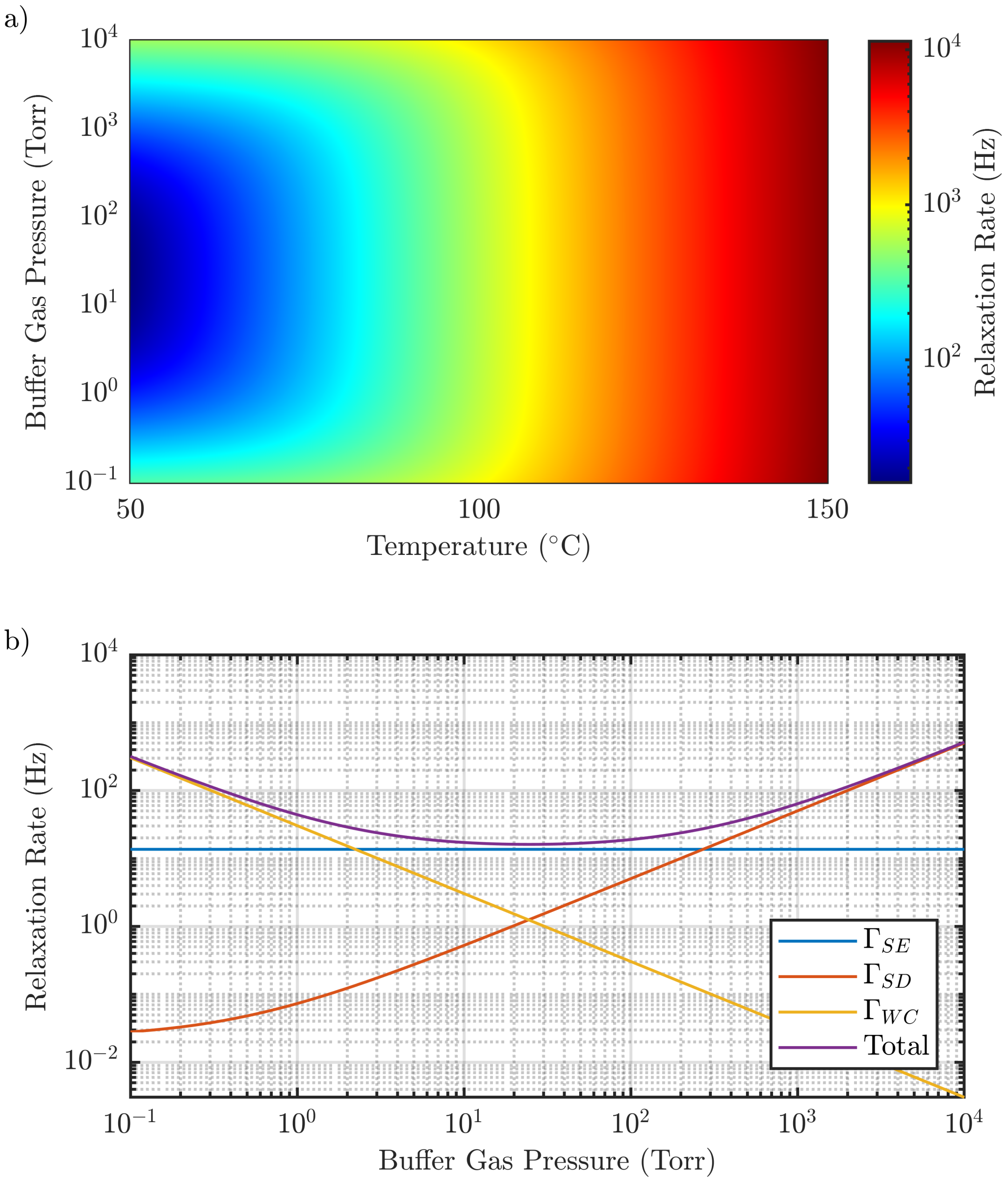

*Figure 2.9: a) A model of the total relaxation rate of a 10 mm$^3$ cell of $^{87}Rb$ with changing temperature and nitrogen buffer gas pressure. b) The individual relaxation mechanisms shown by taking a slice of (a) at 50° C. This model does not include the effects of being spin exchange relaxation free.*

where $k_B$ is the Boltzmann constant, T the temperature in K and M the reduced mass of the colliding particles:

$$M = \frac{1}{\frac{1}{m_1} + \frac{1}{m_2}}. \tag{2.37}$$

Here $m_1$ and $m_2$ are the individual masses of the colliding particles. As the alkali gas is usually in a solid or liquid state at room temperature, the following expression is used to obtain the atomic density, $n_A$, of a saturated vapour at a desired temperature:

$$n_A = \frac{1}{T} 10^{21.866 + C_1 - \frac{C_2}{T}}, \tag{2.38}$$

where $C_1$ and $C_2$ are constants given in Table 2.5. Depending if the alkali is solid or liquid before evaporating, the correct constants need to be used to obtain an accurate density. By doing so the atomic density in calculated in atoms/cm$^3$. The increased velocity and density of atoms increases the number of collisions occurring each second which means that the amount of destructive collisions must also increase with the temperature.

| Element | $C_1$ Solid | $C_1$ Liquid | $C_2$ Solid | $C_2$ Liquid |
|---|---|---|---|---|
| K | 4.961 | 4.402 | 4646 | 4453 |
| Rb | 4.857 | 4.312 | 4215 | 4040 |
| Cs | 4.711 | 4.165 | 3999 | 3830 |

*Table 2.5: Alkali density constants for potassium, rubidium and caesium [69, 70, 71].*

Using the density of alkali vapour and the length of vapour the light has to pass through, it can be calculated how far the light will travel and/or how much light will exit the vapour:

$$I(z) = I(0) \exp(-OD), \tag{2.39}$$

where $I(z)$ is the intensity of the light after depth $z$ travelled in the vapour, $I(0)$ is the intensity before entering the cell and $OD$ the optical depth:

$$OD = n_A \sigma(v) l, \tag{2.40}$$

with $l$ being the length of the cell.

### 2.7.2 Spin Destruction Collision

Spin destructive collisions are a form of relaxation and caused by depolarising collisions with other elements and molecules:

$$\Gamma_{SD} = \frac{1}{q_I}(\sigma_{SD} n_A \bar{v} + \sigma_{SD} n_B \bar{v}). \tag{2.41}$$

Here $q_I$ is the nuclear slowing down factor with the subscript of $\frac{3}{2}$, $\frac{5}{2}$ and $\frac{7}{2}$ representing the nuclear spin, $I$, of the atom. The nuclear slowing down factor is highly dependent on the amount of spin polarisation that has been created [72]. As electrons experience these depolarising collisions they change magnetic sublevel within the hyperfine state. This change in Zeeman sublevel changes the angular momentum along the quantisation axis. The cross-sections of spin exchange and spin destruction collisions between alkali atoms are given below in Table 2.6.

| Collision | SE Cross-section (cm$^2$) | SD Cross-section (cm$^2$) |
|---|---|---|
| K-K | $1.8\times10^{-14}$ | $1\times10^{-18}$ |
| Rb-Rb | $1.9\times10^{-14}$ | $1.6\times10^{-17}$ |
| Cs-Cs | $2.1\times10^{-14}$ | $2\times10^{-16}$ |

*Table 2.6: Alkali-alkali collisional cross-sections for SE and SD collisions. SE cross-sections are orders of magnitude larger the SD and can be a dominant form of relaxation [58].*

It can be seen in Fig 2.9b how the rate of spin destruction relaxation increases with the increased buffer gas pressure for a given temperature. This is expected as the spin destructive collisional cross-sections for alkali-alkali collisions and alkali-buffer gas collisions are combined, as described in Eq 2.41. This continually increasing relaxation rate with pressure leads of the spin destructive relaxation becoming a dominant form of relaxation at higher buffer gas pressures in low temperatures.

### 2.7.3 Wall Collision

Wall collisions, as the name implies, are collisions between alkali atoms and cell walls. These collisions are completely depolarising as the atom gets briefly absorbed into the cell wall. While it is there it experiences magnetic and electric fields created by ions in the glass, randomising the electron spin before being released back into the cell [73]. The rate of collisions, $\Gamma_{WC}$, is dependent on many factors:

$$\Gamma_{WC} = P_{depol}\frac{D}{d^2}, \tag{2.42}$$

where d is the cell smallest dimension and $P_{depol}$ is the chance of depolarisation, usually governed by anti-relaxation coatings if included. $D$ is the diffusion constant:

$$D = \frac{1}{3}\lambda\bar{v}, \tag{2.43}$$

where $\lambda$ is the mean free path and $\bar{v}$ is the average velocity of alkali atoms:

$$\lambda = \frac{1}{\sqrt{2}n_B\sigma_B}. \tag{2.44}$$

Here the $\sqrt{2}$ comes from the mean relative velocity of the two bodies, $n_B$ the density of the gas being moved through and $\sigma_B$ the ballistic cross-section:

$$\sigma_B = \pi(r_A + r_B)^2, \tag{2.45}$$

with $r_A$ and $r_B$ the radii of the particles in question. For low buffer gas pressures wall collisions will be a large contributor towards relaxation as there is nothing to increase the time between the wall collisions. This will reduce as the amount of buffer gas present

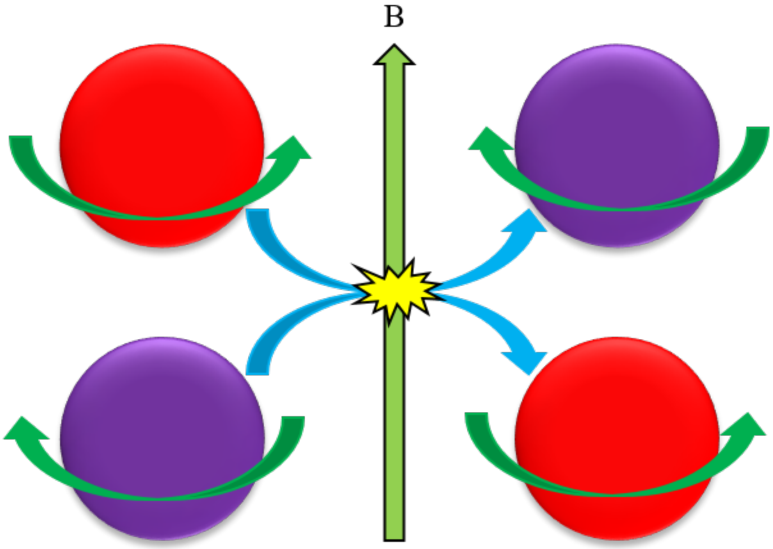

*Figure 2.10: Spin exchange collision with the upper and lower hyperfine ground state represented by blue and red.*

in the cell increases until a buffer gas pressure where the alkali-buffer gas collisions will take over, as seen in Fig 2.9b. This point is dependant on the species of alkali vapour, the density of the vapour, buffer gas used and cell dimensions.

### 2.7.4 Spin Exchange Collision

Spin exchange collisions happen when two alkali atoms that are in different hyperfine ground states collide. Atoms in the upper and lower hyperfine states precess in the opposite directions, caused by their hyperfine $g$-factor being opposite as shown schematically in Fig 2.10. The collision is elastic and angular momentum must be conserved meaning the direction of precession could be flipped [74, 75]. The rate at which spin exchange relaxation takes place can be calculated:

$$\Gamma_{SE} = \frac{1}{q_{SE}}(\sigma_{SE} n_A \bar{v}), \tag{2.46}$$

$\sigma_{SE}$ represents the spin-exchange collisional cross-section, given in Table 2.6. The remaining variable, $q_{SE}$, is the spin-exchange broadening factor:

$$\frac{1}{q_{SE}} = \frac{2I(2I-1)}{3(2I+1)^2}, \tag{2.47}$$

which depends on the ambient magnetic field. As the magnetic field approaches zero, $q_{SE}$ also tends to zero. The cross-section of a spin exchange collision is orders of magnitude larger than any of other collisions, meaning that as the vapour density is increased it quickly becomes a dominant form of relaxation. However, a phenomenon of entering a regime where the sample becomes spin exchange relaxation free takes place when the spin exchange rate is significantly larger than the Larmor frequency and is discussed in the next section.

## 2.8 Spin Exchange Relaxation Free

The impact of increasing the temperature of an alkali gas to the point where the effects of spin exchange are reduced were known before the first SERF magnetometer [76, 77]. The reason behind the phenomena is that the two hyperfine ground states in an atom have opposite $g_F$ values. This means that Zeeman sublevels in one hyperfine state precess in one direction, while in the other they precess in the opposite direction. When atoms in different hyperfine states collide they have an elastic collision where angular momentum is conserved, this means they can not leave the interaction both in the same hyperfine level. Instead they switch hyperfine levels as well as destroying polarisation.

In order to eliminate the contribution of spin exchange relaxation, the rate of SE collisions needs to be increased. The SE rate needs to be on the order of roughly 100 times faster than the Larmor frequency the atoms are experiencing [77]. Shown in Fig 2.11 are Cs, Rb and K experiencing a 1 nT static field. Their Larmor frequency is shown by the dashed line and the SE rate they need to reach respectively to suppress SE relaxation by the dash-dot line. This increased SE rate means that atoms are colliding with each other and changing hyperfine ground state after only a fraction of their Larmor precession.

The SERF regime is more easily reached in lower ambient magnetic fields. In these low field conditions, atoms are precessing sufficiently slow that in order for the SE collisions to reach the condition of being 100 time faster than the Larmor frequency, the temperatures can be lower. As can be seen from the trend in Fig 2.11, high field values would require an increased temperature to meet the condition mentioned already, reaching temperatures which would not be practical for biomedical applications. As the ambient magnetic field tends towards zero, so does the Larmor frequency, completely suppressing SE relaxation. The reason for this suppression is due to the dephasing that is caused by the precession around the magnetic field when atoms are pumped into the excited states.

As there are more Zeeman sublevels in the upper hyperfine ground state ($-F \leq m_F \leq F$), when undergoing rapid SE collisions in the SERF regime, the electrons statistically have a higher probability of being in an upper hyperfine ground state. This will cause the ensemble as a whole to precess in the direction of the upper ground state but at a reduced frequency caused by the rapid collisions:

$$\omega_q = \frac{\omega_L}{q}, \tag{2.48}$$

where $q$ is the nuclear slowing down factor as discussed in Section 2.7.2.

## 2.9 Hanle Effect

### 2.9.1 Polarisation

A phenomenon used to measure the magnetic resonance is the Hanle effect. The Hanle effect, when first discovered, showed how the fluorescent polarisation from an excited

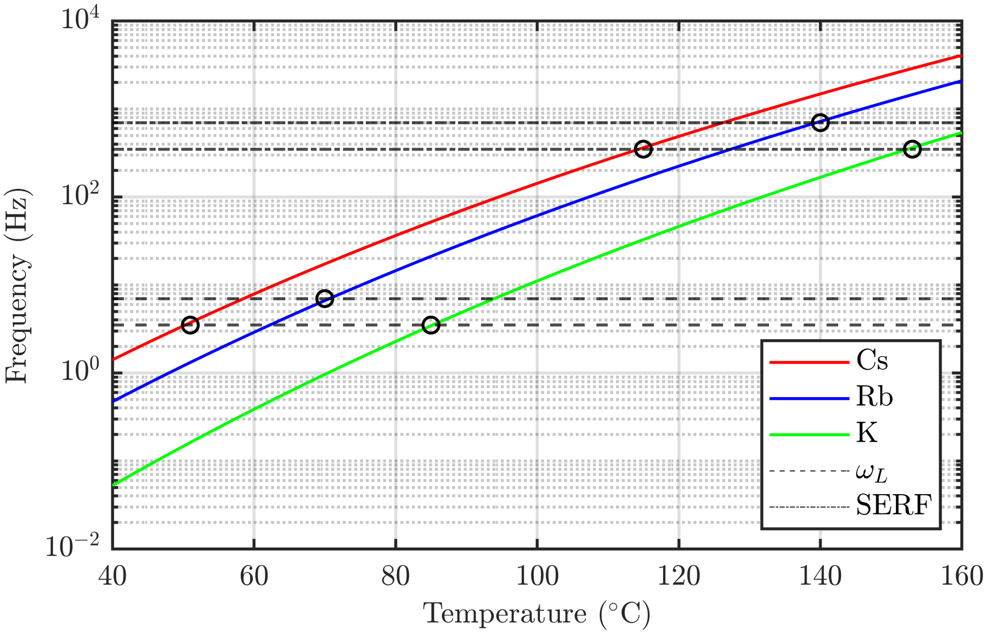

*Figure 2.11: Spin-exchange collision rate as a function of temperature. The Larmor frequency in a 1 nT field shown by the dashed line and 100 times that shown the dash-dot line.*

atom depends on the direction a magnetic field is applied [14]. A classical explanation for this is that if an atom is excited by resonant light in the $z$ direction with a weak magnetic field along $x$, the atom will precess around the magnetic field. From the $x$ direction emitted light would appear to be circularly polarised. However, when viewed from the $y$ direction the light would appear to oscillate rather than rotate. This leads to the fluorescent light having a linear polarisation [78]. This fluorescent polarisation effect is usually only seen for weak magnetic fields, when the Zeeman splitting is within the linewidth of the resonance. This is what is referred to as the Hanle effect, level crossing and zero-field crossing. Level crossing can also be achieved with larger fields when levels from different hyperfine states cross within the linewidth.

### 2.9.2 Magnetically Induced Absorption and Transparency

Magnetically induced absorption (MIA) and magnetically induced transparency (MIT) are used as a detection method in this thesis and referred to as the Hanle effect, due to the zero-field resonance they produce. These resonances can be described in OPMs by using the Bloch equations:

$$\frac{d}{dt}\begin{pmatrix} M_x \\ M_y \\ M_z \end{pmatrix} = \begin{pmatrix} -\Gamma & \gamma B_z & -\gamma B_y \\ -\gamma B_z & -\Gamma & \gamma B_x \\ \gamma B_y & -\gamma B_x & -\Gamma \end{pmatrix} \begin{pmatrix} M_x \\ M_y \\ M_z \end{pmatrix} + \begin{pmatrix} 0 \\ 0 \\ \Gamma_P M_0 \end{pmatrix}. \tag{2.49}$$

The Bloch equations are used to derive the magnetisation, $M$, in any direction as a function of the relaxation, $\Gamma$, and magnetic fields, $B$, in the system. Assuming the beam to be along the z-axis, this is then referred to as the longitudinal axis. Using this definition of longitudinal axis along the z-axis, the x-axis and y-axis then become the transverse axes. Solving the Bloch Equations first of all for the transverse field. In the case of the y-axis, setting the change in magnetisation to steady state and $B_x$ and $B_z$ to zero. As the pumping and detection direction are both along the z-axis this is the magnetisation which is of interest:

$$M_z = \frac{\Gamma}{\Gamma^2 + (\gamma B_y)^2}. \tag{2.50}$$

When modelling Eq 2.50 with a sweeping $B_y$ field the expected response in $M_z$ is seen in Fig 2.12 with a peak in magnetisation at a field of 0 nT. This is because all the atoms will be aligned along the beam axis at this point giving maximum transmission of light. As the depolarising transverse field is applied the atoms move away from being aligned along the beam axis in a the stretched state, becoming more absorbent. This absorption is due to coherences being created between neighbouring sublevels split by the Larmor frequency [79].

In the case of solving Eq 2.49 for a sweeping field along the longitudinal axis ($B_z$) a static field also needs to be included on one of the transverse axes:

$$M_z = 1 - \frac{(\gamma B_x)^2}{(\gamma B_x)^2 + (\gamma B_z)^2 + \Gamma^2}. \tag{2.51}$$

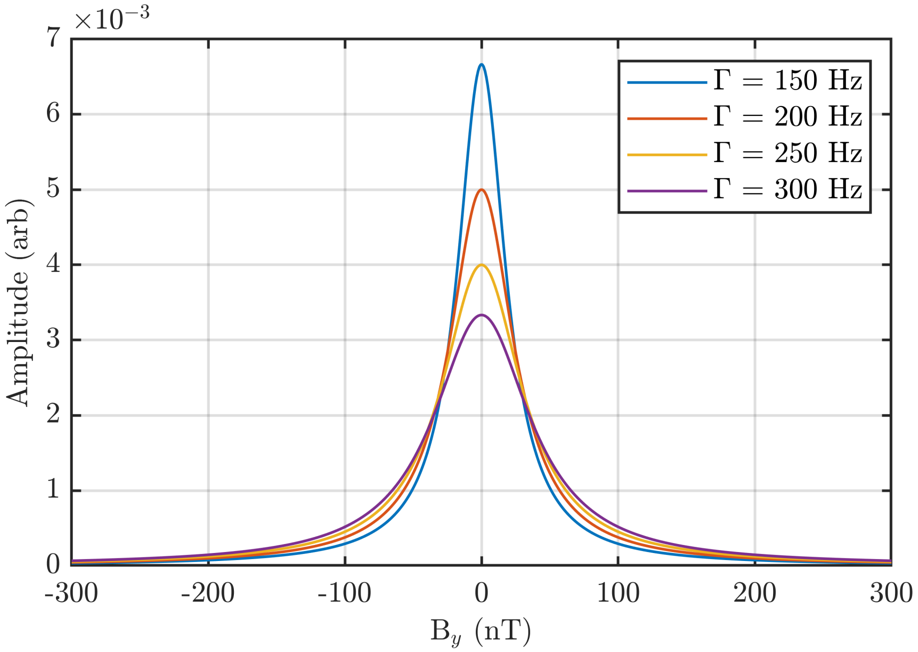

*Figure 2.12: Transverse Hanle effect with varying* Γ.

Eq 2.51 has been solved for increasing static field values along the x-axis, the results would be the same if it were along the y-axis. It has then been modelled with a static $B_x$ field and sweeping $B_z$ and shown in Fig 2.13. While there is no magnetic field being applied on the transverse plane the magnetisation along the z-axis is maximum. This is because the field and light are along the same axis meaning the atoms are always aligned in this direction giving maximum transparency and magnetisation. With an increasing field along $B_x$ the magnitude of the magnetisation along the longitudinal direction decreases as $B_z$ passes through zero field as well as broadening the resonance. The broadening is caused by the increase in spin exchange relaxation due the the depolarising transverse field [79]. As discussed earlier in Section 2.8, when there is no field the relaxation caused by spin exchange is suppressed.

Combining the effects created from Eq 2.50 and 2.51, a picture of the 2D landscape can be modelled and is shown in Fig 2.14. Looking at the landscape in this form is used in this thesis to extract the zero-field point for the two fields and discussed again in Section 4.1. In order to extract the zero-field point, a 2D Lorentzian function

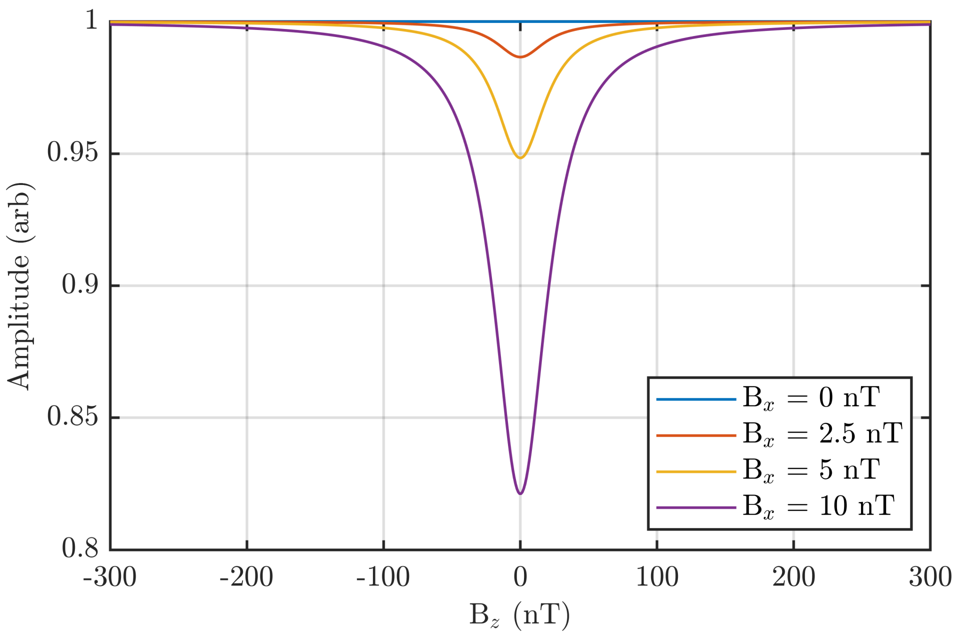

*Figure 2.13: Longitudinal Hanle effect modelled with varying transverse static field.*

is used:

$$L_{2D} = A\frac{(B_x - B_{x0})^2 + \Gamma_z}{(B_x - B_{x0})^2 + \Gamma_z + \frac{\Gamma_x}{\Gamma_z} + (B_z - B_{z0})^2} + C, \tag{2.52}$$

where $A$ is amplitude, $\Gamma_x$ and $\Gamma_z$ are the resonance widths, $B_{x0}$ and $B_{z0}$ are the resonance centres and $C$ is the offset in the y-axis. A 1D Lorentzian fit is also used to extract the parameters from raw data, which has the form:

$$L_{1D} = A\frac{1}{1 + \left(\frac{B_x - B_{x0}}{\Gamma}\right)^2} + C. \tag{2.53}$$

MIA and MIT are both common methods used for zero-field resonance detection in a single beam OPM. Another common method is polarisation rotation and is discussed in the next section.

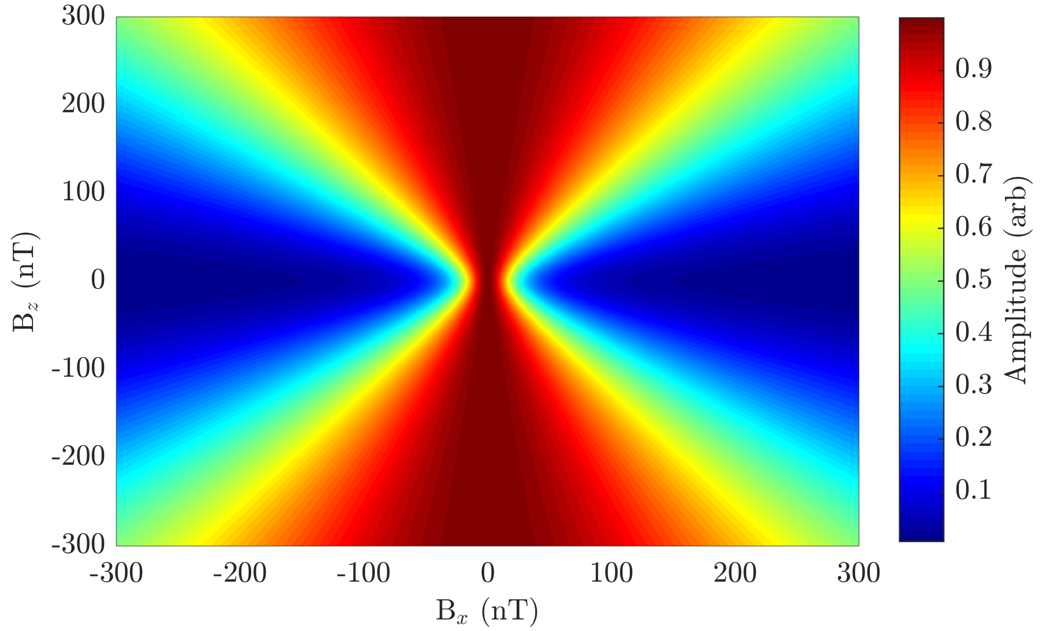

*Figure 2.14: Modelled Hanle effect in both the transverse ($B_x$) and longitudinal ($B_z$) axes. The landscape narrows as $B_z$ reaches 0 nT, with a maximum amplitude where $B_x$ is 0 nT.*

## 2.10 Polarisation Rotation

Polarisation rotation is a method of detection which utilises the fact that there is an imbalance between populations in the upper and lower hyperfine ground states. The two hyperfine ground states provide different refractive indexes for circularly polarised light. When linearly polarised light, which is made up from equal parts of left and right circular polarisations, passes through this medium it experiences the different refractive indexes. The imbalance in populations slows one of the circular components more than the other, causing the linear polarisation to rotate [80]. As the population imbalance grows, so does the amount of optical rotation experienced by the linear light:

$$\theta = \frac{\pi}{2} l \; n_A \; r_e \; c \; P_z \; f \; Im[V(v - v_0)], \tag{2.54}$$

where $l$ is the cell length and $P_z$ the population difference between the lower and upper hyperfine ground states. If the atoms are aligned along the beam axis, this is known as circular birefringence [58].

The polarisation rotation method is carried out using a balanced polarimeter which has two photodiodes where the voltages from each port are subtracted from one another. This provides a final readout showing 0 V when they are balanced. The polarimeter reaches 0 V when light with the same amount of horizontal and vertical components is incident on a polarising beam splitter (PBS) and focused in to each port of the detector and discussed further in Section 5.1. A more practical way of calculating the rotation is by knowing how much light is incident on each of the ports:

$$\theta = \frac{I_1 - I_2}{2(I_1 + I_2)}, \tag{2.55}$$

where $I_1$ and $I_2$ are the intensities of light detected in each port of the balanced polarimeter. This effect is most effectively used when using a separate probe beam, far detuned from resonance. The reason for this is so there can be efficient pumping created by a pump beam, while the probe beam can be far detuned that it does not create any pumping but still susceptible to optical rotation due to the imaginary part of the optical lineshape as discussed in Section 2.6. By using elliptically polarised light the atoms can be pumped by the circular component, but the light can also be rotated at the same time with a single beam [81].

## 2.11 Sensitivity

The sensitivity of a magnetometer is defined in units of $\mathrm{T}/\sqrt{\mathrm{Hz}}$. Measuring the sensitivity is done by taking the power spectral density (PSD) of some given data from the photodiode, in Volts. To obtain the PSD first of all a fast Fourier transform (FFT) is needed. An FFT is calculated by taking time or space domain data and converting this in to the frequency domain. The PSD can the be found from the FFT:

$$PSD = \frac{2A^2}{F_s N}, \tag{2.56}$$

where $A$ represents the amplitude of the FFT, $F_s$ is the sampling frequency and $N$ is the number of points [82]. A difference between an FFT and PSD is that an FFT has the correct amplitude in each peak and is a valid way to estimate peak amplitude but not the noise floor. The PSD on the other hand has an accurate representation of the noise floor but not the power in each peak.

The PSD has units of $\mathrm{V}^2/\mathrm{Hz}$. The square root of the PSD is needed to have units of $\mathrm{V}/\sqrt{\mathrm{Hz}}$ which is the noise spectral density (NSD). To convert this from $\mathrm{V}/\sqrt{\mathrm{Hz}}$ to $\mathrm{T}/\sqrt{\mathrm{Hz}}$, the data has to be scaled by V/T. The V/T value is found by using both:

$$X = D_m cos(\omega), \tag{2.57}$$

$$Y = D_m sin(\omega), \tag{2.58}$$

where $D_m$ is the modulated data and $\omega$ is the demodulation frequency [83, 84]. These two formulas produce the two components of the demodulated signal. This data is captured by performing a similar measurement to that described in Section 2.9.2, while also applying a secondary modulating magnetic field. The modulation is then demodulated out at the same frequency. By finding the on-resonance gradient of the $X$ component of demodulated data ($\partial B/\partial X$), the gradient can then used to scale the NSD into the correct unit form. This is the smallest change in magnetic field which the sensor can determine. Writing this in equation form:

$$\delta B = \sqrt{PSD}\frac{\partial B}{\partial X}. \tag{2.59}$$

Achieving a sensitivity by this method is a very experimental approach. However, an estimate for the photon shot noise limited sensitivity can be found by using:

$$\delta B = \frac{V}{\sqrt{N}}\frac{\partial B}{\partial X}, \tag{2.60}$$

where $V$ is the voltage recorded and $N$ the number on photons received in 1 s [42, 85]. The number of photons is calculated using the photodiode's Volts per Watt (V/W) conversion. The photon shot noise will provide the ultimate sensitivity an OPM can reach providing there are no other limiting sources of noise.

Key aspects of theory for OPMs and SERF OPMs have been discussed here. The optical resonance plays an important role in an OPMs success due to the optical pumping that can be achieved with overlapping hyperfine transitions. The magnetic resonance is equally important as its width based on relaxation mechanisms influences the OPMs sensitivity. For the SERF regime to be achieved at easily reached temperatures the alkali vapour should be experiencing as little background magnetic field as possible. Detection methods can vary between using MIA/MIT and optical rotation, each having their pros and cons which will be explored in later chapters. The photon shot noise sensitivity is the ultimate sensitivity a sensor can reach which will be compared to the sensitivities achieved in this thesis.

# Chapter 3

# Experimental Design

This chapter will discuss the design decisions made in order to build a functioning SERF magnetometer. This experiment has been designed as a lab based system in which new ideas can be trialled and proof of concepts can be achieved. Information gathered will be passed on to a more portable version designed for biomedical applications [86, 87, 88]. Because of this a few design requirements are outlined. The portable version needs to be compact, limiting the experiment to a single beam configuration. As will be discussed, material choice is important due to how a SERF sensor is operated and the equipment used to control it.

## 3.1 Overall Design

The experimental architecture is shown in Fig 3.1. A distributed Bragg reflector (DBR) laser producing 795 nm light is used, from a butterfly mount package (Thorlabs DBR795PN) and driven by a low-noise digital diode driver (Koheron CTL200). Laser calibration data is shown in Appendix B. The package has a polarisation maintaining fiber leading to a fiber collimator producing a 4 mm diameter beam, also from Thorlabs (F280APC-780). After exiting the fibre the polarisation is controlled using a combination of zero-order $\lambda/4$ and $\lambda/2$ waveplates from Union Optics (WPF4212-795-M25.4 and WPF2212-795-M25.4). The light is then converted from linearly polarised to circularly polarised before entering the five layer mu-metal shield (custom design from Magnetic Shields Ltd). Here the light passes through the rubidium vapour magnetometry cell housed within the central structure. The light then exits the shield and reaches a low-noise photodiode with a gain of 600 V/W. The custom built coil driver and heater, designed to be low-noise, are controlled using a PC [89]. This PC is also used to read in the photodiode voltage. The PC controls the coil driver and heater via USB and serial connection respectively. The photodiode voltage is read in and modulation coils are controlled via a National Instruments 16-bit DAQ (PCIe-6353). The digital control system and experiment are connected via a NI break-out BNC rack (BNC-2090A).

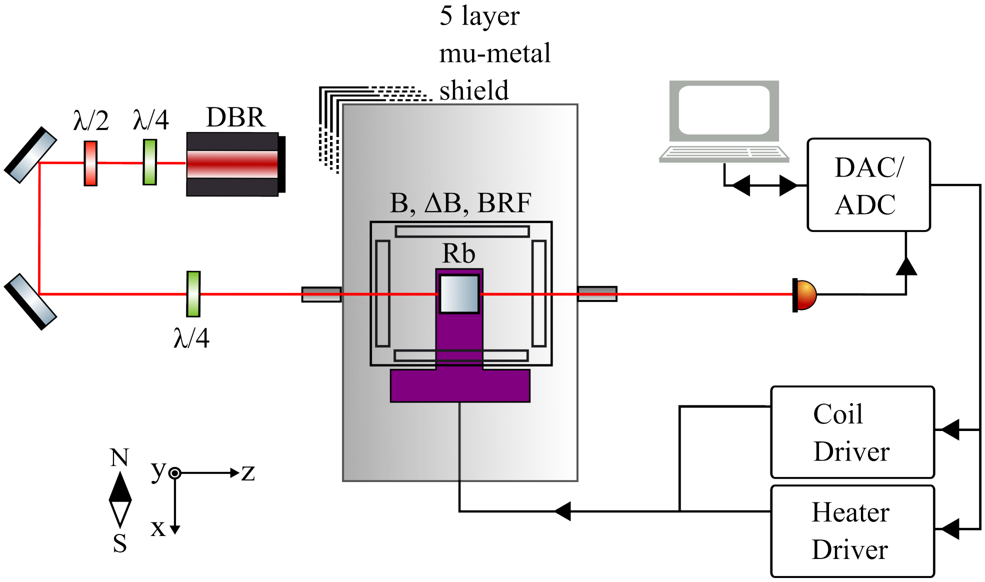

*Figure 3.1: Schematic of the experimental design. DBR laser produces 795 nm light which is converted to circular polarisation before entering the shield. Light that has not been absorbed by the atoms exits the shield and is then detected on a single photodiode.*

## 3.2 Shield

For magnetic shields to be most effective they need multiple layers. Mu-metal helps in diverting external fields, such as the Earth's field, as it has a high permeability, providing an easy path for magnetic flux to travel through [90]. By increasing the number of layers of shielding the residual field that leaks to the centre of the shields decreases. Because of this a five layer mu-metal shield, which has concentric cylindrical layers, is used. The outer most shield is 200 mm in diameter and the inner most shield measuring 100 mm in diameter. The outer shield has a length of 1208 mm, giving it an aspect ratio of just over six, while in the inner most has a length of 800 mm, giving an aspect ratio of eight. The larger aspect ratio makes it harder for the magnetic flux to bend and leak into the shields, optimising the shielding factor [91].

The Johnson noise can be a limiting factor in many experiments. For the shields commercially available the manufacturer estimates the resolution is in the region of 10 $\mathrm{fT}/\sqrt{\mathrm{Hz}}$ of low frequency magnetic fields for larger diameter shields than have been used in this experiment [92]. As the shield in this thesis is narrower than the commercially available one, it is estimated that the Johnson noise in this experiment will be higher than 10 $\mathrm{fT}/\sqrt{\mathrm{Hz}}$.

## 3.3 Centre Block

The centre block (Fig 3.2) is comprised of two parts: coil formers and magnetometry cell housing. The first set of coil formers can be seen at the top and bottom (in green) as square plates which have grooves and channels to allow easy winding of the x and y-axis coils. The x-axis coils are wound between the two green plates while the y-axis coils are wound around each of the green plates. The second set of coil formers can be seen (in red) near the centre of the block which are for the z-axis. Specifics of the coils are discussed in the next section. The magnetometry cell housing (black) is designed to locate the magnetometry cell in the beam's path while holding it in a fixed position with respect to the coils and beam. The centre block had to be designed to fit inside the five layer cylindrical mu-metal shield. The inner diameter of the inside layer is 100 mm which is the biggest design constraining factor. Other factors which had to be taken into account when designing this piece are coil geometry, magnetometry cell size, beam access and fixing it in place inside the shield all of which are discussed below.

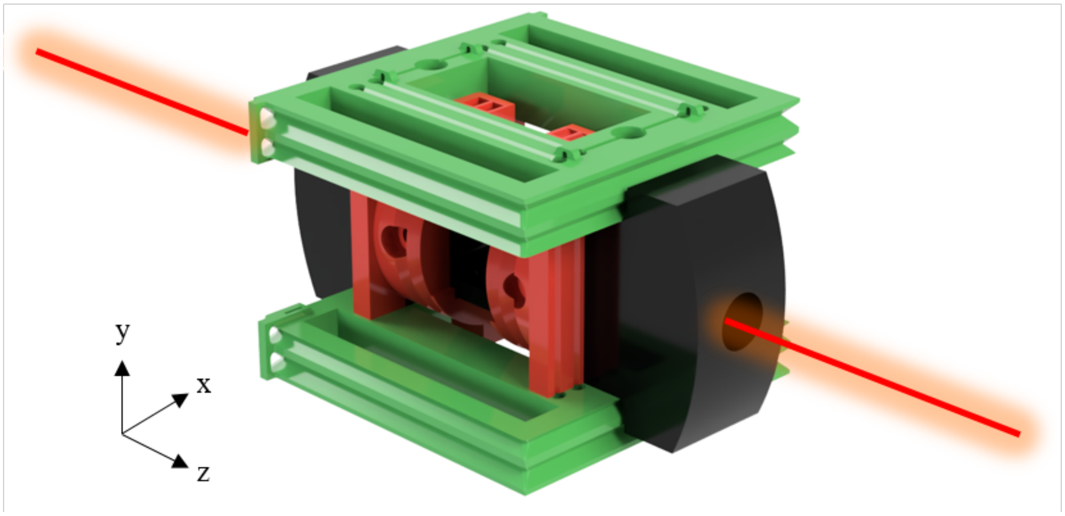

*Figure 3.2: Centre block which has coil formers as well as beam access through the holes at either end. The magnetometry cell sits in the middle of block. 3D printing allows for detailed design such as small features like tunnels for wires in awkward places.*

The central block needs to be able to withstand temperatures up to around 200°C, so Formlabs High Temp Resin was chosen [93]. This is so that the magnetometry cell can be heated to sufficiently high temperatures to reach the SERF regime without damaging the housing. Using a 3D printer allowed for cheap as well as quick production in the development stages where changes were being made frequently. The magnetometry cell sits in the centre of the block where two channels from either end meet allowing for beam access from outside the shield and allowing the light to exit. A secondary housing was also printed from the same High Temp Resin to secure the magnetometry cell to the main block. Within the magnetometry cell housing there are layers of insulation creating a more stable and even temperature. The coil formers and magnetometry cell housing were co-designed so that they are located correctly with respect to the magnetometry cell and allows for smaller details to be printed such as lugs on top of the coil formers to secure the coil wire.

## 3.4 Coils

### 3.4.1 Helmholtz Coils

Helmholtz coils are a pair of coils wound in the same direction so that a homogeneous field is produced between the pair. Helmholtz coils generally have a radius and coil separation that are matched, but in practice many teams use this name for coils that are near to this configuration. As magnetic fields surrounding current in a wire follow the right hand rule this allows for static field control in either direction along the centre of the coil pair as the magnetic fields point in the same direction. Helmholtz coils are an important part of the experiment as they are used to null stray fields that still exist within the shield. The experiment has three sets of Helmholtz coils on the x, y and z-axis. Due to the restrictions imposed by the shield's size, three coils of varying geometries were chosen. This included a set of circular coils on the beam axis (z), which are the smallest set. The other two sets are square coils and placed further away from the centre. These two sets of coils increase in size from the x-axis to the y-axis coils as shown by Table 3.1.

| Coil | $R$ (mm) | $a$ (mm) | $s$ (mm) | $N$ |
|---|---|---|---|---|
| z (circular) | 17 | - | 18.5 | 3 |
| x (square) | - | 25 | 26 | 4 |
| y (square) | - | 32 | 36 | 6 |

*Table 3.1: Helmholtz coil geometries. $R$ represents the radius of the circular coil, $a$ the half length of the side of the square coils, $s$ the separation of the coils and $N$ the number of turns as used in Eq 3.1 and Eq 3.2.*

Each coil is designed to produce similar fields for a given input current as can be seen from Fig 3.3. Even though they have varying geometries, all produce 1200 nT - 1400 nT for 10 mA. The dashed black lines at ±5 mm represent the edge of the magnetometry cell used showing that the Helmholtz coils produce very little change in magnetic field across the magnetometry cell with a variation of a few nT over the (10 mm). The fields in Fig 3.3 have been produced by modelling Eq 3.1 and 3.2 with 5 mA of current for all three coil geometries used. For circular coils Eq 3.1 can be used as an approximation for the Bio-Savart law:

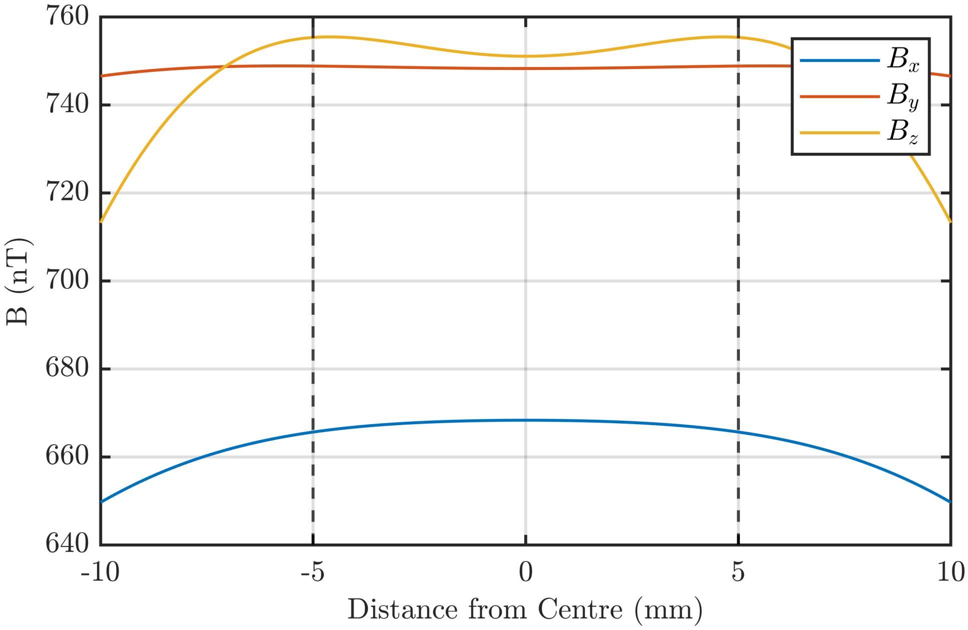

*Figure 3.3: Modelled Helmholtz coil fields with 5 mA of current produced using Eq 3.1 and 3.2. The magnetic fields produced scale proportionally with the current applied. The fields produced are similar, even though their sizes vary, by increasing by the number of turns for the larger coils. The dashed black lines at ±5 mm show the edge of the magnetometry cell so the field change across it can be seen.*

$$B_z(z) = \frac{\mu_0 N I R^2}{2}\left(\frac{1}{(R^2+(z-\frac{s}{2})^2)^{\frac{3}{2}}} + \frac{1}{(R^2+(z+\frac{s}{2})^2)^{\frac{3}{2}}}\right), \tag{3.1}$$

an for square coil:

$$B_x(x) = \frac{2\mu_0 N I a^2}{\pi}\left(\frac{1}{((a^2+(x-\frac{s}{2})^2)(2a^2+(x-\frac{s}{2})^2)^{\frac{1}{2}})} + \frac{1}{((a^2+(x+\frac{s}{2})^2)(2a^2+(x+\frac{s}{2})^2)^{\frac{1}{2}})}\right), \quad (3.2)$$

is also an approximation [94]. In both these equations $B$ represents the field produced, $\mu_0$ the permeability of free space, $N$ the number of turns of wire, $I$ the current passing through the wire and $s$ the separation of the coils. $R$ in the circular coil equation represents the radius of the coil where $a$ is the half length of the side of the square coils. The coordinate system for both equations is centred at the midpoint of the coils.

### 3.4.2 Anti-Helmholtz Coils

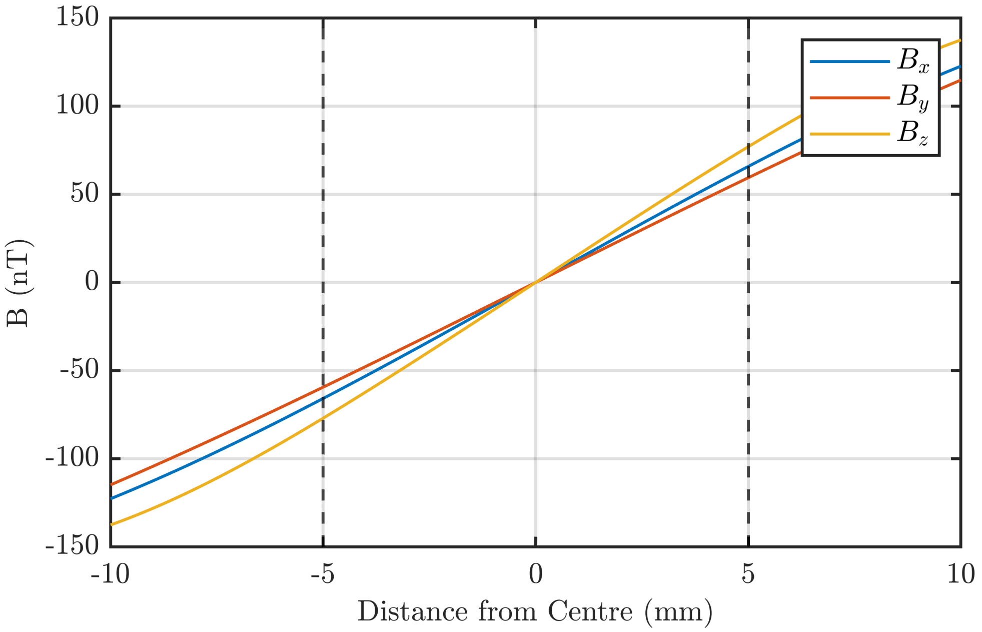

*Figure 3.4: Modelled anti-Helmholtz coil gradients with a current of 5 mA using Eq 3.3 and 3.4. The magnetic fields produced scale proportionally with the current applied. Using these equations it is clear that as you move away from the centre point of the coils a similar gradient will be experienced on all three axes due to the subtraction of the fields produced by each individual coil in the pair. The dashed black lines at ±5 mm show the edge of the magnetometry cell so the gradient produced across it can be seen.*

The anti-Helmholtz coils are wound in parallel channels to the Helmholtz coils with a circular pair on the z-axis and square sets getting larger from x to y. The difference between Helmholtz and anti-Helmholtz coils is the relative direction of current flow in the coils. Where Helmholtz has the current flow in the same direction on both coils, anti-Helmholtz has the current flow in the opposite direction in each coil. This is why the anti-Helmholtz equations have a subtraction between the fractions for each of the individual coils where the Helmholtz have an addition. Again, an approximation for the Bio-Savart law for circular anti-Helmholtz coils is:

$$B_z(z) = \frac{\mu_0 N I R^2}{2}\left(\frac{1}{(R^2+(z-\frac{s}{2})^2)^{\frac{3}{2}}} - \frac{1}{(R^2+(z+\frac{s}{2})^2)^{\frac{3}{2}}}\right), \tag{3.3}$$

and for the square coils:

$$\begin{aligned} B_x(x) = \frac{2\mu_0 N I a^2}{\pi}\Bigg(&\frac{1}{((a^2+(x-\frac{s}{2})^2)(2a^2+(x-\frac{s}{2})^2)^{\frac{1}{2}})} \\ &- \frac{1}{((a^2+(x+\frac{s}{2})^2)(2a^2+(x+\frac{s}{2})^2)^{\frac{1}{2}})}\Bigg), \end{aligned} \tag{3.4}$$

[94]. The model of Eq 3.3 and Eq 3.4 using the coils geometries given in Table 3.2 can be seen in Fig 3.4. A current of 5 mA has been used in this model to show the gradients produced by each coil is nearly matched.

| Coil | $R$ (mm) | $a$ (mm) | $s$ (mm) | $N$ |
|---|---|---|---|---|
| z (circular) | 17 | - | 26 | 1 |
| x (square) | - | 25 | 34 | 2 |
| y (square) | - | 32 | 46 | 3 |

*Table 3.2: anti-Helmholtz coil geometries. Here the variables represent the same as in Table 3.1 and used in Eq 3.3 and Eq 3.4.*

| Coil | $R$ (mm) | $a$ (mm) | $s$ (mm) | $N$ |
|---|---|---|---|---|
| Modulation | - | 32 | 36 | 4 |
| Test | - | 32 | 36 | 2 |

*Table 3.3: Modulation and test coil geometry. The modulation and test coil both have square geometries in a Helmholtz configuration with variables the same as in Table 3.1 and Table 3.2.*

### 3.4.3 Modulation and Test Coils

A modulation and a test coil were wound so additional magnetic fields can be applied to the atoms. The purpose of the modulation coil is to change the atomic orientation with respect to the lasers propagation direction. As discussed already in Section 2.9.2, as the atoms are moved from the zero field point they become more absorbent. This change in absorption is measured and discussed in the next chapters. The test coil is used to produce test signals which are detected by the atoms while they are magnetically sensitive to small fields during modulation.

The modulation coil is wound with four turns while the test coil has two turns. Current is applied to the coils using the DAC outputs directly. These are voltage devices, although capable of driving up to 10 mA on each channel. For the modulation coil, the current is limited using a 1 kΩ resistor added in series. The reason for this is that the signal applied wants to fill as much of the ±10 V range available on the digital to analogue converter to reduce digitiser noise entering the system. In order to produce the fT scale signals created by the test coil a 10 MΩ resistor was used. Although the resistor for the test coil is four orders of magnitude larger than the modulation coil, the current needed is six orders of magnitude less. This discrepancy is due to there being fewer windings on the test coil than the modulation coil.

## 3.5 Cell

A cubic borosilicate glass magnetometry cell (Twinleaf) shown in Fig 3.5 was used in the experiments described in this thesis. The magnetometry cell has inner dimensions

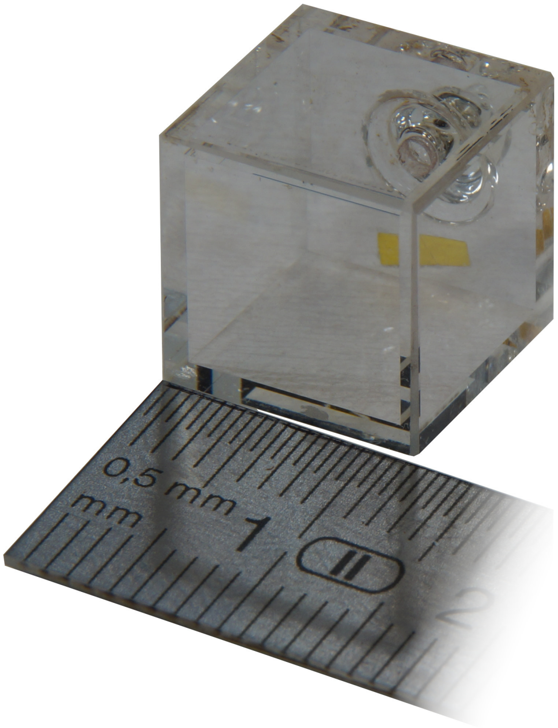

*Figure 3.5: Enriched $^{87}$Rb vapour magnetometry cell from Twinleaf used in this thesis. The internal volume is (10 mm)$^3$ with 1 mm thick borosilicate glass, giving an external volume of (12 mm)$^3$.*

of (10 mm)$^3$ and a glass stem on one side which limits the number of axes that may be practically used for light transmission. Within the stem there is a droplet of enriched rubidium-87. The magnetometry cell also contains 200 Torr of nitrogen buffer/quenching gas.

Fig 3.6 shows absorption spectroscopy for both a reference cell which has natural abundance rubidium (both rubidium-85 and rubidium-87 isotopes) and the magnetometry cell with 200 Torr of nitrogen quenching gas shown by the blue and red trace respectively. The broadening of the absorption profile and frequency shift from the reference point (0 GHz) seen in the magnetometry cell is due to the effects of the quenching gas and is a good match to that modelled in Fig 2.2.

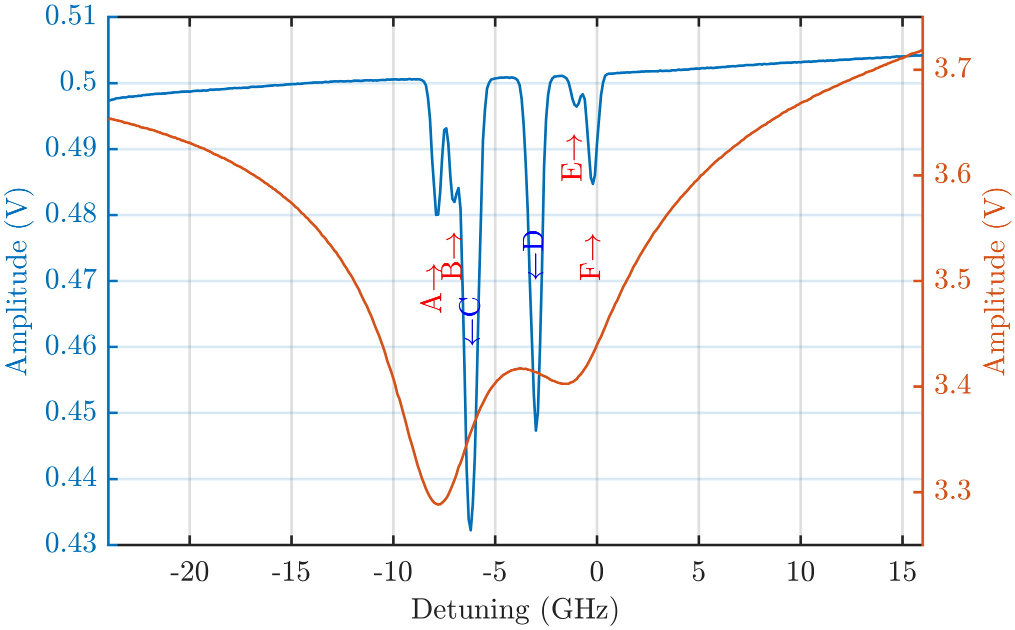

*Figure 3.6: Spectroscopy from both a reference cell (blue) and the Twinleaf magnetometry cell with 200 Torr of nitrogen quenching gas (red). A=$^{87}$Rb F=2→F'=1, B=$^{87}$Rb F=2→F'=2, C=$^{85}$Rb F=3→F'=2/3, D=$^{85}$Rb F=2→F'=2/3, E=$^{87}$Rb F=1→F'=1, F=$^{87}$Rb F=1→F'=2.*

## 3.6 Heater and Coil Driver

### 3.6.1 Heater

Two resistors are used to heat the magnetometry cell from the top and the bottom, one of which is shown in Fig 3.7. These are composed of printed circuit boards (PCBs) which have been designed such that their windings cancel magnetic fields produced. This is done by winding one surface as well as the same configuration on the reverse side of the PCB where the current flows in the opposite direction. The active area of the resistor is (12 mm)$^2$ to cover the entire magnetometry cell. Heating the magnetometry cell is achieved using AC current and two overlapping square waves at a frequency of 136 kHz. Such high frequencies are used so not to affect the region of sensitivity below 1 kHz. An efficient, low-noise, custom built driver was designed which switches between the two waveforms. The phase of the square waves are changed to control the temperature of the magnetometry cell. When the waves are 180° out of phase there is no heating

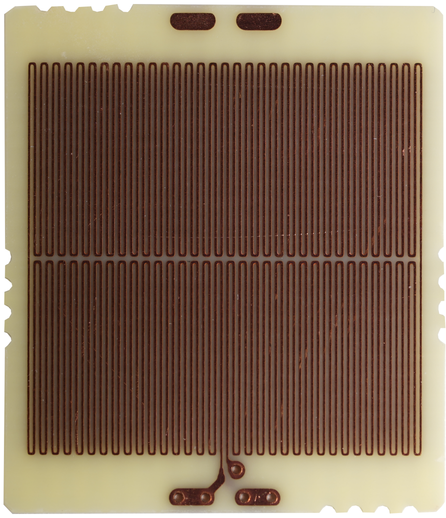

*Figure 3.7: Heating resistor with an active area of (12 mm)$^2$. The tracks are 76 μm and follow the same pattern on both sides to cancel magnetic fields produced.*

as the waves will completely cancel out providing no power. Having the waves at 0° out of phase results in heating being constantly applied to the magnetometry cell [86]. Heating calibration data is shown in Appendix B.

### 3.6.2 Coil Driver

The coil driver is also a custom built circuit designed to be ultra-low noise with a measured noise floor of 146 pA/$\sqrt{\text{Hz}}$ with a current range of ±10 mA [95]. The driver is a bipolar current source which is controlled via the computer to output the desired current. Using the modelled field to current shown in Fig 3.3 and Fig 3.4 a specific field can be requested and the driver executes the correct current. The driver has three individual channels allowing one driver to control each of the Helmholtz coil pairs individually [89].

In this chapter the design requirements to build a SERF sensor have been discussed as well as the solutions implemented in order to achieve this. Temperature resistant materials are used to construct components close to the magnetometry cell which are also non-magnetic. By using non-magnetic materials no extra stray fields are added in to the system. Larger fields require more current which in turn can potentially introduce more noise. With the use of low-noise coil drivers the remaining stray fields can be cancelled without adding additional current noise. To reach the SERF regime the magnetometry cell also needs to be heated. Using high frequency square waves for heating shifts the oscillating heating field noise away from the region of interest, outside the bandwidth of the sensor. This high frequency AC heating is paired with a non-inductive heater design which helps cancel the fields the heating produces.

# Chapter 4

# Field Zeroing and Parameter Optimisation

This chapter will describe the operating procedure of an absorption based SERF magnetometer. Cancelling residual magnetic fields is important to entering the SERF regime as this reduces the Larmor frequency of the atoms to a point where the SE collision rate is far greater and allows the exploitation of zero-field effects. The process of how residual field cancellation is achieved will be discussed as well as how the key operating parameters are optimised. These parameters include laser power, laser detuning, magnetometry cell temperature, modulation amplitude and modulation frequency. The effect of the laser power, detuning and magnetometry cell temperature have on the magnetic resonance width are discussed while the modulation parameters' effect on sensitivity is also discussed.

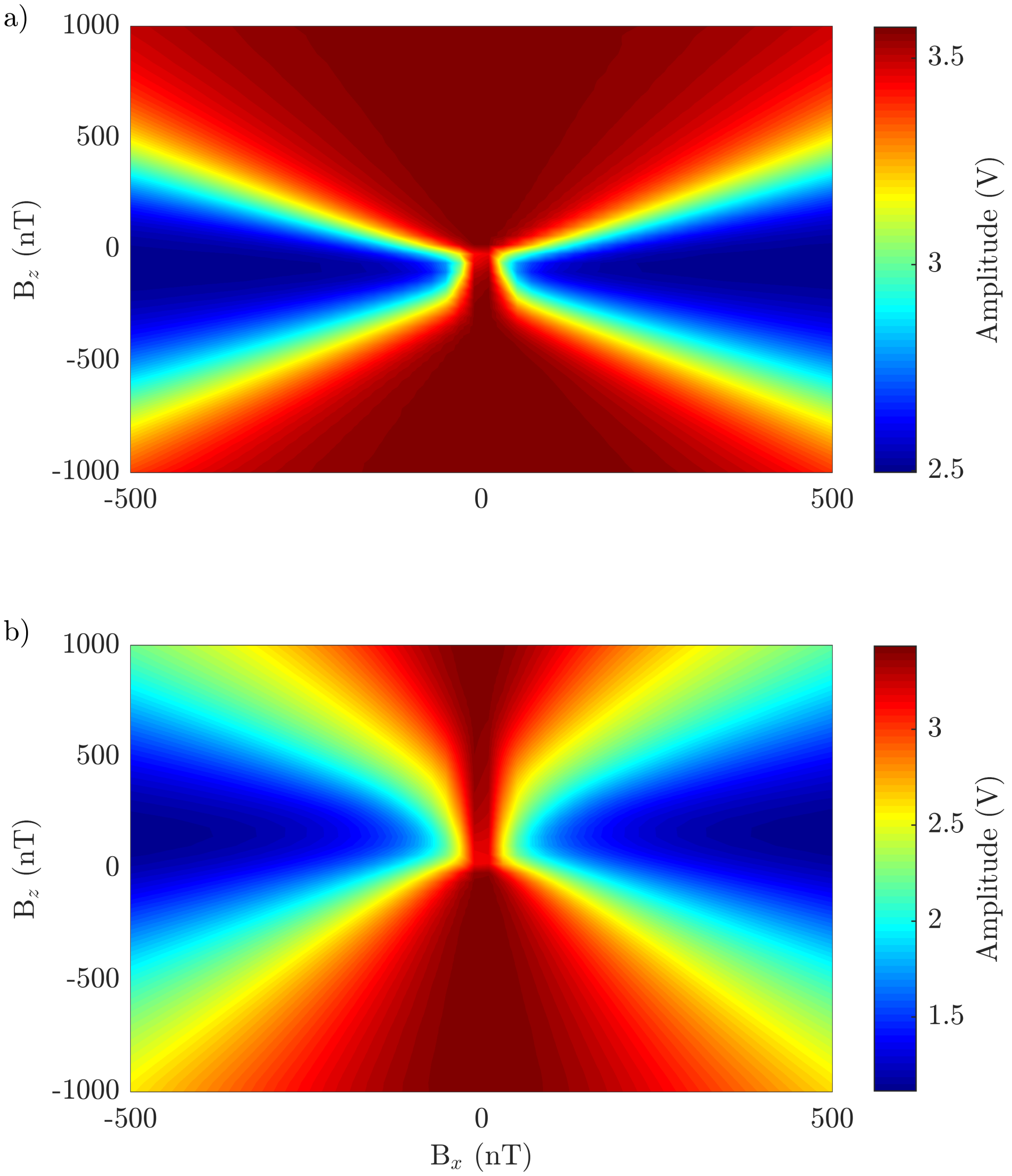

*Figure 4.1: 2D maps of longitudinal and transverse Hanle effect by sweeping $B_x$ for changing $B_z$. As $B_z$ approaches zero the width of the resonance narrows before increasing in width again while as $B_x$ approaches zero field the resonance amplitude increases. In plot a) the operating parameters are a magnetometry cell temperature of 150°C, laser power of 5 mW and laser detuning of 16 GHz, meaning the lasers detuning allows pumping on the F=1 ground state, while in b) the operating parameters are 150°C, 5 mW and -24 GHz, which will now mean the light is pumping the F=2 ground state.*

## 4.1 Field Zeroing

The first step in the experimental procedure is to null any residual and induced magnetic fields inside the mu-metal shield. To do this, the Hanle effect is used. The Hanle effect can induce either absorption or transparency based on the magnetic fields applied, as discussed in Section 2.9.2. This effect is realised by creating a series of a magnetic field sweep values which are then sent to the coil driver while simultaneously being recorded on the photodiode. First $B_z$, the field along the longitudinal axis, is set and then $B_x$, the field along the transverse horizontal axis, is systematically changed. This process is then repeated for a number of $B_z$ values until a full 2D map of the magnetic field response is built up, similar to that in Fig 2.14.

What can be seen in Fig 4.1 is a series of transverse and longitudinal Hanle resonances aligned based on the magnetic field applied. As $B_z$ is brought toward zero field the resonance in $B_x$ narrows. The experimental output aligns with what has been discussed and modelled in Section 2.9.2. The resonance amplitude also increases as $B_x$ is brought closer to zero. The amplitude of the resonance does not stay at its maximum as there is a slight residue field on the third, y-axis, still at this point. It should also be pointed out that the point where the resonance reaches its narrowest is shifted from 0 nT on the y-axis ($B_z$). This is due to the previously discussed light shift (Section 2.6) created by the circularly polarised light used which again matches the shift calculated using Eq 2.30. Using a 2D Lorentzian fit, as discussed in Section 2.9 with Eq 2.52, the points at which $B_x$ and $B_z$ values are narrowest are then extracted [96].

There is some clear asymmetry along $B_z$ in Fig 4.1a where the slope towards the narrowest point from the negative $B_z$ field values is much shallower than that from the positive side. The asymmetry can also be flipped by changing the detuning of the light from one side of the optical resonance to the other as shown in Fig 4.1b. This indicates that the asymmetry could be a product of the optical pumping created by the laser's detuning.

Once the values of the applied current have been set to achieve zero-field, the y-axis is also swept in a similar manner. The magnetic field is swept producing a single Hanle resonance. This is fit to using a single Lorentzian (Eq 2.53), extracting the width, offset, amplitude and centre.

## 4.2 Magnetic Field Modulation

Magnetic modulation is used as a way of mitigating low frequency technical noise. The modulation is created using the modulation coil discussed in Section 3.4.3. The oscillation in magnetic field changes the amount of light being absorbed by the atoms and allows the demodulation of this signal to make use of lock-in detection [97]. This is done by a using a modulation frequency in a region of low-noise, usually at high frequencies outside the bandwidth of the atoms. The static magnetic field is swept in $B_y$ and a known number of magnetic oscillations is applied at each static field point. It is important to know the number of oscillations applied as well as the frequency. If this is not the case then a non-integer number of oscillations could be applied, so when moving to the next static field value there is a step in the modulation field, which can affect the demodulation. Demodulation is carried out by multiplying the data with the carrier frequency. The $X$ and $Y$ components at each $B_y$ value are then averaged and plotted. The on-resonance slope of the demodulated signal is measured and used to scale the NSD as described in Section 2.11. The demodulation phase can also impact the amount of power that is retrieved in the $X$ and $Y$ components so optimisation of this parameter can have an impact on the overall sensitivity of the magnetometer. For this thesis all the data has a demodulation phase of $0\pi$.

Magnetic modulation is used in the case of sensors which are sensitive in the low frequency range as it removes low frequency noise, often introduced by laser light. The instability could be coupled in by either laser power or polarisation noise. The modulation can have a big effect on the sensitivity and optimising this parameter is a critical step in the experiment.

## 4.3 Modulation Parameter Scan

In order to find the optimal modulation parameters a series of scans were done varying the modulation frequency and amplitude relative to the magnetic resonance width. Doing this moves the modulation frequency from being within the bandwidth of the sensor to out of the bandwidth of the sensor. By using a high amplitude for modulation the atoms leave the SERF regime due to their increased Larmor frequency. Using a high amplitude can be compensated for by using a high modulation frequency [98]. This compensation works by scaling the frequency with the amplitude so the larger fields are coupled with higher frequencies, this in turn means the atoms cannot respond fast enough when large fields are applied due to the limited bandwidth of atoms within the SERF regime. Varying the modulation parameters results in a landscape where there is a clear single region of interest.

In Fig 4.2a there is a clear region where the demodulated slope is maximised in the low amplitude and frequency region. Modulation parameters in this region modulate the atomic sample just along the steepest part of the slope at a frequency that is within the magnetometers bandwidth. However, the steepest slope does not correspond to the best sensitivity exactly. The modulation parameters have been scaled by the HWHM as this allows for an easy comparison between the resonance width and the applied field and frequency. While the slope is maximised at around 0.4 in amplitude and 0.8 in frequency, the sensitivity is maximised at 0.7 and 1.2 of the magnetic resonance HWMH for the amplitude and frequency respectively. It is possible that the two values do not directly overlap as the frequency which returns the best slope might be a noisy region for the sensitivity. The technical noise would not affect the slope, but would affect the sensitivity.

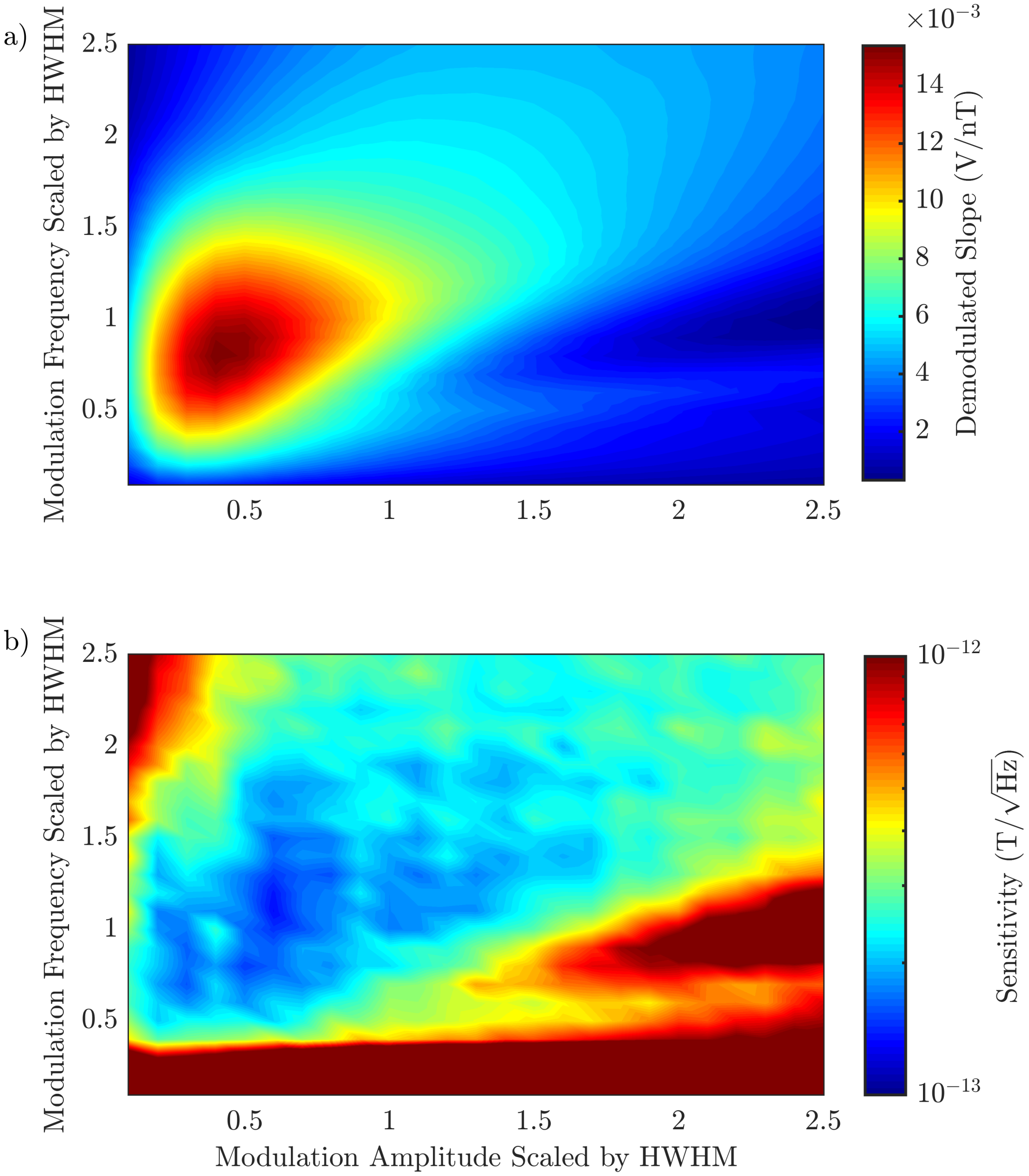

*Figure 4.2: Modulation amplitude and frequency scan for a fixed HWHM of 48 nT. By varying the modulation amplitude and frequency with respect to the magnetic resonance HWHM it can be seen where the sensor has not just the steepest demodulated slope, but also the best sensitivity. The optimum sensitivity does not overlap with the steepest slope which is at a slightly lower frequency and amplitude.*

## 4.4 Temperature, Power and Detuning

### 4.4.1 Temperature

As the modulation parameters have been discussed, this section will focus on the three remaining parameters: magnetometry cell temperature, laser power and laser detuning. The operating parameters of magnetometers are complex and not straight forward to select as the parameters discussed here would create a 5-dimensional landscape. These three parameters have direct effects on each other and the sensitivity of the magnetometer.

The magnetometry cell temperature has a profound impact on the resonance width, especially when operating within the SERF regime. As has been touched on already in Section 2.7.1, as the magnetometry cell heats and vapour becomes more dense, the SE collision rate between the alkali atoms increases, eventually reaching a point where the SE rate is far beyond the Larmor frequency. As the vapour is heated to this point the SE collisions contribution to the magnetic resonance width begins to decrease. When the SERF regime is reached atoms precess for only a fraction of the Larmor frequency in the magnetic field before undergoing a SE collision.

As the vapour density increases the amount of light being absorbed will increase since it has to pass through more atoms as described by Eq 2.39. There will become a point where the vapour becomes optically thick and light can no longer pass all the way through the magnetometry cell. As the density and SE rate increase, the magnetic resonance begins to narrow. The magnetic resonance narrowing due to the increased temperature leads to extremely narrow resonances on the order of single digit nT.

As can be seen in Fig 4.3, as the temperature is increased the amount of light that passes through the magnetometry cell initially increases. This is due to there being more atoms to absorb light when a depolarising transverse field is applied. The increased

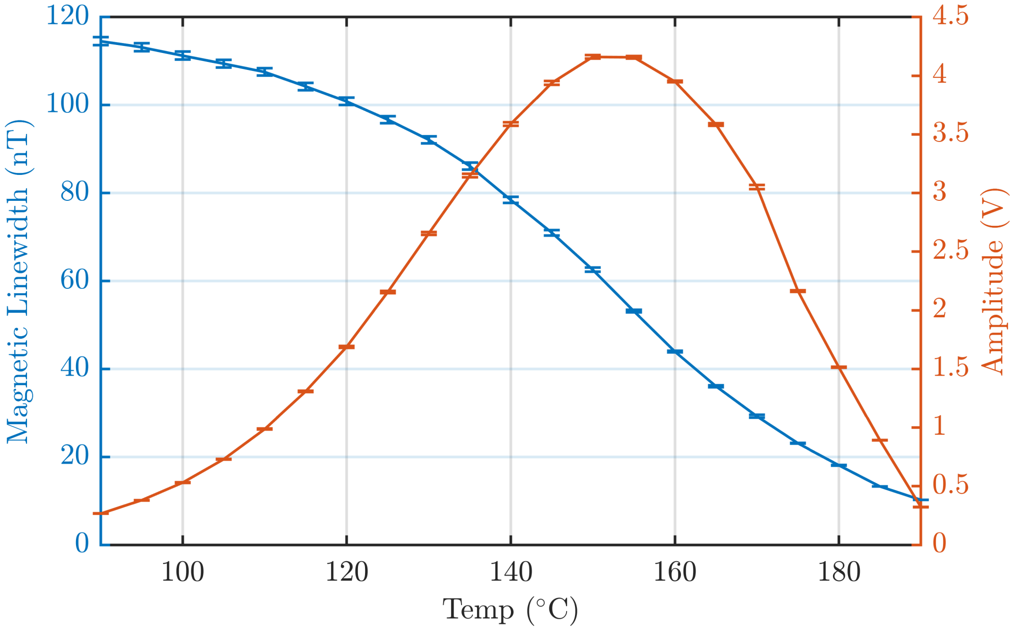

*Figure 4.3: Magnetic resonance width and amplitude for changing temperature with laser detuning of 5 GHz and power of 7 mW. As the temperature increases from 90° C - 140° C so does the amplitude. In the same range the magnetic linewidth narrows gradually. Between 140° C and 160° C the amplitude of the resonance peaks while the width has a sharp decrease. After this temperature the amplitude drops off rapidly while the linewidth begins to level out.*

absorption reduces the background offset. When the applied field passes through the zero-field point the amount of light transmitted is the same. Once the magnetometry cell temperature passes 155°C the amplitude then begins to drop. Even when the field passes through the zero-field point, more and more light is being absorbed due to the increased density and chance of depolarising collisions. It can also be seen how the resonance narrows from a HWHM of 115 nT at 90°C to a fraction of that at 190°C of 10 nT. The trend of the data shows that by increasing the temperature further the resonance would continue to narrow. The narrowing is expected to extend until around 200°C before the spin destructive collisions become the dominant relaxation mechanism and start to broaden the resonance again [58, 22]. Due to limitations within the experiment of only being able to heat as far as 190°C, data was not captured beyond this temperature. The optimal point is determined when the best ratio of amplitude to resonance width is produced. From the data it is found to be around 150°C. Varying either the laser power or laser detuning would have an effect on the amplitudes and widths measured, but the trend in the data would remain the same and will be explored in the next section [99].

### 4.4.2 Power

Laser's light will broaden the magnetic resonance, even whilst in a low power regime, below $I_{sat}$. This broadening in the low power regime is created by optical pumping and redistribution of the atoms in the magnetic sublevels. By measuring the magnetic linewidth at varying powers the data can be extrapolated to zero power and the intrinsic relaxation rate of the magnetometry cell found [99, 100].

The power of the laser has a dramatic effect on the magnetic resonance profile in this experiment. It can be seen from Fig 4.4 that using a 500 uW beam provides a narrow resonance with a $\Gamma_2$ of 7 nT, while using five times the power yields a resonance with of 31 nT. In the same range the amplitude increases by just over a factor of six. Both the width and amplitude are observed to have a roughly linear dependence on the laser power. Extrapolating the magnetic linewidth to 0 uW of power yields a $\Gamma_2$ of 2 nT. This extrapolated linewidth can be assumed to be the magnetometry cell's intrinsic linewidth at a temperature of 145°C and laser detuning of 0 GHz.

As discussed in the previous section, to increase the density of atoms in the magnetometry cell, and therefore the SE collision rate, it needs to be heated to a higher temperature. However, when the temperature is increased the amount of light detected drops off rapidly. A compromise between temperature and light detected needs to be reached. The power can be increased, but at the risk of power broadening the magnetic resonance, decreasing the sensitivity. To avoid reducing the temperature and using excessive laser power, the laser's detuning can be changed.

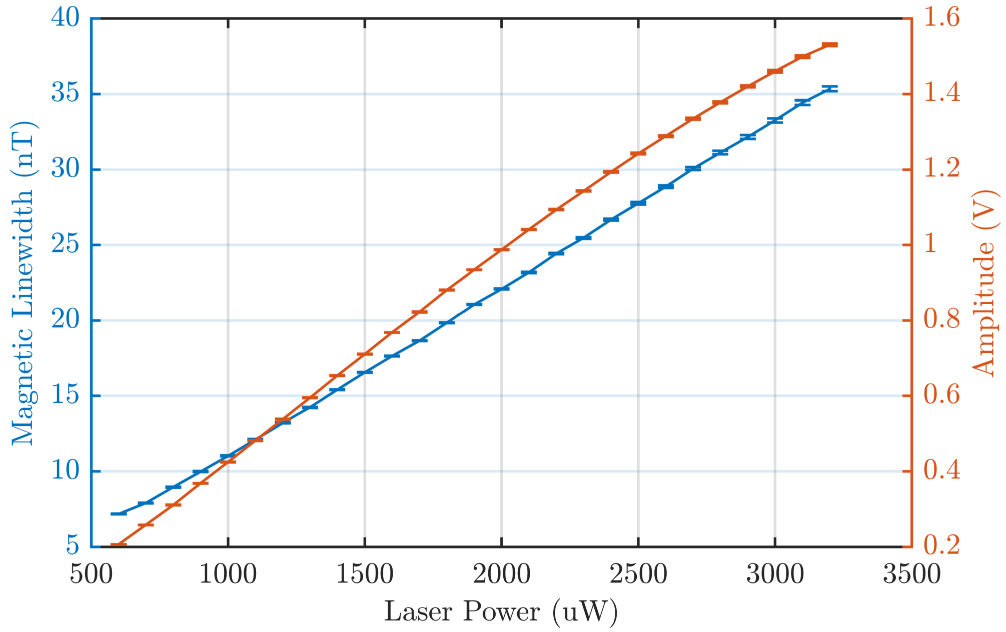

*Figure 4.4: Magnetic resonance width and amplitude for changing power with magnetometry cell temperature of 145° C and laser detuning of 0 GHz. As the power is increased both the amplitude and width increase with a near linear dependence.*

### 4.4.3 Detuning

In this experiment the laser's detuning is referenced from the highest frequency transition, $F = 1 \rightarrow F' = 2$. The rubidium transitions in this experiment are characterised from a reference cell using spectroscopy and are shown in Fig 4.5a. Here it can be seen that the $F = 1 \rightarrow F' = 2$ transition is denoted as $''F''$ at 0 GHz. As mentioned in Section 2.5, the use of buffer gas broadens the optical resonance as well as shifting it from the 0 GHz point in the reference spectroscopy. When sitting on the peak of the optical resonance nearly all the atoms' transition frequencies will match that of the light. Such a close match of atomic transition and laser frequency leads to a large portion of the light being absorbed. As the laser is moved blue and red detuned of this point fewer atoms will be able to absorb the light. The number of atoms that will be able to absorb light at a detuned point depends on the temperature and amount of buffer gas as these affect the profile in different ways. As fewer atoms absorb the light

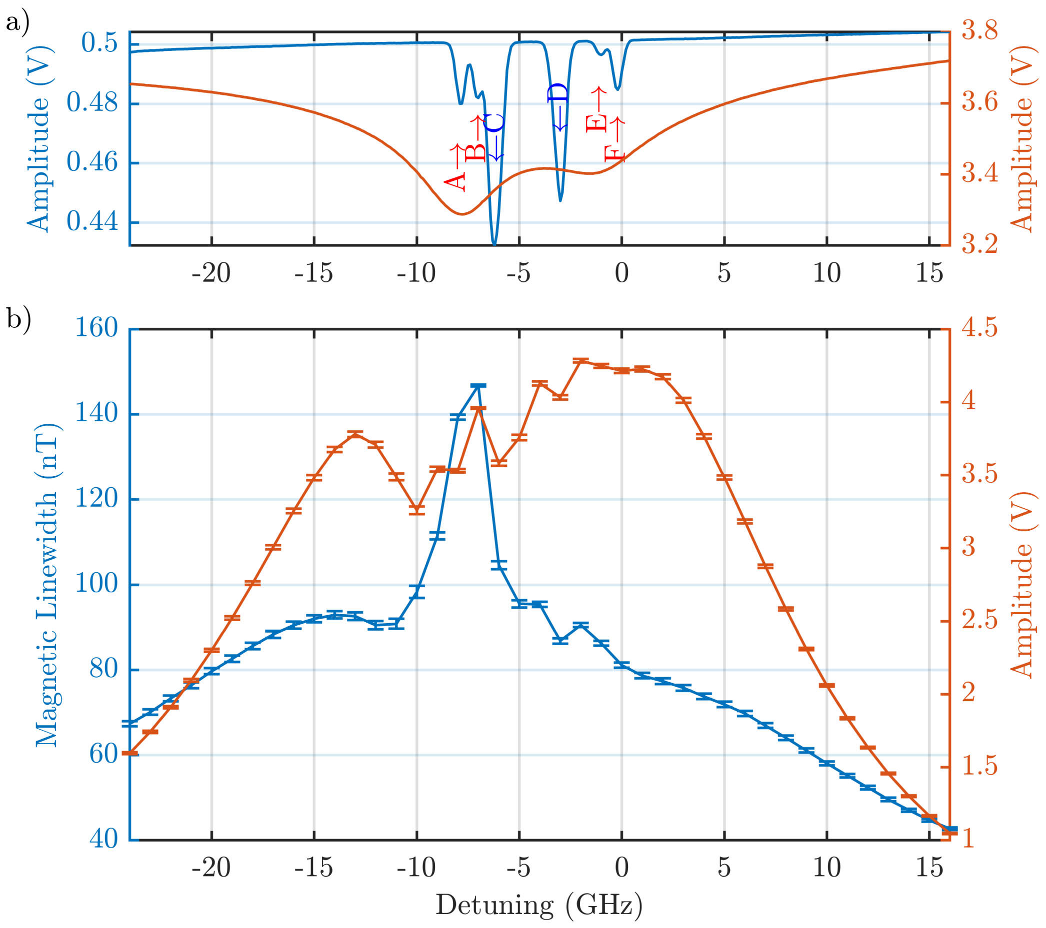

*Figure 4.5: a) Spectroscopy of both a reference cell (blue) and the magnetometry cell (red) with A, B, C, D, E and F as described in Fig 3.6. b) Magnetic resonance width and amplitude for changing detuning with a magnetometry cell temperature of 145° C and laser power of 6 mW.*

more light is able to pass through while still interacting with the non-resonant atoms. Detuning the laser too far from resonance means there is no absorption and therefore the laser can not magnetically polarise the atoms. To increase the amount of absorption the temperature could be increased or the laser is detuned closer to resonance.

Changing the laser's detuning across the optical resonance range makes the effect of optical pumping on the magnetic resonance clearly visible in Fig 4.5b. The amplitude of the resonances at each detuning varies due to the balance between the amount of light being absorbed to optically pump the atoms and that being received at the detector. As the laser approaches resonance from the negative detuning side the width increases along with the amplitude of the resonance. At -13 GHz detuned a significant fraction of the atoms become resonant with the light, which is seen by the amplitude of the resonance approaching a maximum. The large increase in resonance width seen at around -7 GHz is caused by strong pumping on the $F = 2 \rightarrow F' = 1/2$ transitions, which is trying to repopulate the F=1 ground state. However, while undergoing rapid SE collisions the atoms are statistically more likely to be found in the $F = 2$ upper ground state. This constant reshuffling of populations creates a near even distribution between the the two hyperfine ground states and thus broadening of the magnetic resonance, in an opposite manner to that of light narrowing, where the population is pumped in to one hyperfine state eliminating SE collisions [101]. The points where the amplitude peaks are around 2 GHz and -13 GHz. The reason for large amplitudes at these points is because the laser has become far enough detuned from the optical resonance peak that a lot of light is passing through the magnetometry cell but still enough is being absorbed to optically pump the atoms. The optimal point where the amplitude and resonance width produce the best ratio is in the region of 2 GHz. Here the atoms are being optically pumped on the $F = 1 \rightarrow F' = 1/2$ transition, populating the upper hyperfine ground state, increasing the magnetisation along the beam axis, leading to a narrower resonance with a larger amplitude.

It is easy to see how these three parameters are so intertwined as there is more than one set of parameters that would produce an equivalent magnetic linewidth. Finding the best combination of these three values is a time consuming task and not intuitive.

## 4.5 Optimum Parameters

To find the best combination of the previously mentioned parameters, multiple sensitivity measurements are performed by varying the magnetometry cell temperature as well as laser's detuning and power in order to build a 3D map of the sensitivity landscape. In every sensitivity measurement the fields must be zeroed by performing a new 2D and 1D magnetic field scan, as a change of either laser power or detuning will change the light shift experienced by the atoms as well as temperature affecting the resonance width. By plotting the demodulated mV/nT and sensitivity for varying power and detuning, the landscape shows the combined effects when changing the parameters.

To find the optimum parameter a systematic search of the parameter space is carried out. This involves setting the magnetometry cell temperature and systematically changing the laser's power and detuning to cover the desired range. The ranges chosen for each parameter are as follows: laser detuning from -24 to 16 GHz in 2 GHz steps, laser power from 1 to 8 mW in 1 mW steps and changing the magnetometry cell temperature in steps of 5°C from 130°C - 170°C. The data in Fig 4.6 shows a clear region where the mV/nT slope is best, on the positive detuning side of the optical resonance. This region coincides with the transitions from lower ground state being resonant, pumping the atoms into the upper ground state. This is also why the best magnetometry cell temperature is relatively high, making sure the atoms are in the SERF regime, but not so high the light is completely absorbed. The best temperature was found to be 150°C, which when looking at the Fig 4.3 matches the region where the amplitude is highest while the resonance width is quite narrow. The power and detuning combination found to give the best sensitivity were 7 mW and 6 GHz.

A complete set of data for the full temperature range can be found in Appendix C.

## 4.6 Absorption Sensitivity Measurement

Using the optimal parameters found in the previous section a sensitivity measurement is performed. After any static fields in the shield have been nulled a modulating magnetic

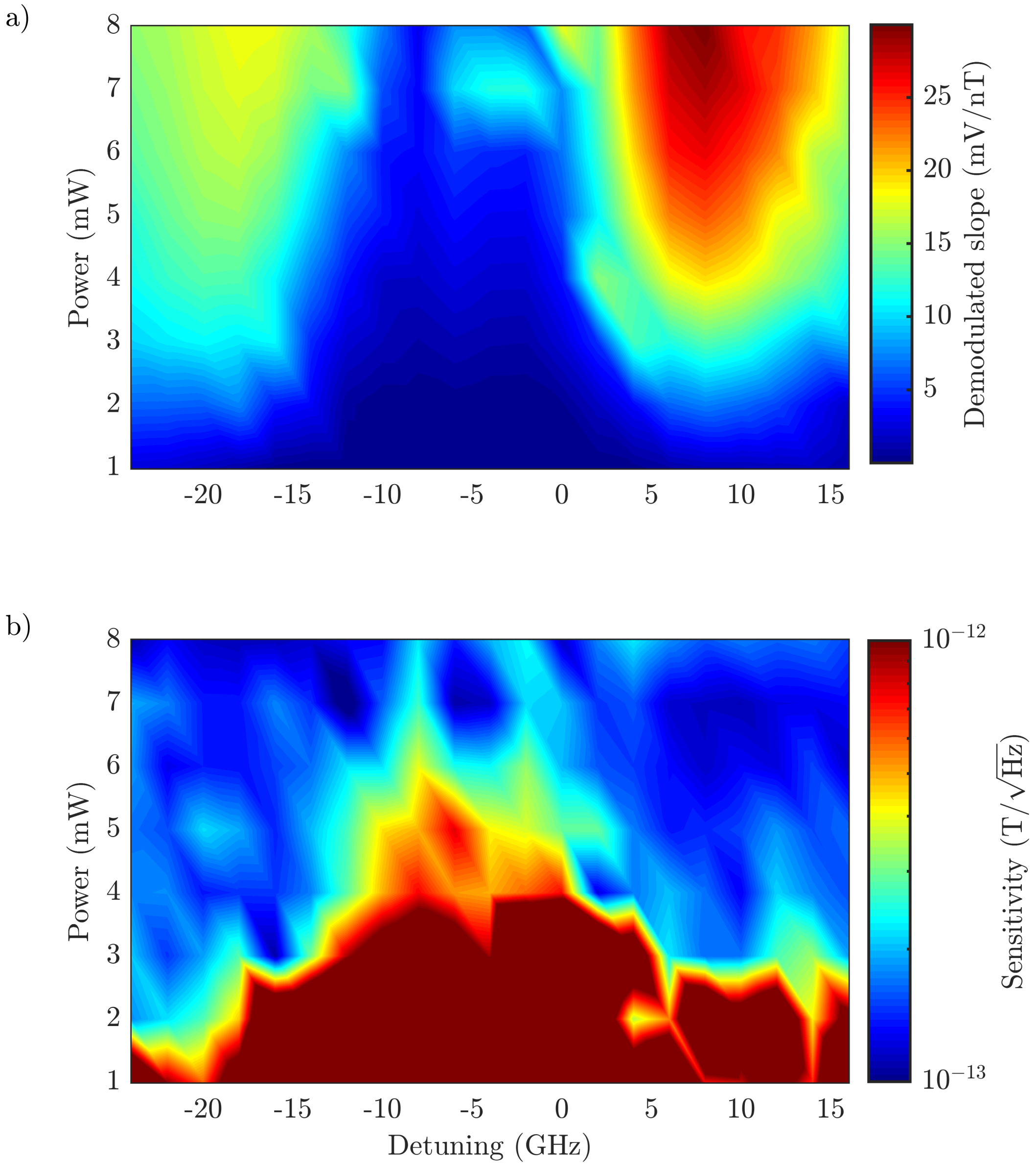

*Figure 4.6: Laser power and detuning parameter slice at 150° C. This slice shows how the demodulated slope and sensitivity vary with power and detuning. There is a clear region of poor performance below 4 mW. The top left of both plots is pumping the $F = 1$ ground state which has been shown already to provide broader magnetic resonances with lower amplitude. The optimal parameters for the best sensitivity are close to 6 GHz and 7 mW.*

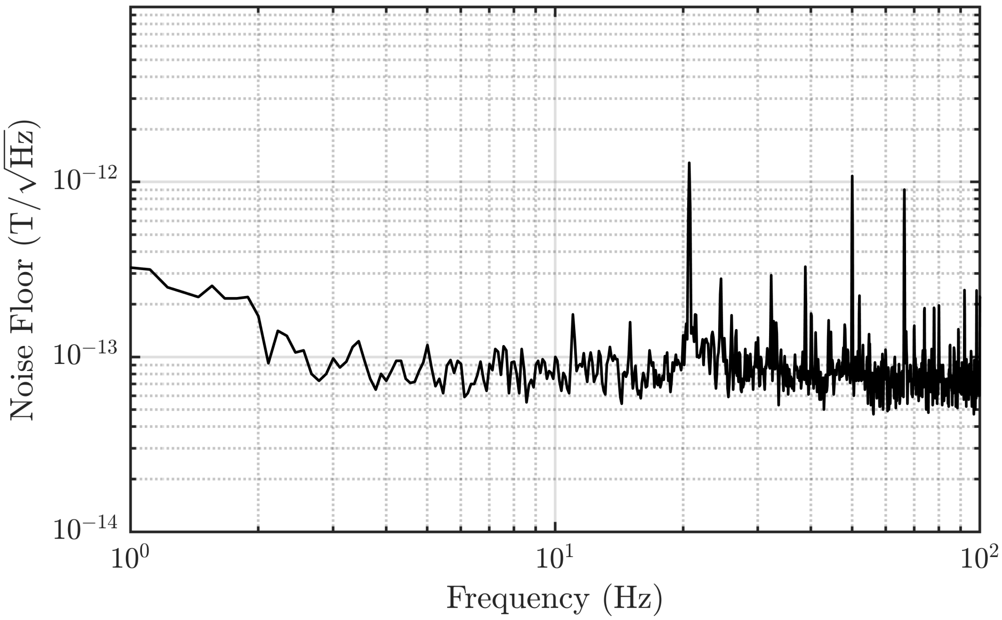

*Figure 4.7: Sensitivity measurement carried out at the optimal parameters found in Sections 4.3 and 4.4. A sensitivity of 70 $fT/\sqrt{Hz}$ is achieved above 5 Hz. At frequencies below this point there is a decrease in sensitivity. There is also noise at a number of discrete frequencies introduced by the environment.*

field is applied at the optimal modulation parameters determined in Section 4.3. The photodiode is synchronized with the magnetic field modulation to start recording at the same time the field is applied. The data is then demodulated at the modulation frequency and converted to a noise spectrum following the same process as described in Section 2.11. A single data capture consists of a 10 s long exposure which is then converted to a NSD. Ten of the exposures are performed and averaged after they have been converted to a NSD. Averaging the data this way gives an average of the noise floors, rather than averaging the time series data before converting it to a NSD as this would give an average of the noise. What this achieves is averaging out the more random noise while repeatable ″noise″, such as the mains signal at 50 Hz is not affected. The sensitivity between the frequencies of 1 Hz - 100 Hz is shown in Fig 4.7.

A value for the sensitivity is calculated by performing an average on the NSD in a region where there are no large features. The large peaks seen in the data are introduced by the environment, the largest of which are just above 20 Hz. The source of many of these is unknown except for the mains at 50 Hz. It is speculated that they are caused by vibration in the shields layers. There is a small amount of 1/f noise present in the system with the sensitivity decreasing in the region below 5 Hz. This is thought to be introduced by the instability within the laser's optical fibre.

The operating temperature of the magnetometry cell is optimised by finding the best ratio of magnetic resonance amplitude over width which is easily determined from Fig 4.3 to be 150°C. Laser power and detuning are a bit more intertwined with the best parameters coming out at 7 mW and 6 GHz measured with respect to the reference cell 0 GHz transition: $F = 1 \rightarrow F' = 2$. Modulation amplitude and frequency are found to be dependent on the magnetic linewidth. The best parameters are found to be when the amplitude comes out to be around 0.7 of the HWHM of the magnetic linewidth and 1.2 for the frequency. A combination of all of the parameters discussed here achieved a sensitivity of 70 fT/$\sqrt{\text{Hz}}$.

# Chapter 5

# Polarisation Rotation

This chapter will cover the operation of a polarisation rotation based SERF magnetometer. The experimental procedure is the same as that discussed in the previous chapter but the atoms' response is interrogated using a balanced polarimeter. The main benefit of using a balanced polarimeter comes from the common mode noise rejection. This can reduce the noise floor, increasing the sensitivity of the sensor. Here the optics used in order to build a single beam polarisation rotation based setup will be discussed as well as the operational parameters used to achieve the best performance of the sensor. The operational parameters are again laser power and detuning, magnetometry cell temperature as well as the modulation amplitude and frequency.

## 5.1 Design

The experimental design has one main difference to that of the absorption based setup in the previous chapter. The form of detection has been changed from absorption to balanced polarimetry in this chapter. The additional components are shown in

Fig 5.1. As has been touched on in Section 2.10, in order to obtain polarisation rotation there must be a linear polarisation component in the light. However, for SERF magnetometry and to create a Hanle resonance, circular light is still needed for optical pumping. Because of this criterion the circularly polarised light used in the absorption measurements is changed to elliptically polarised. The change in polarisation is done by using a combination of 795 nm zero-order $\lambda/2$ and $\lambda/4$ waveplates from Union Optics (as described in Section 3.1) to modify the light polarisation before it enters the shield. The detection stage is made up of a PBS, mirror and commercial differential detector (New Focus Large-Area Photoreceiver 2307) with 40 dB common-mode rejection ratio and high bandwidth (up to 1 MHz) [102]. The $\lambda/2$ waveplate after the shield is used to analyse the polarisation rotation of the beam after it has passed through the atoms. It is rotated to a point where the light has even amount of horizontal and vertical polarised components so that when it passes through the PBS the light is split equally between the reflected and transmitted ports. The transmitted and reflected light is then focused on to the polarimeter's photodiodes. The polarimeter is balanced when the output of the balanced detector is 0 V. The gain of the balanced detector is roughly double that of the single photodiode previously used, with a gain of 1200 V/W.

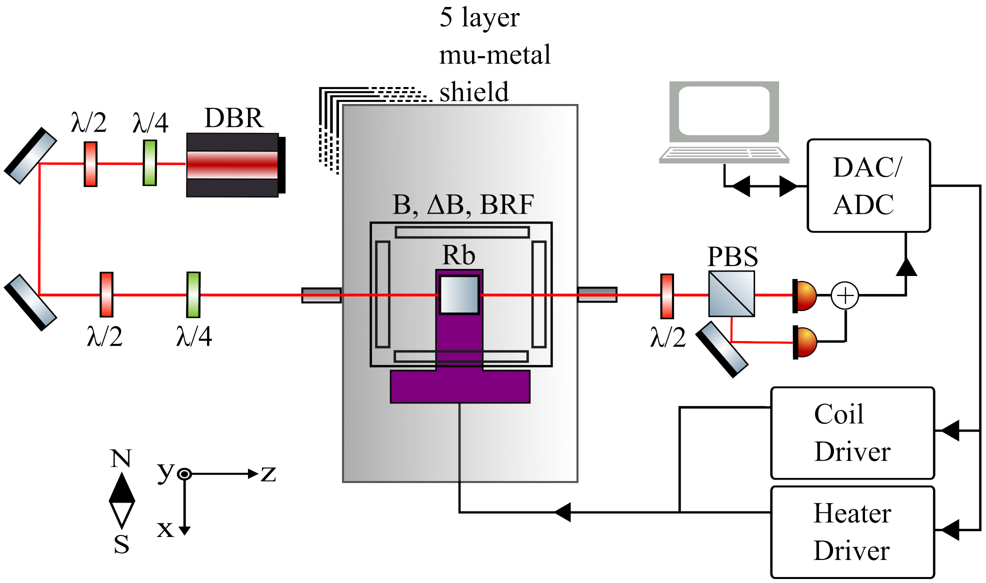

*Figure 5.1: Schematic of the experimental design. DBR laser produces 795 nm light which is converted to elliptically polarised light before entering the shield. The circular component of the light is used to pump the atoms while the linear component is optically rotated. Optical rotation is then detected on a balanced polarimeter.*

## 5.2 Noise Cancellation

The main reason for using balanced detectors is to take advantage of common mode noise suppression. As the photodetector subtracts the signals from each port, fluctuations in the amount of light received at both of the ports can be eliminated. The fluctuations must be in-phase in order for the cancellation to work and can be effective for sources of noise such as laser power instability. Low frequency 1/f noise, as well as any noise contributed by the environment such as vibrational noise, are areas which usually benefit from this technique as they tend to be common mode [103]. It is thought that through vibration of the optical components, in the case of this experiment, that noise is introduced by the air conditioning units in the lab. Vibrational noise is imprinted on the intensity of the beam and as a result it becomes common mode in both ports of the balanced detector, which cancels it out. In Fig 5.2 it is shown how much of the noise in both ports is common mode and successfully removed. There is also a reduction in the low frequency range, reducing the contribution of 1/f noise slightly in the 2 Hz - 8 Hz range. Smaller features that have been suppressed include features at 10 Hz and larger features between 20 and 50 Hz. The remaining noise can be attributed to polarisation noise being converted to intensity noise at the PBS. As the polarisation varies the power down each port of the balanced detector will change. This makes the noise in each port not common mode.

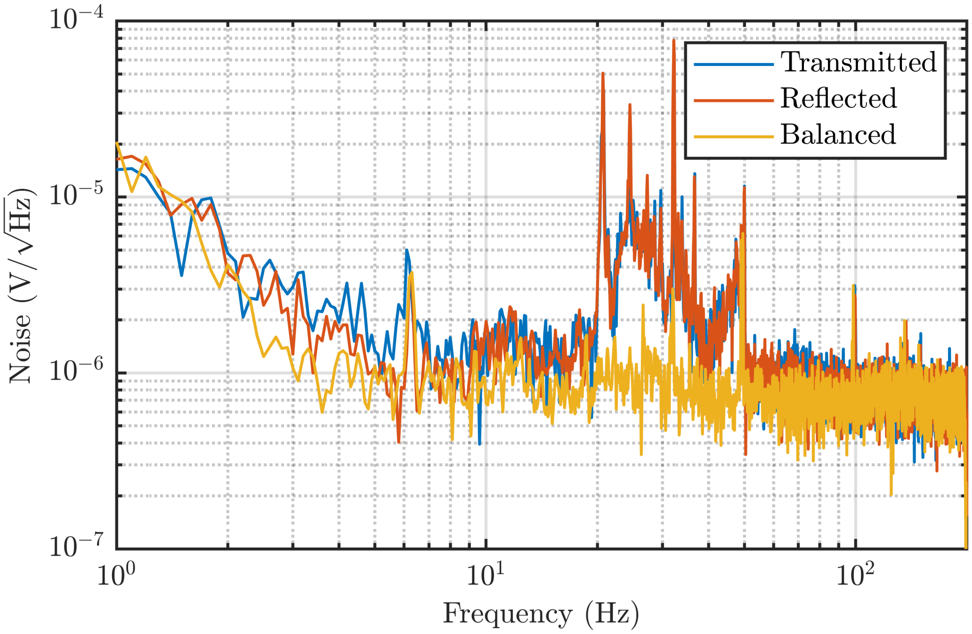

*Figure 5.2: Common mode noise rejection from the balanced polarimeter. By blocking the transmitted and reflected channels individually it can be seen that they both have noise in the 20 Hz - 50 Hz region. When they are both unblocked this noise is cancelled resulting in a much cleaner noise floor.*

## 5.3 Optical Rotation Field Zeroing

Field zeroing is carried out in much the same way as discussed in Section 4.1. The fields $B_x$ and $B_z$ are systematically changed until a complete 2D magnetic resonance is created. Instead of the absorption change being measured for changing magnetic field, the rotation of the linear component is measured. It can be seen in some circumstances where the light rotates by more than $\pi/4$. This swings the light from one component of

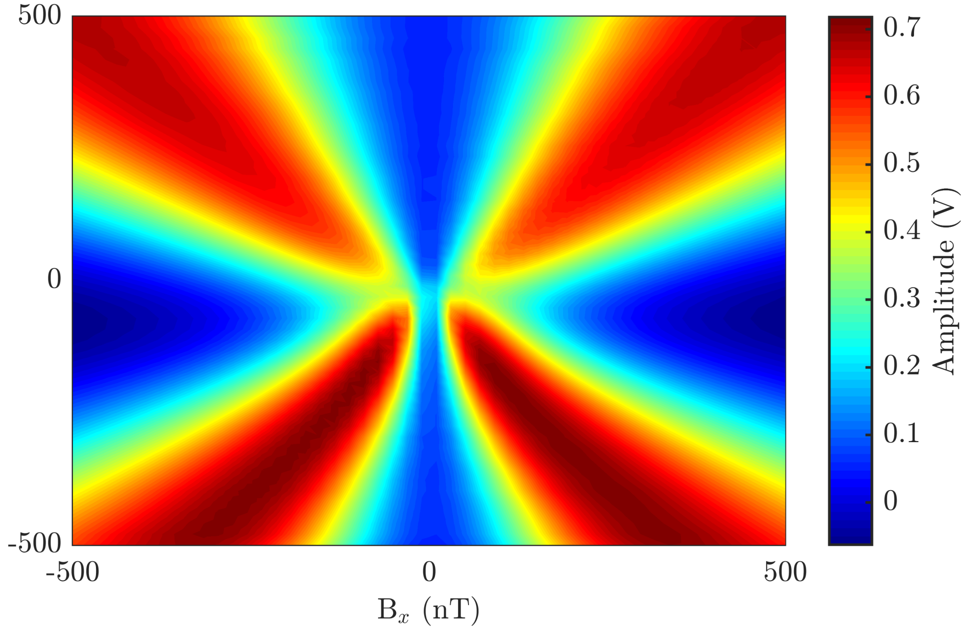

*Figure 5.3: 2D polarisation rotation created by sweeping $B_x$ for discrete static field values in $B_z$. The rotation of the light polarisation can be seen going from 0 V when balanced to a maximum where the light is either vertically or horizontally polarised and then over-rotating back to 0 V.*

linear polarisation (horizontal or vertical) to the other. On the balanced detector this is observed as the voltage going through a cyclic motion of increasing and decreasing voltage seen as the magnetic field passes through zero field and shown in Fig 5.3 [81, 104]. As the amount of rotation observed is based on the magnitude of the bias field, the rotation should be symmetric around the zero field point. However, as seen in Fig 4.1, there is asymmetry created along the beam axis which is thought to be induced by optical pumping.

When the field has a large bias on a transverse plane to the beam axis, the medium exhibits linear birefringence which is seen when $B_x$ is ±500 nT and $B_z$ is just below 0 nT. Linear birefringent media slow down one of the linear components of the light. By slowing down one of the linear components the ellipticity changes but the same portion of linear light of each component still reaches the PBS. As the transverse field is reduced (or longitudinal field increased) the atoms begin to align along either the bias field on the z-axis or be aligned by the beam itself, turning the vapour circular birefringent. As has been mentioned, since linearly polarised light is made up from equal parts of left and right circular polarisations, as the amount of circular birefringence increases one circular component of the light is slowed down more than the other. This leads to the angle of the linearly polarised light rotating [103, 105, 106].

As the light's polarisation in this configuration is elliptical there is noticeably less light shift created than in the absorptive configuration with respect to $B_z$. With $s$ in Eq 2.30 representing the light's polarisation with circularly polarised light being $s = \pm 1$ and linearly polarised light being $s = 0$, elliptical light scales the light shift between these two values. The asymmetry is also less pronounced than in Fig 4.1. As there is less light shift created, the effects of the optical pumping are also reduced.

## 5.4 Modulation Parameters

The modulation parameters can be mapped out following a similar method as described in Section 4.3. This is again done by systematically varying the amplitude and frequency of the modulation field based on a scaling of the HWHM of magnetic resonance. Looking at Fig 5.4a there is a clear area of steeper demodulated slope and sensitivity in the low frequency and amplitude region at the bottom left between 0.1 and 1 on the amplitude and on the frequency axis. There is a band surrounding the area of high demodulated slope and sensitivity in the low frequency and amplitude regime where both mV/nT and sensitivity drop off before rising back slightly.

Using this data the modulation parameters were set to 0.3 for the modulation amplitude and 0.7 of the modulation frequency based on the HWHM. Although the modulation frequency is well within the HWHM of the magnetic resonance it does not pose any risk to the frequencies of interest of biomagnetic signals due to the large linewidths created in the optical rotation based sensor, a topic that is discussed in the next sections.

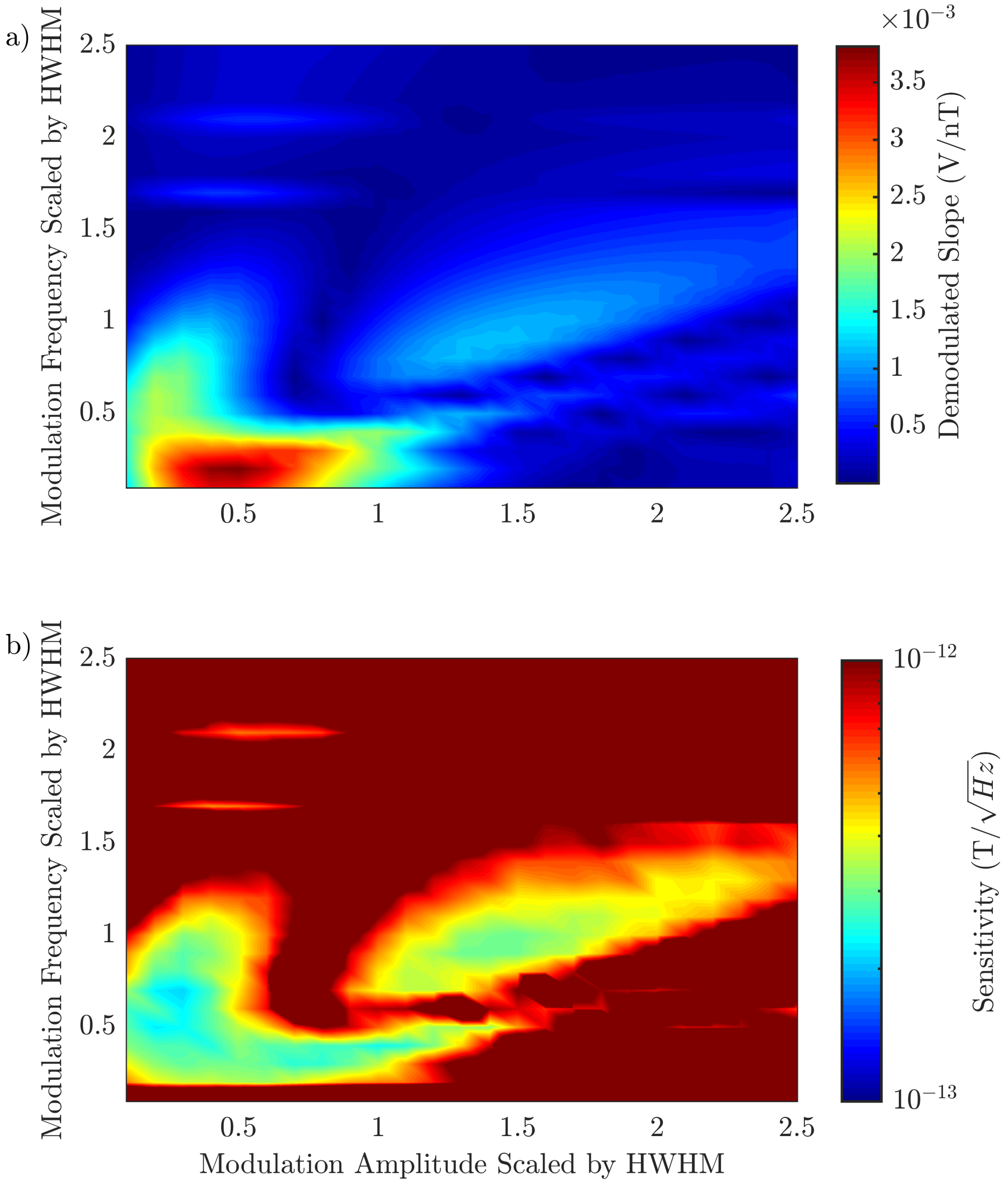

*Figure 5.4: Amplitude and frequency scan for a fixed HWHM of 126 nT. By varying the modulation amplitude and frequency with respect to the magnetic resonance HWHM it can be seen in a) where the sensor has not just the steepest demodulated slope, but also the best sensitivity in b). A second region of good sensitivity appears at amplitudes from 1 to 2.5 and frequencies from 0.5 to 1.5 based on the HWHM. The steepest slope and best sensitivities are at different values again with the steepest slope being at lower amplitude and higher frequency than the best sensitivity.*

## 5.5 Temp, Power and Detuning Parameters

### 5.5.1 Power Based Rotation

The balancing of magnetometry cell temperature, laser power and laser detuning when using polarisation rotation is similar to when doing an absorptive measurement. Each parameter has a similar effect on the magnetic resonance by creating more or less optical rotation. In order to create sufficient population imbalance between the upper and lower hyperfine ground states to achieve optical rotation there has to be enough pump power, as can be seen from Fig 5.5a. A $\pi/4$ rotation is completed each time the Lorentzian inverts on itself. By taking the ratio of the amplitude of the first inversion and the point where the rotation has stopped in the high field regime, the amplitude of one $\pi/4$ rotation is found. This can then be used to determine how far past this point the light has been rotated by using the value reached at 0 nT and converting it to fractions of $\pi$. The data shows that there is a change in the amount of rotation achieved by increasing the laser power shown in Fig 5.5b. The amount of rotation increases between the power values of 1 to 5 mW and then decreases between 6 to 8 mW. This decrease in rotation beyond 6 mW could be caused by power broadening of the optical resonance, creating more optical pumping to the neighbouring hyperfine ground state, decreasing the population imbalance. However, this change in optical rotation is not as drastic as when compared to the laser's detuning.

### 5.5.2 Detuning Based Rotation

As the detuning is varied the amount of optical rotation observed changes, which are shown in Fig 5.6. This rotation goes from less than $\pi/4$ producing a near Lorentzian lineshape when the detuning is far from resonance, to more than $\pi$ when on the steepest part of the optical resonance, measured between ±500 nT. Large amounts of rotation are achieved due to the detuning of the light with respect to the optical resonance. As shown in Eq 2.54, the rotation is a function of the imaginary part of the optical

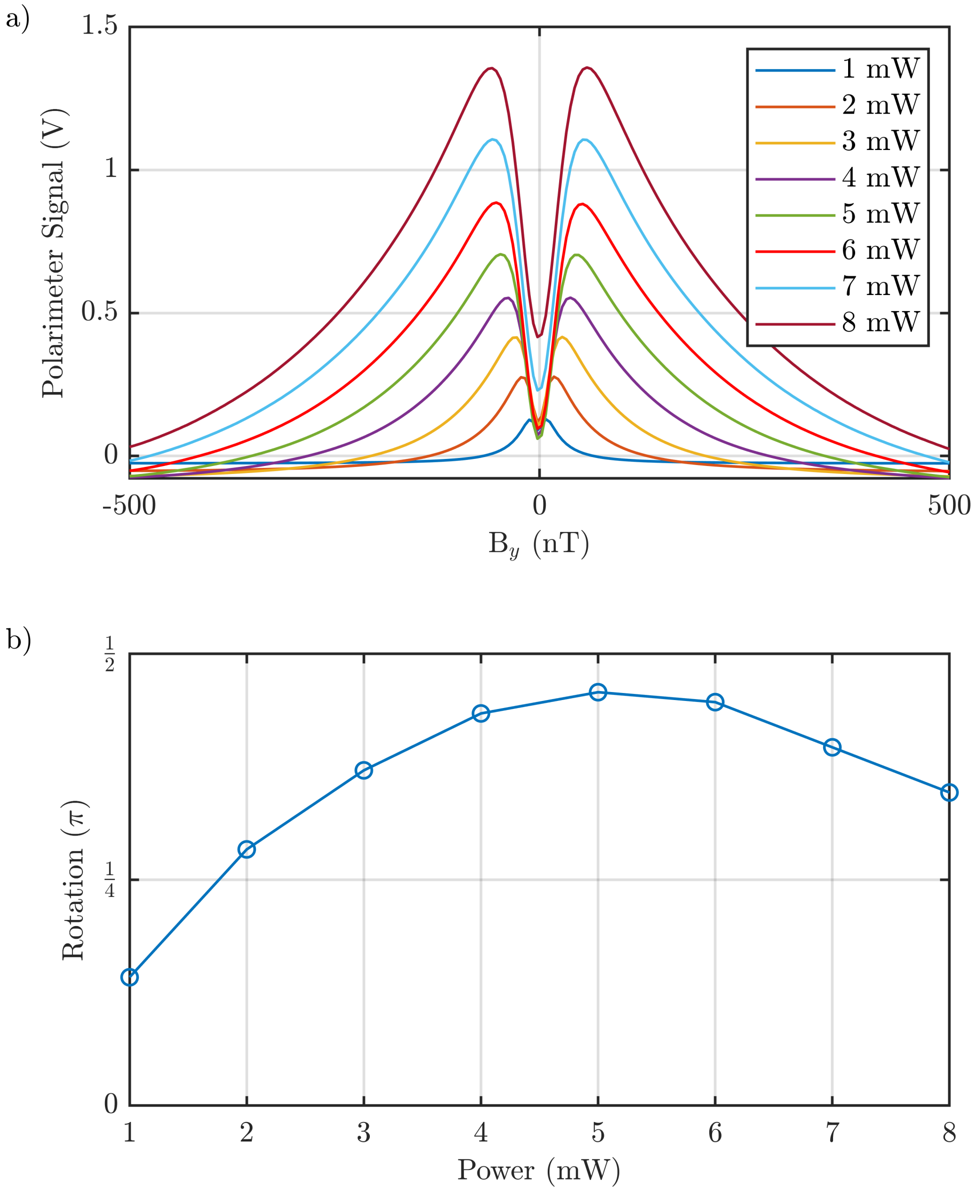

*Figure 5.5: Optical rotation measured by sweeping $B_y$ for different laser powers at a detuning of -20 GHz and 140° C. a) As the laser power is increased the magnetic resonance broadens and amplitude increases. The optical rotation increases from 1 to 5 mW before starting to decrease again towards 8 mW. b) The difference between peak amplitude and 0 nT amplitude, converted to optical rotation in terms of $\pi$.*

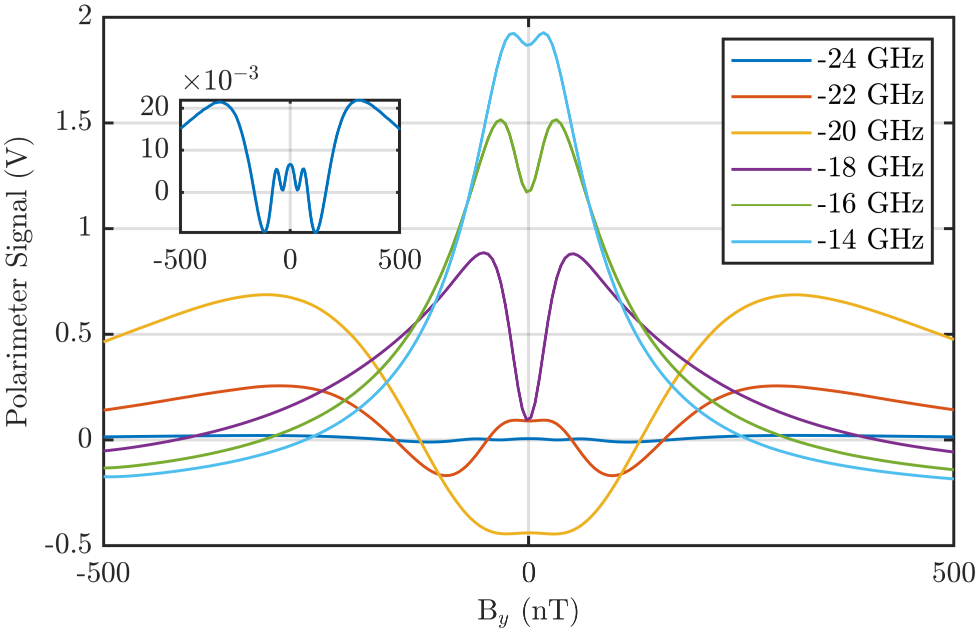

*Figure 5.6: Optical rotation measured by sweeping $B_y$ for different laser detunings between -24 and -14 GHz at 6 mW and 140° C. The amount of rotation at different detunings varies greatly as seen here. As the detuning approaches the steepest section of the optical resonance the rotation increases from just over $\pi/4$ at -24 GHz to full $\pi$ rotation at -14 GHz, shown in the insert.*

resonances, similar to the light shift created by circularly polarised light. Since the rotation drops off as function of $1/\Delta$ rather than $1/\Delta^2$ for the absorption, there is a balancing act between having enough optical pumping and light transmitted through the magnetometry cell to achieve the best amount of optical rotation. When the light is detuned to the steepest part of the optical resonance profile, the most rotation is achieved due to the relationship between the real and imaginary parts as discussed in Section 2.6. This increase in rotation and absorption is also seen in Fig 5.6. As the amount of rotation in the light increases, the signal amplitude drops due to absorption. While the light is detuned to -14 GHz the most rotation is achieved. However, at the same point the amplitudes of the signal are extremely low. By detuning from -14 to -24 GHz the amount of light passing through the magnetometry cell has increased by two orders of magnitude.

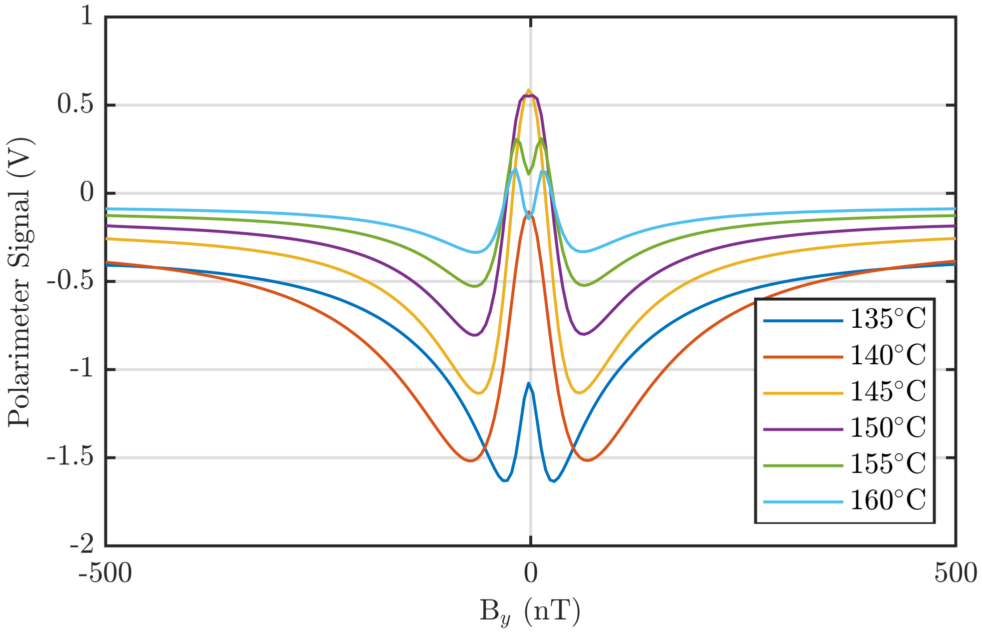

*Figure 5.7: Optical rotation measured by sweeping $B_y$ at different temperatures for fixed laser parameters of 6 mW and 6 GHz. As the temperature of the magnetometry cell is increased the amount of rotation the light experiences also increases. The resonance amplitude increases up to 145° C before it starts to decrease due to the increased absorption.*

### 5.5.3 Temperature Based Rotation

As the temperature of the magnetometry cell is increased, the density of the alkali vapour also increases. This increase in density allows the light to interact with more atoms as it traverses the magnetometry cell. This is shown again by Eq 2.54 as it has a dependence of the alkali density, $n_A$. The relationship between optical rotation and magnetometry cell temperature is shown in Fig 5.7. Even at 135°C, the light is already being rotated by more than $\pi/4$ as it has one inflection. As the temperature is increased the feature grows, showing that the light is being rotated further. This behaviour continues up to 150°C. After this point the light has been rotated by more than $\pi/2$ which is shown by the second inflection becoming visible. It is also worth noting as the temperature is increased the resonance amplitude increases as well as narrows between 135 and 145°C. After this point at higher vapour densities, more light is absorbed, diminishing the signal.

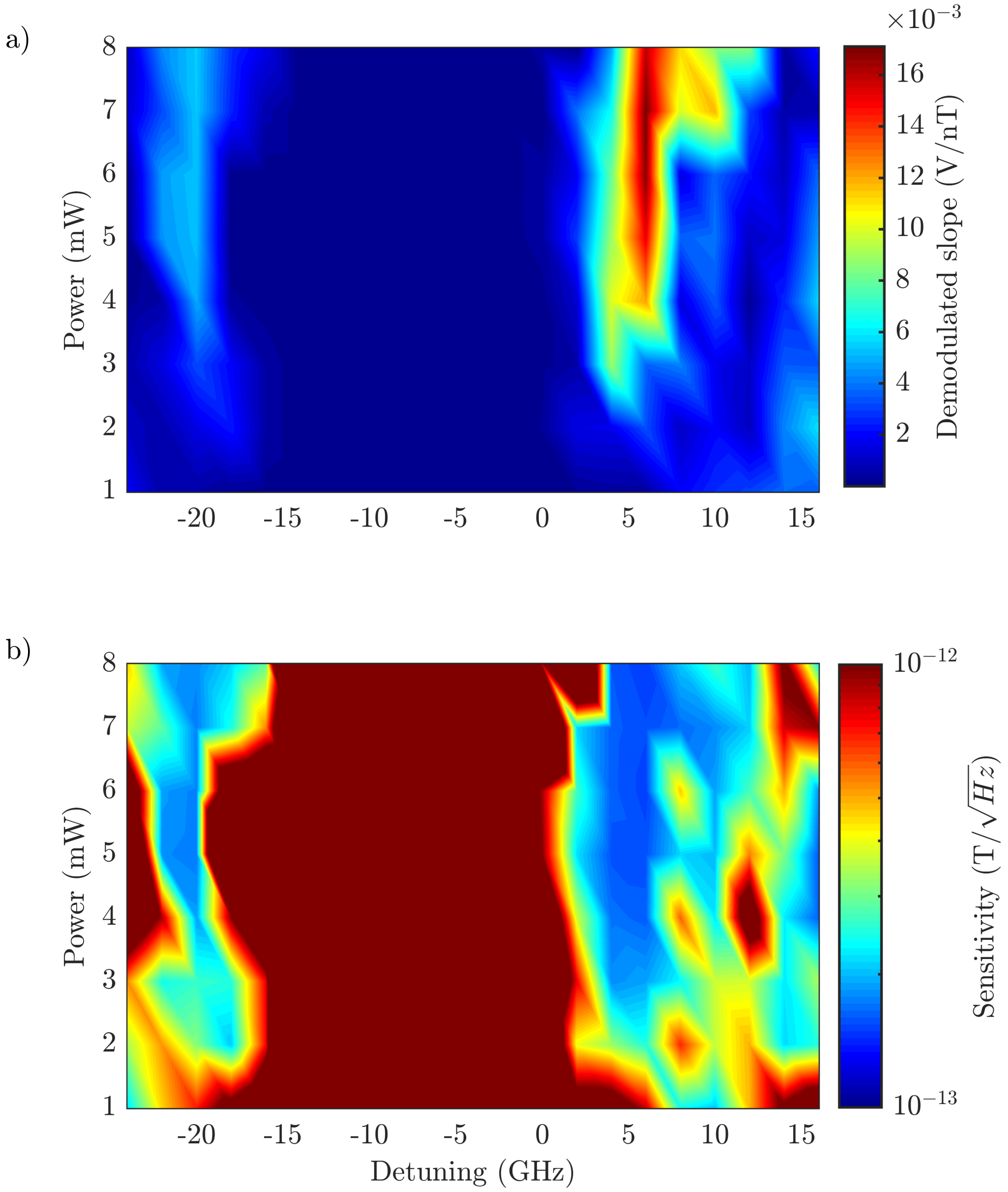

*Figure 5.8: Laser power and detuning parameter slice at 140° C. This data shows how the demodulated slope (a) and sensitivity (b) vary with power and detuning. It is clearly seen that the optical rotation does not perform well between -15 GHz and 0 GHz due to increased absorption and less efficient pumping of the elliptical light. There is a region near -20 GHz of good performance where both the demodulated slope and sensitivity are high. However, the region at 5 GHz has higher demodulated slope and sensitivity. This is due to the pumping of the F=2 ground state at -20 GHz compared to the F=1 ground state at 5 GHz.*

## 5.6 Optimal Optical Rotation Parameters

The parameters that returned the best sensitivity were found by carrying out a large systematic scan of the laser power, detuning and temperature, similar to that already discussed in Section 4.5.

The effects of moving the laser's detuning towards resonance are seen in both the demodulated slope and the sensitivity. The large amount of absorbed light gives a much shallower slope and therefore sensitivity, shown by the large blue section in the middle of Fig 5.8a and red region respectively in Fig 5.8b. Moving to the wings of the optical resonance is where the best sensitivities and demodulated slopes are found. The reason for the positively detuned side being better than the negatively detuned is due to the fact that when the laser is positively detuned it is pumping the lower hyperfine ground state more. This pumping of the $F = 1 \rightarrow F' = 1/2$ causes a slight build-up in the upper ground state without power broadening the magnetic resonance. The optimal parameters for the optical rotation setup were a laser power of 6 mW, detuning of 8 GHz and a magnetometry cell temperature of 155°C.

## 5.7 Optical Rotation Sensitivity Measurement

Following the same process for data capturing as discussed already in Section 4.6, a sensitivity measurement for the optical rotation based sensor is carried out. The data between 1 and 100 Hz is shown in Fig 5.9. The most noticeable feature in this data is the large decrease in sensitivity below 10 Hz, reaching 2 pT at 1 Hz. This is thought to be an effect of the laser's optical fibre polarisation instability, introducing a lot of non-common mode noise at the PBS before reaching the detector. Above 10 Hz the data is much flatter. Even with the common mode noise cancellation some noise is not removed from the system with discrete peaks at frequencies such as 20, 21, 39 and 50 Hz, for example. This could be because the noise is not imprinted on the laser's light,

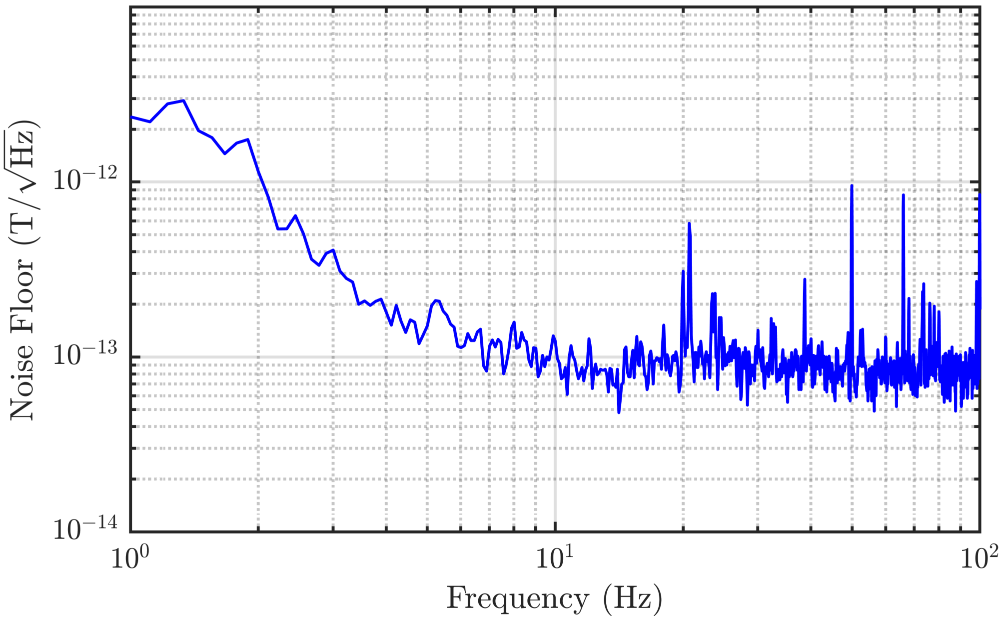

*Figure 5.9: Sensitivity measurement for the optical rotation based sensor. A sensitivity of 70 fT/$\sqrt{Hz}$ is achieve above 10 Hz. The large increase below the 10 Hz is likely attributed to the laser's optical fibre instability.*

but somewhere else, either intrinsically in the components of the sensor, or magnetic noise in the region of the sensor.

## 5.8 Different Light Polarisation

The light used in this section so far has been set with the linear component at 45° and elliptically polarised. The ellipticity of the light was tuned by rotating the the $\lambda/2$ waveplate while performing 1D magnetic scans to find the point where the amplitude of the resonance was maximised. The ellipticity provides light to both pump with the circular component and to interrogate the atoms through rotation of the linear polarisation. By using completely linear light on any axis, the pumping efficiency drastically drops off, reducing the amplitude of the magnetic resonance which is clearly visible in Fig 5.10. This amplitude reduction coupled with no reduction in resonance width leads to a much shallower slope on demodulated data. The differing amplitudes

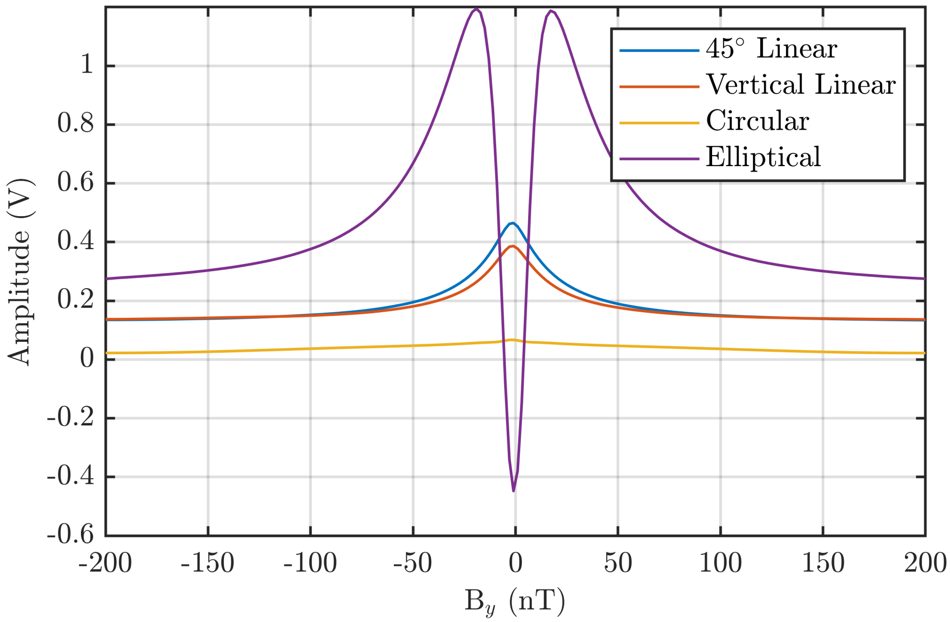

*Figure 5.10: Optical rotation measured by sweeping $B_y$ with different light polarisation; parameters used are 150°C, 6 mW and 8 GHz. Elliptical light provides the largest amplitude as well as the most rotation. The circular polarisation data has very low amplitude in comparison to both the linear and elliptical as there is no linear component to rotate. The linear components provide rotation but low amplitude as there is a lack of efficient optical pumping.*

of the two linearly polarised data sets could be due to there being a small amount of circular light in the 45° data since this is only controlled by hand, rotating the waveplate angles. Using completely circular light results in a very different shape in the magnetic resonance. The amplitude is far smaller due to the lack of rotation created as there should be close to no linear component. As there is still a small peak, it can be assumed the light still had a small amount on linearly polarised light. All four different polarisations produce HWHM of 25 nT while the amount of rotation in elliptical light and amplitude of the resonance is far greater.

The cancellation provided by the balanced polarimeter allows for a reduced noise floor and eliminates sources of common mode noise. This reduction in the noise floor can help increase the sensitivity of the magnetometer. However, the use of only one beam for both optical pumping and rotation reduces the demodulated slope as there is not as efficient pumping from the elliptical light compared to completely circularly polarised light. The less efficient pumping cancels out the improvement gained from common mode noise cancellation. The optimal operational parameters are a magnetometry cell temperature of 155°C with laser power and detuning of 6 mW and 8 GHz. A combination of all of the optimised parameters discussed here achieved a sensitivity of 70 fT/$\sqrt{\text{Hz}}$. The next chapter will explore and compare the sensitivities achieved using the both the absorptive method from Chapter 5 and optical rotation based method discussed in this chapter.

# Chapter 6

# Sensitivity Measurement Comparison, Signal Recovery & Limitations

In this chapter the sensitivity of the single beam Rb SERF magnetometer is compared for the previously discussed absorption and optical rotation based sensors. Discussion of the suitability of each of the absorptive and optical rotation operational methods as well as signal recovery in the absorptive method will be carried out. Improvements which were made to the sensor's operation will be commented on as well as the limiting factors reached in the experiment.

## 6.1 Best Sensitivity Parameters

The optimal parameters for the absorptive and optical rotation operational methods are close in terms of their laser power, laser detuning and magnetometry cell temperature, but they do diverge in their modulation parameters. For the absorptive mode the parameters which returned the best sensitivity were a laser power of 7 mW, detuning of 6 GHz and magnetometry cell temperature of 150°C as found in Chapter 4 and for the optical rotation mode they were 6 mW, 8 GHz and 155°C from Chapter 5. The slight differences in parameters could be because the rotation is based on the dispersive component of the optical resonance. As shown in Section 2.10, due to the dispersive component there is still good rotation at detunings beyond those optimal for the absorption based measurement. The optical rotation is also based on the density of the alkali atoms performing better at higher temperatures and as shown in Fig 5.7. By comparison, the absorptive measurement drastically worsens at temperatures above 155°C due to the decreasing amount of light being received at the photodetector. This decrease in amplitude can have a negative impact on the sensitivity. The absorption of the light also reduces as the inverse square of the detuning, where the rotation is reduced at the inverse of the detuning, meaning it needs to operate closer to resonance.

## 6.2 Modulated 1D Resonances

To show the observed difference in the form of signals we examine the demodulated signals for both the absorption and rotation detection methods. The plots shown in Fig 6.1 are produced at the optimal parameters for the respective experiments. The signals of the demodulated $X$ and $Y$, as discussed in Section 2.11, for both the absorptive and optical rotation produce the same shapes, with the absorptive plots being larger in amplitude and width. The gradient of the amplitude and width ($\partial B/\partial X$) around the zero crossing is also steeper for the absorptive curve with 18 mV/nT compared to 12 mV/nT for optical rotation. In order to maximise the resolution when operating on the resonance slope, the DAQ limits are set so that the demodulated signal fills as much of the range as possible.

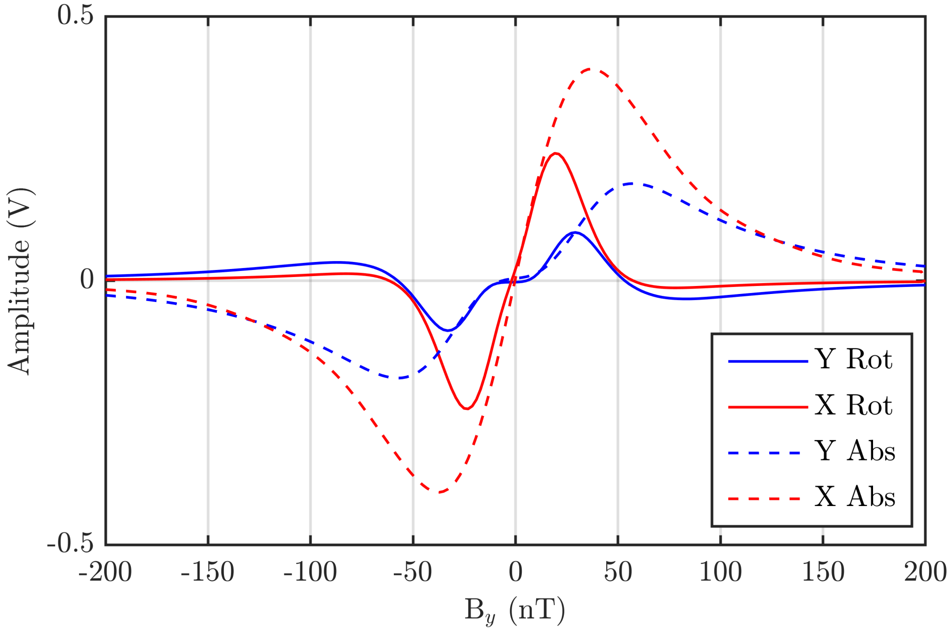

*Figure 6.1: Demodulated data at the best sensitivity parameters for both the absorptive (dashed) and optical rotation (solid) based experiments. It is seen here how the demodulated X components of the optical rotation compares with the absorptive. The absorptive setup returned a steeper on-resonance gradient than that of the optical rotation. The gradients are 18 mV/nT for the absorptive and 12 mV/nT for the optical rotation. There is a few nT offset in the X Rot data which could be caused by imperfect field nulling.*

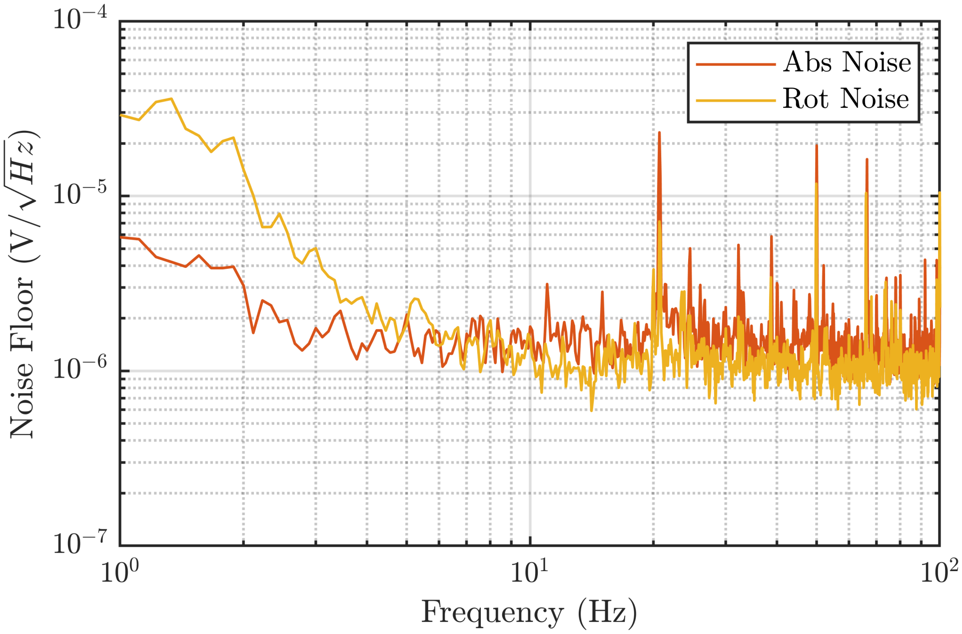

*Figure 6.2: Voltage noise floor detected by the photodiode of both the absorptive (orange) and optical rotation (yellow) based experiments. Below 5 Hz the absorptive experiment performs better with much less noise. From 10 Hz and above the optical rotation noise floor is lower, benefiting from the noise cancellation.*

## 6.3 Noise Floor

Noise floor measurements provide information about noise sources that limit the device's sensitivity as well as the frequency dependent noise sources. Fig 6.2 shows the demodulated data for both the absorptive and optical rotation experiments. The voltage noise floor of the absorptive setup is lower than that of the optical rotation in the low frequency regime up to around 5 Hz. It is likely that this is due to polarisation instability in the optical fibre delivering light to the experiment. The changing polarisation is turned into intensity noise going through the PBS in the optical rotation based setup which is not common mode on the balanced polarimeter. This drift in polarisation does not have as much of an effect on the absorptive setup as the small changes in polarisation does not have as pronounced an effect on the optical pumping [107]. Above 10 Hz the optical rotation experiment has a noise floor of roughly $1 \times 10^{-6}$ V/$\sqrt{\text{Hz}}$, while the absorptive experiment has a higher noise floor in the region of $1.5 \times 10^{-6}$ V/$\sqrt{\text{Hz}}$. It

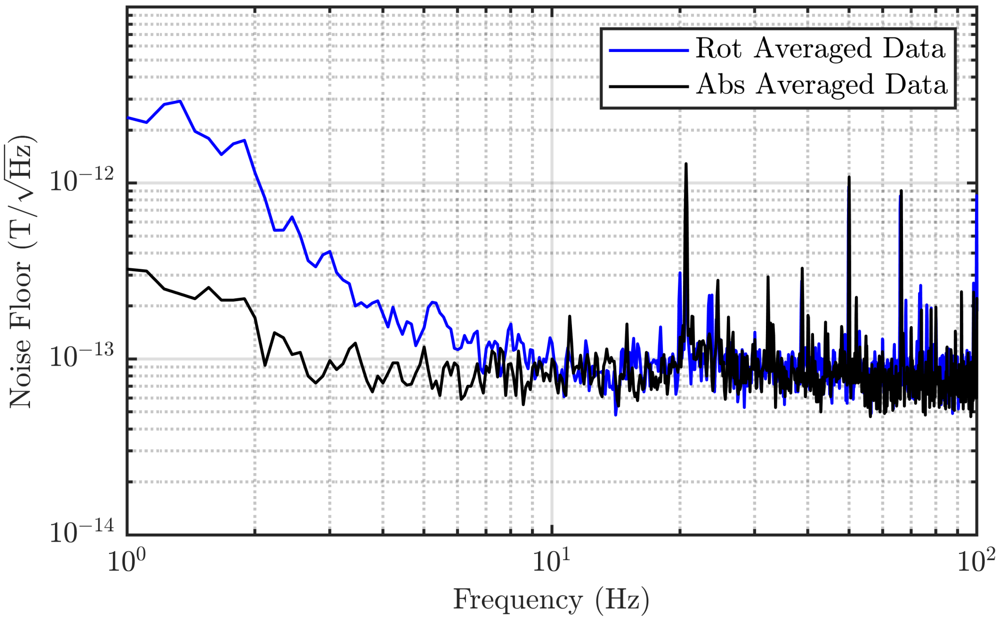

*Figure 6.3: Magnetic noise floor for both the absorptive (black) and optical rotation (blue) based experiments. Once Fig 6.2 has been scaled by the respective gradients of Fig 6.1 the magnetic noise floor is found. Both the absorption and polarisation rotation reach a magnetic noise floor of 70 fT/$\sqrt{Hz}$ after 10 Hz with the absorptive reaching the point at a lower frequency of 5 Hz.*

can also be seen that there are much larger spikes at 21, 25, 32 and 50 Hz, for example, in the absorptive data than the optical rotation. Both of these factors are likely due to the common mode cancellation of intensity noise in the balanced polarimeter.

Once the noise floors have been scaled by their respective mV/nT it is seen that they both achieve similar sensitivities of roughly 70 fT/$\sqrt{\text{Hz}}$ which is shown in Fig 6.3. The optical rotation has a lower overall noise floor in V/$\sqrt{\text{Hz}}$ but the conversion factor is lower than that of the absorptive data. Due to the large amount of low frequency noise in the optical rotation based measurement, only the absorptive will be discussed from here. When looking at MCG signals for instance the signal of interest has components spread across a range of frequencies up to around 50 Hz. Important information can be lost from the signal of interest if there is not sufficient sensitivity in the lower frequencies.

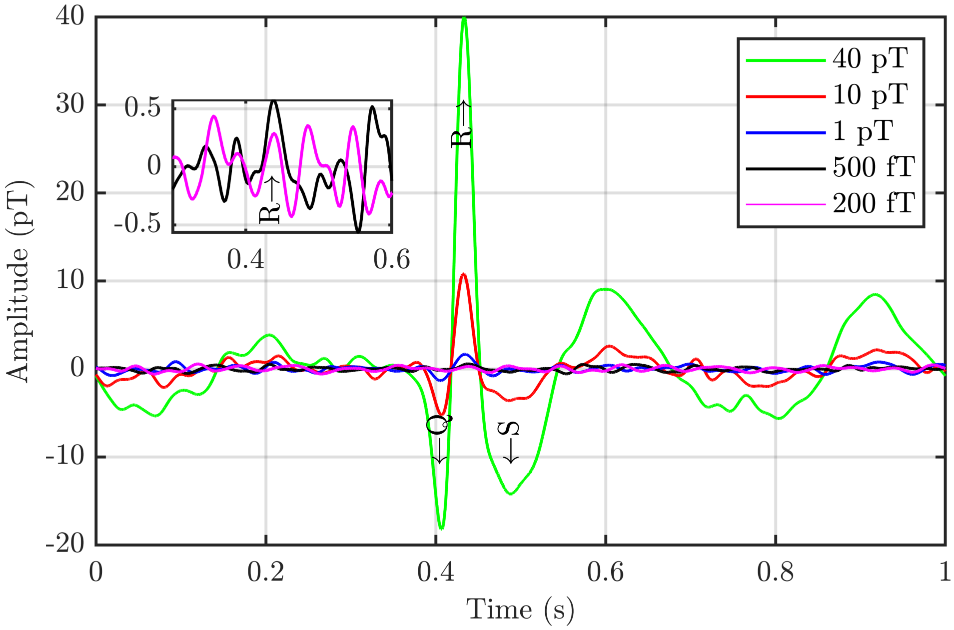

*Figure 6.4: Detected response from the sensor due to MCG signal applied via the test coil. The sensor can clearly pick up an MCG signal at a level produced by an adult human which can be as large as 100 pT. A signal with peak amplitude of 40 pT (green), 10 pT (red) and 1 pT (blue) have the QRS complex clearly visible. Below 1 pT only the main R component is visible shown in the insert which are shown using the left axis. The 40 pT trace is a close representation of the applied field.*

## 6.4 Analog MCG Signals in the Time Domain

When using SERF OPMs to measure MCG and MEG signals it is important be able to resolve the signal in the time domain for diagnostics. The reason for this is that the signals are not sharp single frequency features, but instead are spread across a range. A heartbeat for instance has components up to around 50 Hz making it hard to pick out clearly in the frequency domain. To replicate measuring a heartbeat in the real world a quick qualitative experiment was carried out by using a heartbeat that was recorded in an MSR at the University of Nottingham, which is then re-applied through the test coil inside the shield [87]. The data is demodulated at the carrier frequency leaving the test signal visible in the time domain. For the purposes of this experiment a filter range of 2 Hz - 40 Hz was chosen to omit the large mains frequency component at 50 Hz and the slow changes introduced through the optical fibre. It is clearly shown in

Fig 6.4 that the QRS complex (marked as Q, R and S) is visible. In these signals the R component of the QRS complex was applied at the field magnitudes shown in the legend of Fig 6.4 and discussed here. Signals larger than 1 pT were not averaged and visible with just one application via the test coil. Signals below the 1 pT level were averaged to remove random noise from the signal. For the traces where the R component had a field magnitude of less than 1 pT, only the R component can be distinguished in the time domain trace and shown in the insert. The Q, S and other components begin to get lost below this field value as their magnitudes are a fraction of the peak R component. The components either side of the QRS complex are also low frequency components, as has already been discussed the sensitivity decreases slightly below 5 Hz, which could also hide the slower components at smaller application amplitudes.

Using an equivalent portable sensor a heartbeat measured close to the chest would have an amplitude in the region of 100 pT making this senor more than sufficient to measure the signal [108]. Fetal magnetocardiography signals are much smaller than adults, in the single pT range [37]. A sensor with this performance would also be suitable for such applications.

## 6.5 Signals in the Frequency Domain

As has been discussed in the previous section, it is useful to look at some signals in the time domain. However, to measure the response of the sensor it is better to look at well defined frequencies at known amplitudes.

In order to be able to distinguish single frequencies at much smaller amplitudes the data is averaged. This is done by recording 10 s of data and processing this as discussed in Section 2.11 to retrieve the NSD from the time series data. Here 20 of these measurements are performed and the NSDs are averaged. This process reduces the random noise in the system leaving the repeatable frequencies as sharp features. Increasing the time that data is acquired for in each measurement increases

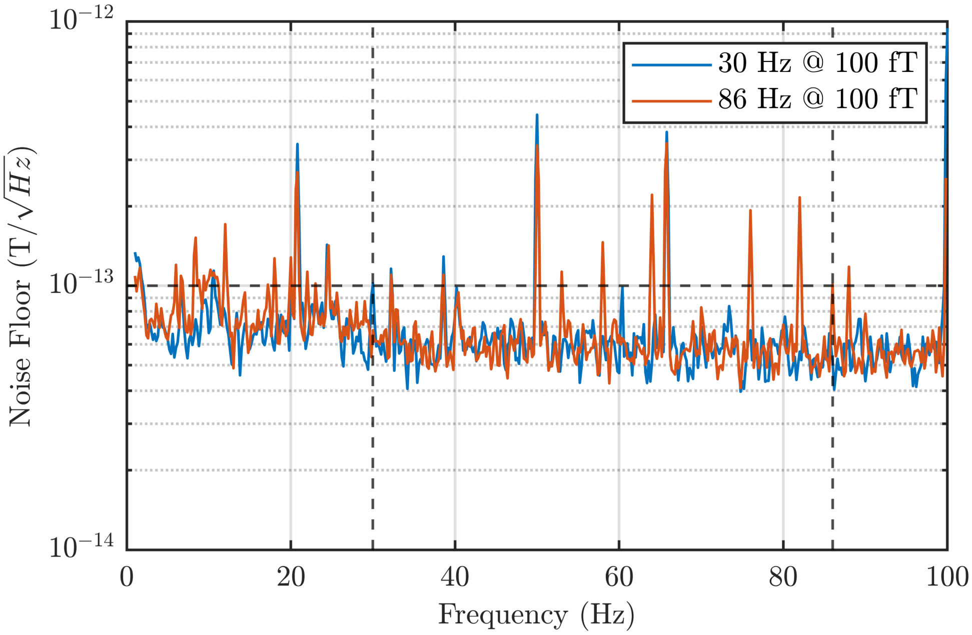

*Figure 6.5: Magnetic modulations at discrete frequencies were applied to be able to resolve them close to the noise floor. 100 fT signals were applied at 30 Hz (blue) and separately at 86 Hz (red). There are additional noise components in the 86 Hz trace which do not appear in the 30 Hz trace. The source of these signals appearing in only this one trace are unknown.*

the resolution in the frequency domain. This allows narrower features to be more easily separated from surrounding peaks.

In Fig 6.5 magnetic modulations were individually applied through the test coil at frequencies of 30 and 86 Hz both with an amplitude of 100 fT. These frequencies have been chosen as they were regions where there was little noise and avoid the larger features such as 21 Hz, 50 Hz and 65 Hz, as well as an amplitude where the signal would be able to be resolved just above the noise floor. The source of a lot of these spikes is unknown except for 50 Hz which is produced by the mains. Both of the applied signals are visible in their own trace and not visible in the others showing that it is not noise in the system.

## 6.6 Bandwidth

It is important to discuss the bandwidth along with the sensitivity. The bandwidth of a sensor typically follows a low-pass filter response. The bandwidth shows the frequency response of the sensor by showing the point at which the amplitude of a given, or a test signal, reaches -3 dB or $1/\sqrt{2}$. To find the -3 dB point a secondary magnetic modulation is applied via the test coil at a changing frequency. The frequency was stepped exponentially so not to have too many data points in the higher frequencies and rounded to integer values. The data is demodulated first of all at the carrier frequency and then at the test coil frequency. This allows for the amplitude of the test coil frequency in each application to be recovered. To determine the -3 dB point a transfer function is used to fit to the amplitude already retrieved [109, 110]. This allows for two regions to be determined. The first of which is the region of in-band frequencies. These are frequencies lower than the -3 dB point. There are also the out-of-band frequencies, which are frequencies higher than the -3 dB point. What these two regions refer to are frequencies that the sensor has a flat response (in-band) and a diminishing response (out-of-band). These can be seen in Fig 6.6.

The solid line in Fig 6.6 represents the raw data while the dashed line shows the transfer function fit and the asterisk the -3 dB point. As the raw data starts to roll-off it's clear that it deviates from the fit transfer function. The reason for this, as was discussed in Sections 4.3 and 5.4, in-band modulation is used as the carrier frequency. As the test frequency approaches the modulation frequency side-bands are created distorting the demodulated amplitude. On average, the -3 dB point is 1.55 times larger than the HWHM of the magnetic resonance, providing a scaling factor from HWHM to bandwidth.

The sensor's optimal operating parameters produce a 1D resonance with a HWHM of 40 nT, as seen in Fig 6.1. By scaling this in the same manner as the data in Fig 6.6, there is a bandwidth of 420 Hz. This is nearly three times higher

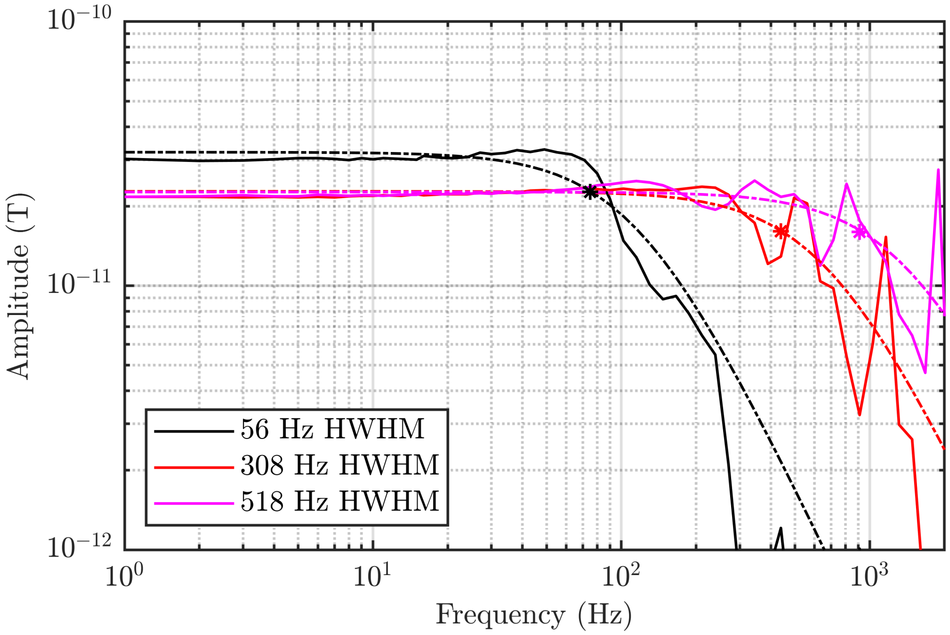

*Figure 6.6: The bandwidth of the sensor has been measured for varying magnetic linewidth. The solid line in each data set shows the experimental data while the dashed line shows the transfer function fit. The asterisk indicates the -3 dB point for each set. The -3 dB point is on average 1.55 times the value of the HWHM across the three data sets.*

than some commercially available sensors on the market today and allows for sensitive measurements up to 420 Hz [111]. Some MEG motor cortex signals can be as high as 200 Hz - 300 Hz showing where a large bandwidth SERF magnetometer could perform well.

## 6.7 Limitations

A big limitation for the sensitivity is the technical noise created by the photodiode and the DAQ. The sample rate used for the DAQ in all data to this point was 100 kHz. This was chosen to reduce the amount of data being processed, as well as the fact that it is a sufficiently high sample rate that satisfies the Nyquist limit of the signals of interest in the 1 Hz - 100 Hz band. By increasing the sampling frequency the resolution at which data can be read is increased, allowing the noise floor to reduce. Working near

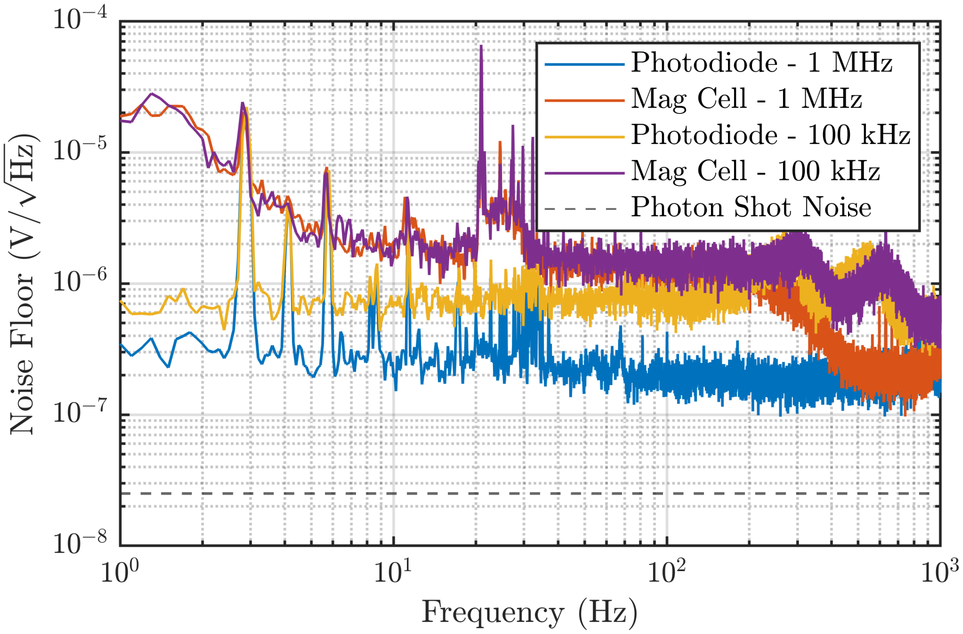

*Figure 6.7: Photodiode and laser noise comparison for increasing DAQ sampling rate. By sampling at 100 kHz the noise is limited to* $1\times10^{-6}$ $V/\sqrt{Hz}$. *By increasing this to 1 MHz sampling rate the noise floor drops by nearly an order of magnitude to* $2\times10^{-7}$ $V/\sqrt{Hz}$ *at the modulation frequency in the 500 Hz region. The photon shot noise is estimated to be* $2.5\times10^{-8}$ $V/\sqrt{Hz}$.

the DAQ limit of 1 MHz sample rate the reduction in noise is on the scale of nearly an order of magnitude as can been seen in Fig 6.7. The photodiode noise is captured by covering the diode so there is no light incident on it. The laser noise is measured on the same photodiode by removing the magnetometry cell so there are no obstructions. The magnetometry cell is then placed back in the shield and the noise is measured again. Taking a specific example, it can be seen that changing the DAQ sample rate has a significant effect on the noise at 500 Hz. This limitation is caused here as the optical noise of the laser meets the DAQ noise floor. This is also where the modulation is carried out indicating that the sensitivity is limited by the DAQ noise floor. The photon shot noise is estimated, using Eq 2.60, to be nearly an order of magnitude below the DAQ noise at 1 MHz. Using the same mV/nT on-resonance gradient from the absorptive demodulated data this would achieve a fundamental sensitivity of 1 fT/$\sqrt{\text{Hz}}$.

Carrying out a similar measurement as in Section 6.5, but at 1 MHz sampling rate, Fig 6.8 shows a increased sensitivity going from 70 fT/$\sqrt{\text{Hz}}$ to roughly 35 fT/$\sqrt{\text{Hz}}$. Signals at 30 Hz and 86 Hz were applied again at 100 fT which can be seen in each of the individual traces. The peaks at 21 Hz, 50 Hz and 65 Hz for instance appear in both traces again and are due to environmental and technical noise. Due to the increased amount of data LabVIEW would crash after four, 10 s measurements. In order to get around this, live averaging was introduced so not to fill LabVIEW's memory.

In this chapter the sensitivity of a rubidium SERF magnetometer has been explored. The comparison between the two previously discussed experimental setups of absorptive and optical rotation have been compared. The optical rotation based setup was more susceptible to low frequency noise caused by the laser polarisation instability leading to increased low frequency noise which in turn leads to it being ruled out as a viable option in the end. The DAQ noise was the limiting factor in the experiment still at

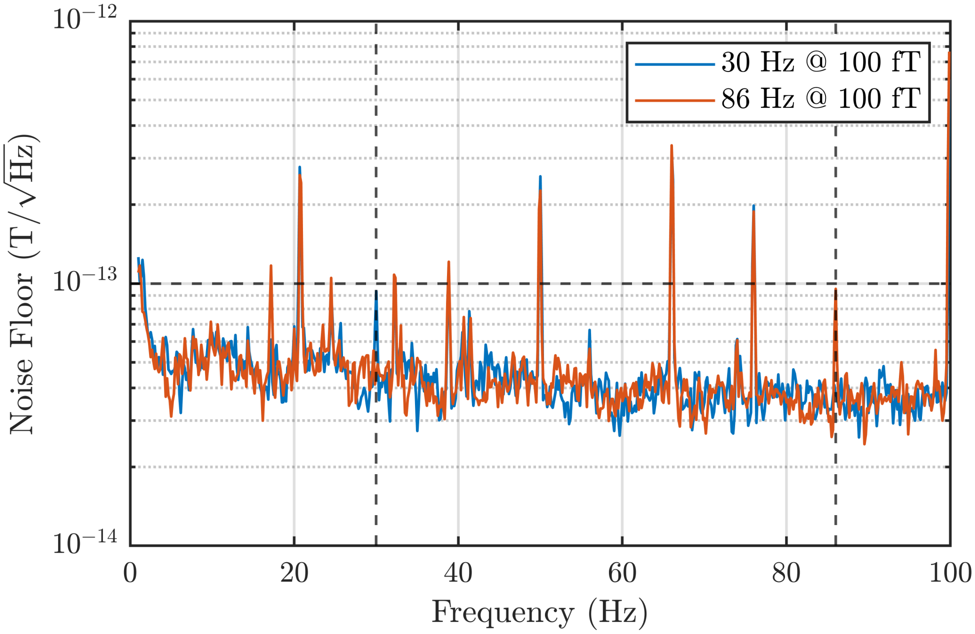

*Figure 6.8: Modulation at discrete frequencies were applied to be able to resolve them close to the noise floor. Differing from Fig 6.5 where a sampling frequency of 100 kHz was used, a sampling frequency of 1 MHz has been used to record the data here. Signals with amplitude of 100 fT were applied at 30 Hz (blue) and separately at 86 Hz (red).*

this point. Increasing the sampling rate from 100 kHz to 1 MHz helped this issue but did not eliminate it completely. It is thought that by increasing the DAQ from a 16 to 18-bit device would resolve this limitation. The increased performance provided by the extra 2-bits would reduce the noise floor below what is currently achieved. Had the DAQ noise limitation been able to be removed it is suspected that the next noise floor would be due to the Johnson noise of the shield. With the current experimental setup described a sensitivity of 35 fT/$\sqrt{\text{Hz}}$ was achieved.

# Chapter 7

# Conclusion

## 7.1 Discussion

This thesis has discussed the design, building and testing of a rubidium SERF magnetometer. The purpose of this work was to increase understanding of SERF systems within the research group and learn new techniques so they can be translated to a smaller, more portable sensor designed for biomedical applications. Here the key takeaway concepts will be outlined.

The theory behind OPMs and SERF OPMs has been discussed. Models of certain aspects of the theory have been created which align with what is seen experimentally. This includes optical lineshapes, light shift and power broadening. The effect the lineshapes have on optical pumping is also explored through population movement based on rate equations. Modelling this behaviour helped understand the sensor's behaviour when detuned to different regions.

Magnetic linewidth theory was also explored. The magnetic linewidth differs from the optical linewidth as it is not broadened by excited state interactions, only those from the ground state. The concepts of spin destruction and spin exchange are discussed and how they influence the magnetic linewidth. Techniques can be used to help narrow the linewidth such as entering the SERF regime where the contribution of spin exchange collisions is negated by increasing the collision rate far beyond the Larmor frequency. The use of additional gases such as a buffer gas can also be used to help reduce the frequency of depolarising wall collisions. Using the collision rates discussed in Section 2.7, intrinsic linewidths can be calculated where a nitrogen buffer gas pressure in the region of 200 Torr with enriched rubidium performed well, informing the selection when purchasing the magnetometry cell.

Two different detection methods were utilised in this thesis for comparison. These were a single photodetector with circular polarised light to measure absorption and a balanced polarimeter with elliptically polarised light to measure optical rotation. The single photodetector makes for a simplified setup while the balanced polarimeter offers common mode noise suppression. For each technique different operational parameters were explored. The absorption detection scheme was used to explore the effect of changing laser power and detuning as well as magnetometry cell temperature on the magnetic linewidth. While for the balanced polarimeter it was the effect the same changes have on the amount of optical rotation that is measured. Finding the balance between these three parameters for the most sensitive combination can be a time consuming process. The common mode noise suppression provided by the balanced polarimeter has an appealing advantage. This could be taken better advantage of by increasing the mV/nT to at least match that of the absorption setup. This could be done by having a separate circularly polarised pumping beam with a linear probe for optical rotation. The extra beam does not lend itself to miniaturisation, but could be explored.

For the absorption based experiment the optimal parameters were found to be 7 mW, 6 GHz and 150°C and for the optical rotation based experiment they were 6 mW, 8 GHz and 155°C. The absorption experiment needs to be close to resonance to optically pump the atoms while still having enough light left to pass through the magnetometry cell for detection. The optical rotation experiment needs sufficient light to both optically pump the atoms as well as exhibit optical rotation. The amount of rotation achieved drops off slower than the decrease in absorption with respect to the detuning, this allows the sensor to be run at higher temperatures while further detuned. The magnetic modulation parameters also need to be considered. For the absorption experiment these were a factor of 0.7 of the HWHM for amplitude and 1.2 for frequency and for the optical rotation method 0.3 for the amplitude and 0.7 for frequency. The reason for the discrepancy in these values is that the optical rotation produces much larger resonances as it is based on circular birefringence rather than absorption. As the resonances are larger, the scale of the HWHM to operate in a low noise region of the laser is lower, as shown in Fig 6.7 where this region is around 500 Hz.

The sensitivity comparison between the two methods is the deciding factor on whether they are suitable for the application or not. Each of the methods reached a sensitivity of 70 fT/$\sqrt{\text{Hz}}$. However, the optical rotation setup was more susceptible to low frequency instabilities in the laser. These instabilities are in the polarisation of the light that is converted into intensity noise at the balanced polarimeter, which is not common mode. The issue of laser instability can be overcome with either the use of noise suppression in the form of a PBS and an acousto-optic modulator or ideally a laser with improved amplitude and polarisation noise. The absorption based experiment was not as affected by these polarisation changes. In the absorption configuration the experiment was able to clearly detect synthetic heartbeat signals at a variety of amplitudes in the time domain as well as resolve low amplitude signals on the order of 100 fT in the frequency domain.

Increasing the DAQ sampling rate from 100 kHz to 1 MHz was found to improve the sensitivity further. This improved the sensitivity from 70 fT/$\sqrt{\text{Hz}}$ to 35 fT/$\sqrt{\text{Hz}}$. At this point the experiment was still limited by the noise floor of the DAQ.

Time was also a limiting factor during this thesis. Due to multiple lockdowns caused by the global pandemic, nine months of this thesis was highly disrupted, with access to the lab limited during the majority of that time. As the limiting noise source in the experiment has been identified the logical next step would be to replace the current DAQ with an improved performance DAQ. A new 18-bit DAQ had been ordered but did not arrive in time to complete the work as a result of the microchip shortage, a knock-on effect of the pandemic. The photon shot noise sensitivity of the sensor is estimated to be in the region of 1 fT/$\sqrt{\text{Hz}}$, a limiting factor before this is reached would be the Johnson noise provided by the shield which is on the scale of 10 fT/$\sqrt{\text{Hz}}$ when using a conventional magnetic shield as has been used here [112, 113]. This limit can also be surpassed by the use of a ferrite layer in the shield or gradiometry to provide further common mode noise suppression.

## 7.2 Post-Completion

After the completion of this thesis, using the conclusions drawn, improvements to the rubidium experimental setup were implemented. Changes were made to resolve known issues in the hardware to help increase the magnetometer's sensitivity. The changes made will be discussed briefly.

### 7.2.1 Shield Change

The shield used in the experimental work discussed in this thesis was a high aspect ratio, custom built magnetic shield as discussed in Section 3.2. It was suspected that the inner layers were not supported enough along the length of the shield, and this led to vibrations being introduced in to the experiment. The vibrations were discovered to come from the shield when analysing the noise of the system in different configurations. The noise from the detector was measured in the case where there was no light (detector and DAQ noise), then again when the light was passing through the shield with no magnetometry cell and then with the magnetometry cell in place. The noise appears as large features in the PSD between 5 and 40 Hz when the cell is put in place with the light passing through it and is visible in Fig 6.7.

After the work in this thesis was finished, a new, shorter TwinLeaf MS-L1 shield became available in the group. The experiment was kept in the same configuration as previously discussed but the shield was swapped with the new TwinLeaf shield. This swap would allow the theory of the shield introducing vibrations to be tested. The new TwinLeaf shield will have a lower shielding factor than that of the larger aspect ratio shield, but with the new shield having cage mounted optics attached to the shield's outer layer, hard plastic spacers between the shield layers and an internal breadboard for mounting the magnetometry cell and coils means there will be a reduction in the vibrations in the system.

### 7.2.2 Pre-amplification

It was discovered when setting the DAQ input voltage limits that as the range decreases the relative noise performance of the DAQ decreases. When operating at ±10 V the DAQ has random noise of 281 $\mu$V, so by operating in the ±1 V a random noise of 28.1 $\mu$V would be assumed. However, this is not the case, when operating at ±1 V the random noise is 35 $\mu$V, which is 1.25 times larger relatively than that of the ±10 V [114]. These data are shown in Appendix D. Following this trend of increasing relative noise in the smaller DAQ ranges, when operating at ±0.5 V, such as in Section 6.2, the random noise is 26 $\mu$V which is 1.85 times larger relatively compared to the full ±10 V range. By adding the pre-amplifier, the signal is then able to fill the full ±10 V, benefiting from the noise taking up less of the range. The drawback to amplification is that when pre-amplifying the signal, noise will also be amplified. However, the amplified noise is outweighed by the extra bits made available due to the relatively reduced noise floor.

### 7.2.3 Noise Subtraction

As has been mentioned, the laser introduces low-frequency noise due to the instability in the fibre. In order to reduce this, noise subtraction has been implemented. The experimental setup is the same architecture as discussed in Section 3.1, but with a 50/50 beam splitter before the light enters the shield. To keep the power entering the shield close to that in Section 4.5, the laser is now operating at 12 mW, providing 6 mW for the magnetometry cell. The reflected part of the beam is directed towards a reference pick-off photodiode. The pick-off photodiode and magnetometry photodiode are then recorded simultaneously. The signals from the two photodiodes are then subtracted before the subtracted data is processed in the same manner as described in Section 2.11. The process of subtracting the signals from the photodiodes allows for a large reduction in the 1/f noise. As there are low-frequency instabilities in the beam's power, the subtraction removes the common noise across the two diodes, similar to that discussed in Section 5.2.

### 7.2.4 Sensitivity Measurements

When combined, all the discussed improvements have a dramatic effect on the noise floor and this is shown in Fig 7.1. The data shown here has operating parameters of magnetometry cell temperature of 150°C, laser power of 6 mW and laser detuning of 6 GHz. These parameters match those found in Section 4.5, with exception of the power which has dropped by 1 mW. Each of the implemented changes has affected the result achieved significantly. Firstly, by changing the shield to the shorter TwinLeaf shield, the broad noise features across 6 Hz - 30 Hz, among others, are removed. This appears to be due to there being significantly reduced vibrations in the shields layers to a point where they are no longer detectable. Second, the pre-amplification allows for the magnitude of the signal being captured to be larger than the relatively lower random noise from the DAQ. A reduction in noise floor allows a sensor with the same

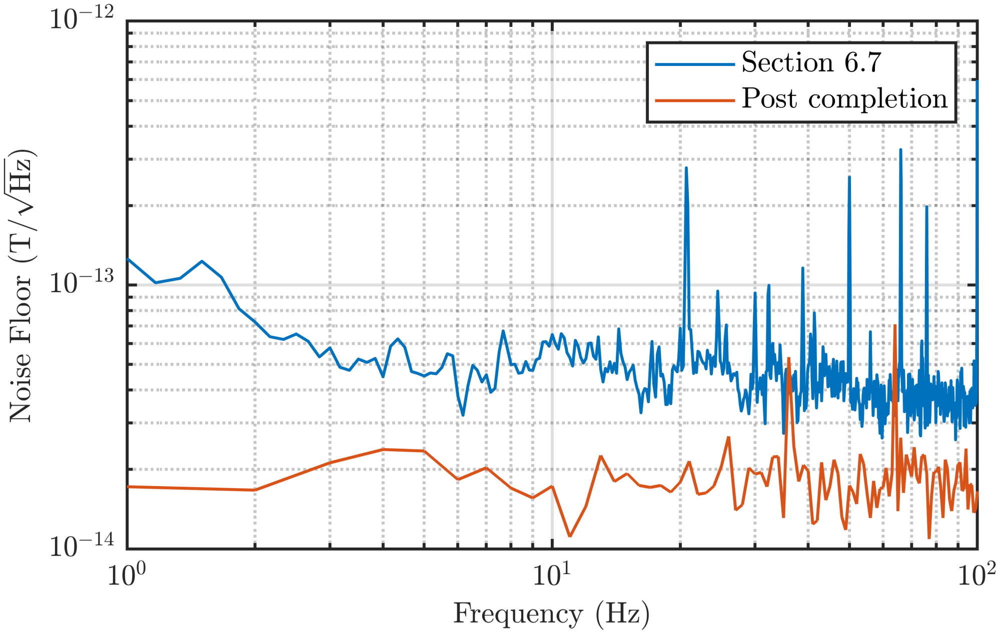

*Figure 7.1: A comparison of the data captured in Section 6.7 and after the changes made to the experiment were carried out. The new data is shown to have a drastic improvement with the noise floor now having fewer peaks and sensitivity below 20 fT/$\sqrt{Hz}$ across nearly the full 1 Hz - 100 Hz range.*

mV/nT to achieve a better sensitivity. Finally, the noise subtraction suppresses the the 1/f noise introduced by the laser's intensity instability through common mode noise suppression. The changes made have reduced the noise floor down to sub 20 fT/$\sqrt{\text{Hz}}$ in nearly the full 1 Hz - 100 Hz range, which is approaching the specified 16 fT/$\sqrt{\text{Hz}}$ Johnson noise of the TwinLeaf MS-L1 shield [113].

This thesis has contributed to the understanding of SERF systems within the group and been a valuable test bed to trial new materials, ideas and techniques to help achieve the goal of a portable sensor suitable for biomagnetic field detection. Although there were significant sources of noise remaining at the end of the experimental work described in the previous chapters, the work described in this thesis developed the experiment to a point where there was a clear roadmap for improvement. The work carried out in this chapter by colleagues within the group shows the potential of the experiment. The changes made to the experimental setup were simple and quick to execute once identified. With the changes made to overcome the limitations that are highlighted in this thesis, the sensitivity is vastly improved. The improvements have resulted in a rubidium spin exchange relaxation free magnetometer with a sensitivity of sub 20 $\mathrm{fT}/\sqrt{\mathrm{Hz}}$ across most of the 1 Hz - 100 Hz range.

# Appendix A

This Appendix contains figures relating to the probability of an electron occupying a particular Zeeman sublevel in the ground state of rubidium-87. Fig A1 is the $F = 1 \rightarrow F' = 1$ transition, Fig A2 is $F = 1 \rightarrow F' = 2$ and Fig A3 $F = 2 \rightarrow F' = 2$.

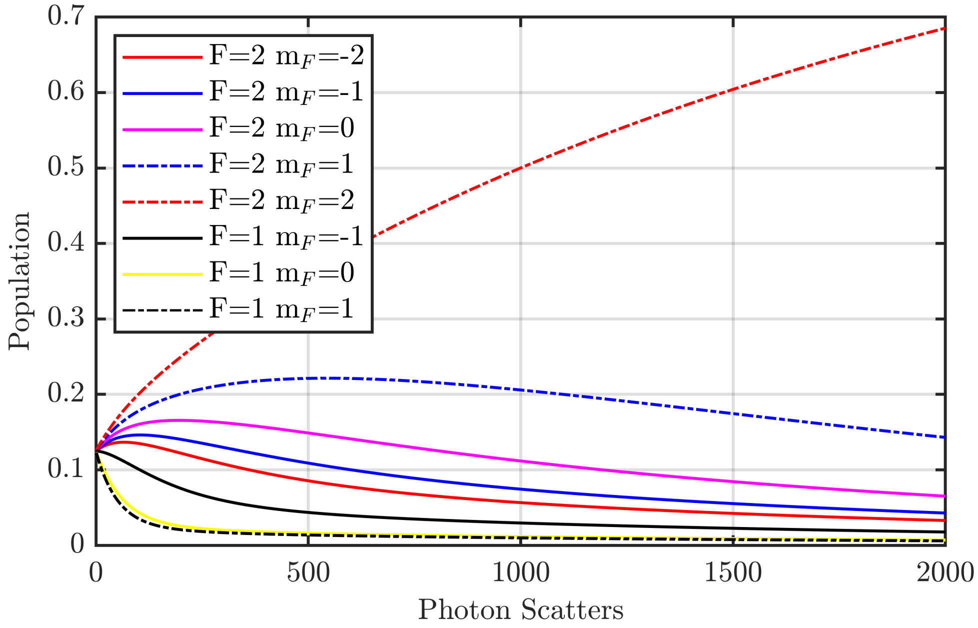

*Figure A1: Modelled population movement based on photon scatter for the F=1→F'=1 transition of* $^{87}$*Rb D1 line with 200 Torr of nitrogen quenching gas. Circularly polarised light has been assumed here with the population build up happening in the stretched state.*

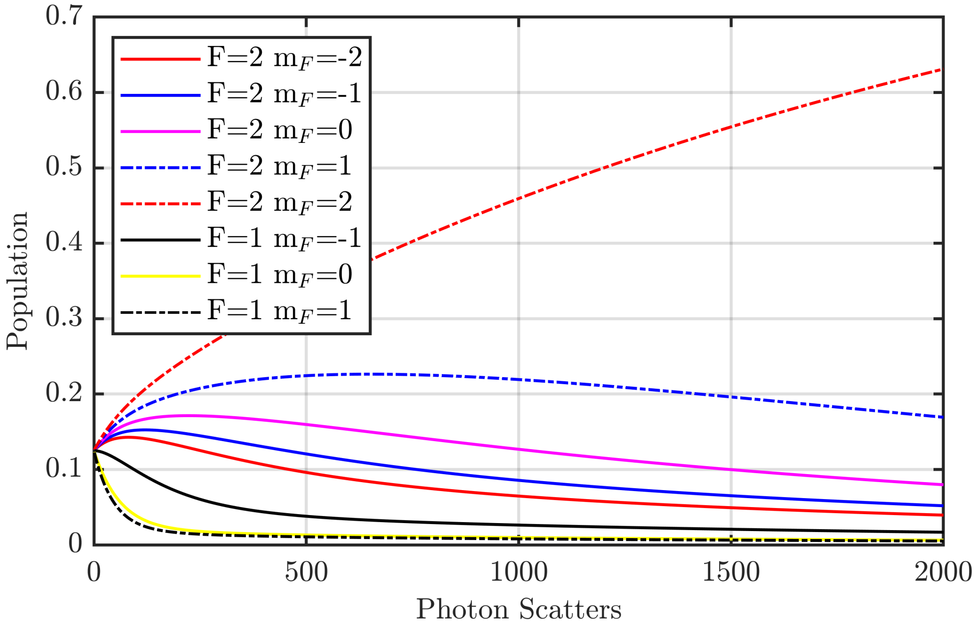

*Figure A2: Modelled population movement based on photon scatter for the F=1→F'=2 transition of $^{87}$Rb D1 line with 200 Torr of nitrogen quenching gas. Circularly polarised light has been assumed here with the population build up happening in the stretched state.*

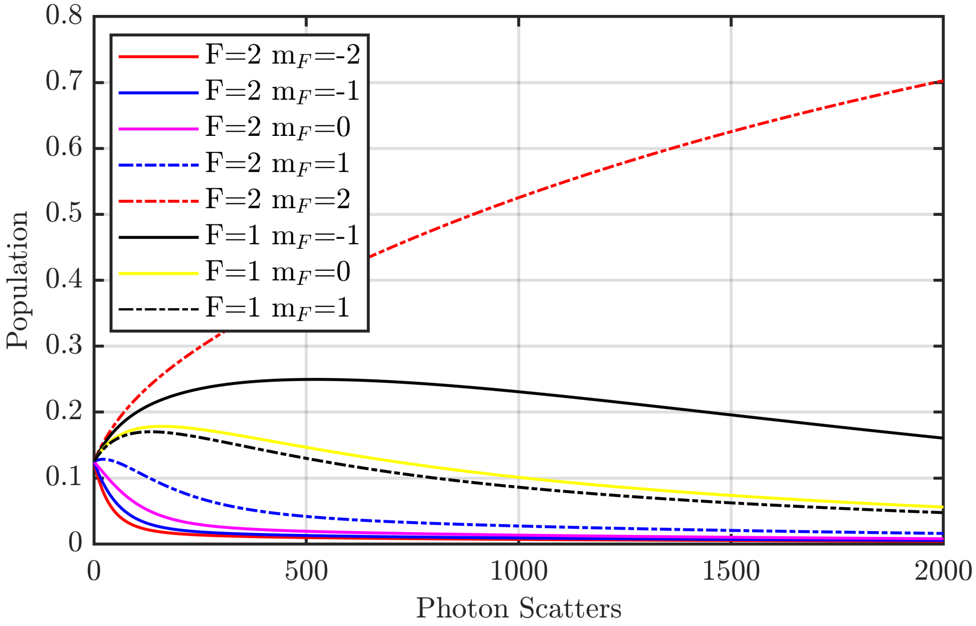

*Figure A3: Modelled population movement based on photon scatter for the F=2→F'=2 transition of $^{87}$Rb D1 line with 200 Torr of nitrogen quenching gas. Circularly polarised light has been assumed here with the population build up happening in the stretched state.*

# Appendix B

This Appendix contains calibration data for the laser in terms of characterising any mode hopes present as seen in Fig B1 and B2 and current to power calibration in Fig B3. The temperature of the magnetometry cell calibration is also shown here based on the phase of the square waves in Fig B4.

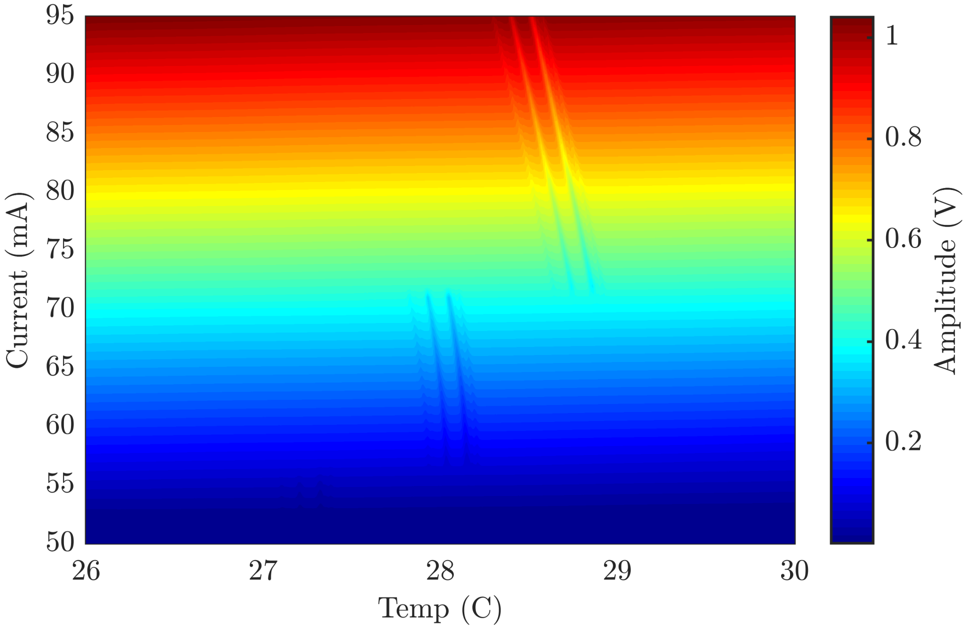

*Figure B1: The DBR laser spectroscopy performed on a reference cell with natural abundance rubidium. By changing the temperature of the thermo-electric cooler (TEC) the detuning of the laser is changed. This is repeated for each mA of current provided to the TEC changing the power. Mode hops in the laser can be accounted for by mapping this space.*

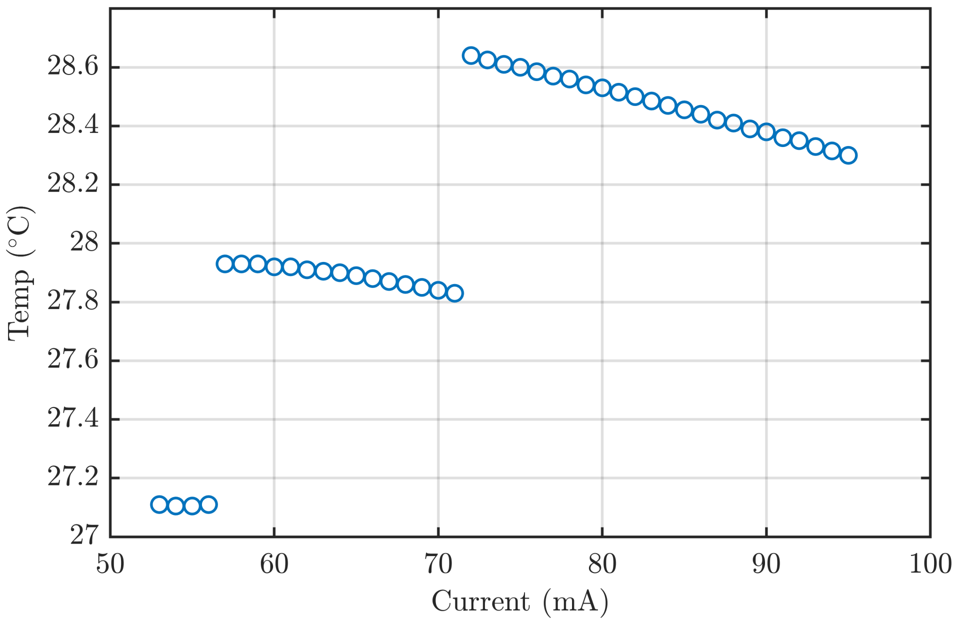

*Figure B2: Extracting the 0 GHz point ($^{87}$Rb F=1→F'=2) for increasing laser power from Fig B1. The mode hops are more clearly visualised here with two hops at 56 and 72 mA. Each of the mode hopped regions has a different fit. This data is used to set different temperature ranges for changing current so the laser's detuning is always calibrated to the reference cell 0 GHz.*

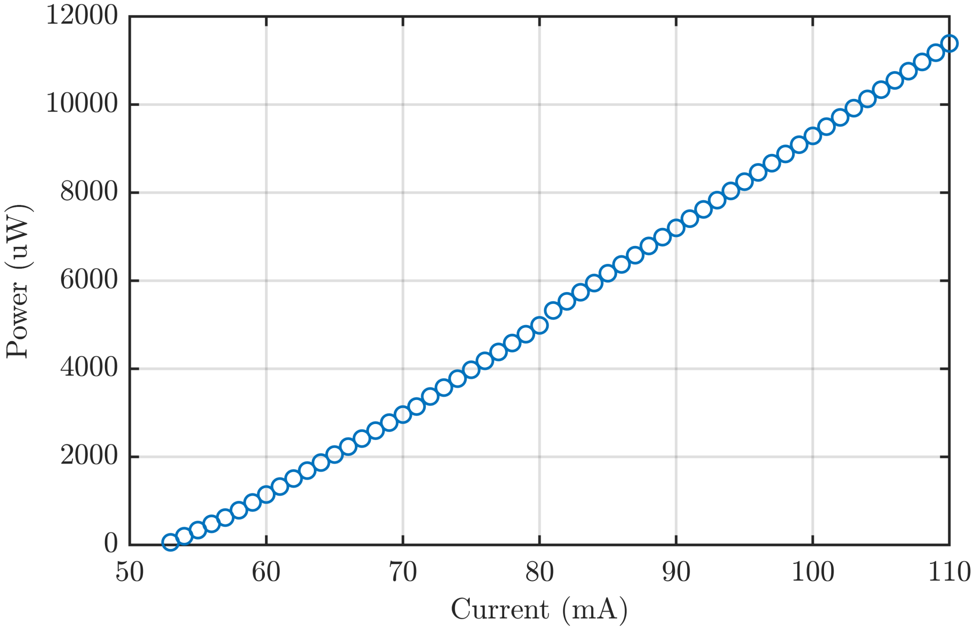

*Figure B3: Laser power measured by increasing the photodiode current of the TEC. A linear dependence can be seen for laser power with increasing current. The laser starts lasing at 54 mA.*

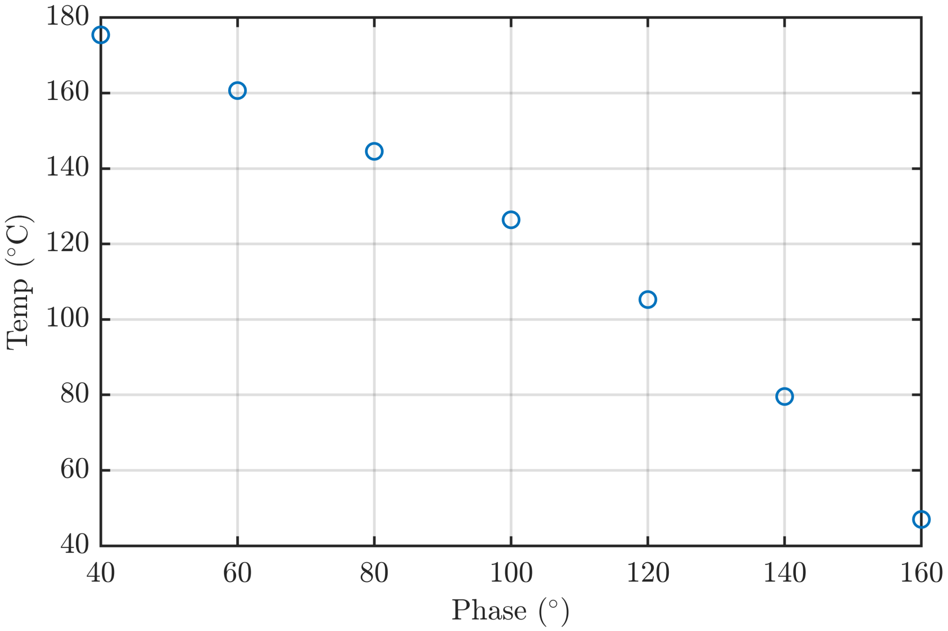

*Figure B4: Calibration of the magnetometry cell heater. The data follows a second degree polynomial fit where the cell is provided with very little heating at large phase offset of the square waves used for the heating. If the data is extrapolated to 0° phase a maximum cell temperature of just over 200° C can be reached.*

# Appendix C

Appendix C contains a complete set of data for a systematic scan. The data sets includes laser power and detuning slices in temperature ranging from 1 - 8 mW, -24 - 16 GHz and 130 - 170°C. Fig C1 shows the sensitivity for each point while Fig C2 shows the demodulated slope.

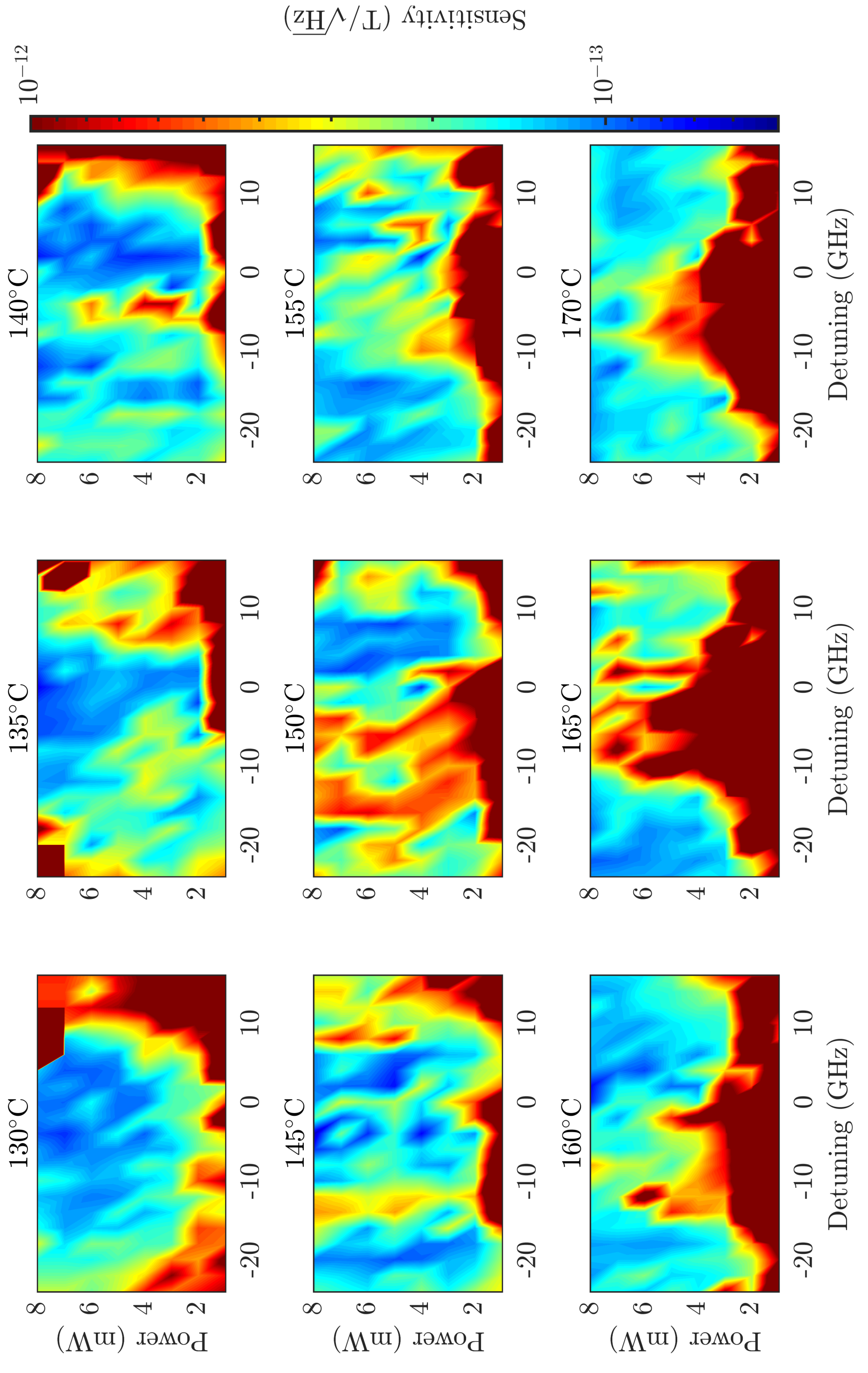

*Figure C1: Sensitivity plots for each temperature slice in a systematic scan ranging from 130° C - 170° C in 5° C steps. The power and detuning range from 1 mW- 8 mW and -24 GHz - 16 GHz respectively.*

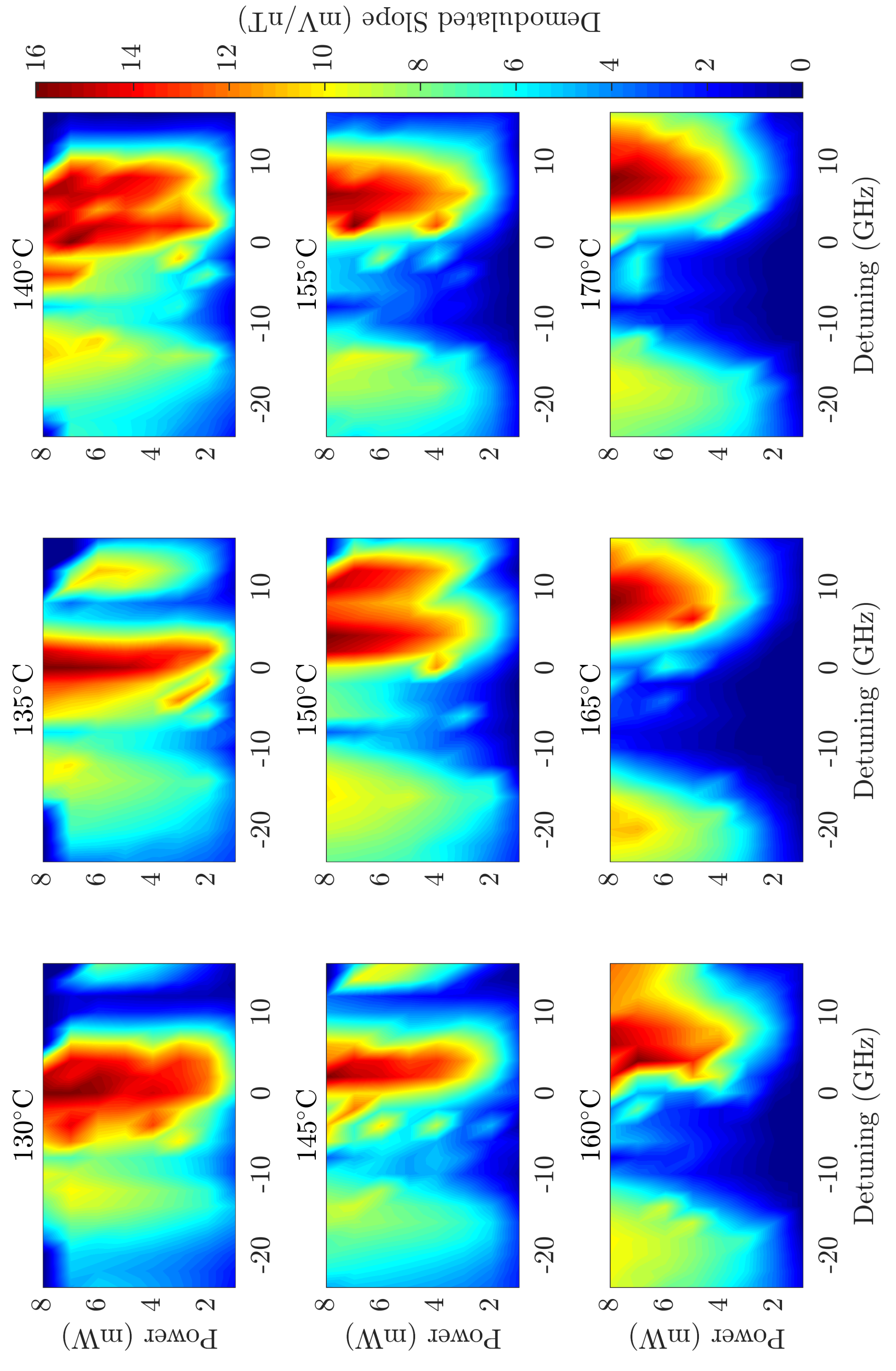

*Figure C2: Demodulated slope plots for each temperature slice in a systematic scan ranging from 130° C to 170° C in 5° C steps. The power and detuning range from 1 mW- 8 mW and -24 GHz - 16 GHz respectively.*

# Appendix D

Appendix D shows how the relative noise of the DAQ changes with selected input voltage range.

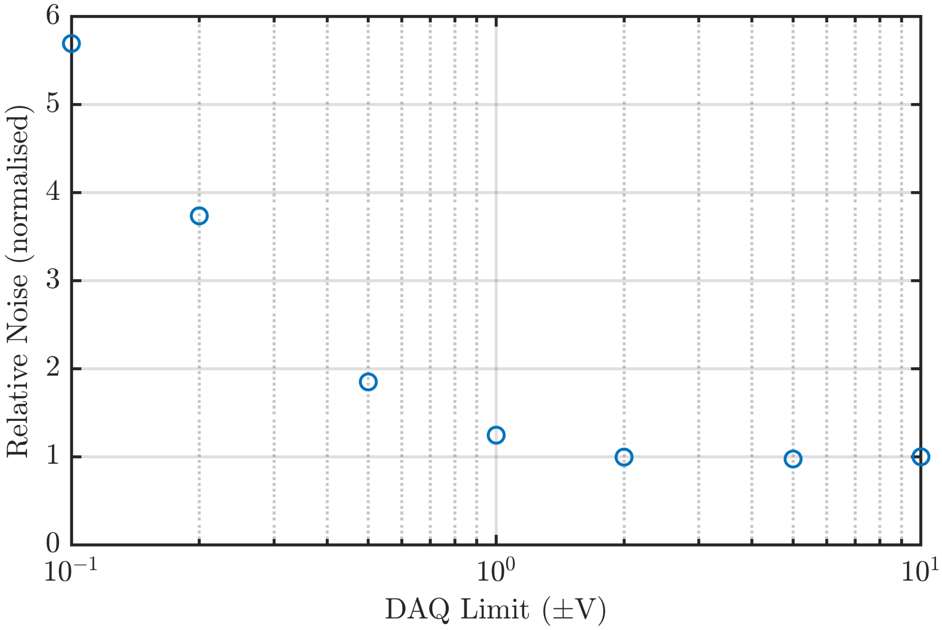

*Figure D1: Relative noise produced by the DAQ for changing voltage ranges. The noise is normalised to the full ±10 V range. It can be seen there is a sharp increase in the relative noise produced when the range is selected to be below ±2 V.*

# Bibliography

[1] Joseph L Kirschvink and James L Gould. Biogenic magnetite as a basis for magnetic field detection in animals. *Biosystems*, **13**(**3**):181–201, (1981).

[2] Massimo Guarnieri. Once upon a time... The compass. *IEEE Industrial Electronics Magazine*, **8**:60–63, (2014).

[3] William Gilbert. *De Magnete.* Courier Corporation, (1600).

[4] Kerry Kuehn. *A Student's Guide Through the Great Physics Texts: Volume III: Electricity, Magnetism and Light.* Springer, (2015).

[5] Carl Friedrich Gauss. The intensity of the Earth's magnetic force reduced to absolute measurement. *Royal Scientific Society*, **8**(**3**), (1832).

[6] Charles Augustin de Coulomb. Second mémoire sur l'Electricité et le Magnétisme. *Histoire de l'Académie Royale des Sciences*, pages 578–611, (1785).

[7] MC Oersted. Expériences sur l'effet du conflit électrique sur l'aiguille aimantée. **14**:417–425, (1820).

[8] Andre Marie Ampere. *D l'action mutuelle de 2 courans electriques; L'experiences relatives a de noveaux phenomenes electro-dinamiques.* (1821).

[9] Michael Faraday. On the forms and states assumed by fluids in contact with vibrating elastic surfaces. *Phil. Trans. R. Soc. Lond.*, **121**:319–340, (1831).

[10] James Clerk Maxwell. A dynamical theory of the electromagnetic field. *Philosophical Transactions of the Royal Society of London*, **155**:459–512, (1865).

[11] Michael Faraday. On the magnetization of light and the illumination of magnetic lines of force. *Philosophical Transactions of the Royal Society of London*, **136**:1–20, (1846).

[12] Pieter Zeeman. The effect of magnetisation on the nature of light emitted by a substance. *Nature*, **55**(**1424**):347, (1897).

[13] Pieter Zeeman. Light radiation in a magnetic field. *Nobel Prize Lecture*, (1903).

[14] Wilhelm Hanle. Über magnetische beeinflussung der polarisation der resonanzfluoreszenz. *Zeitschrift für Physik*, **30**(**1**):93–105, (1924).

[15] RW Wood. Selective reflexion, scattering and absorption by resonating gas molecules. *The London, Edinburgh, and Dublin Philosophical Magazine and Journal of Science*, **23**(**137**):689–714, (1912).

[16] Alfred Kastler. Les méthodes optiques d'orientation atomique et leurs applications. *J. Phys. Radium*, **11**(**6**):255–265, (1950).

[17] H. G. Dehmelt. Modulation of a light beam by precessing absorbing atoms. *Phys. Rev.*, **105**:1924–1925, (1957).

[18] William E. Bell and Arnold L. Bloom. Optical detection of magnetic resonance in alkali metal vapor. *Phys. Rev.*, **107**:1559–1565, (1957).

[19] William E Bell and Arnold L Bloom. Optically driven spin precession. *Phys. Rev. Lett.*, **6**(**6**):280, (1961).

[20] W. Happer and H. Tang. Spin-Exchange Shift and Narrowing of Magnetic Resonance Lines in Optically Pumped Alkali Vapors. *Phys. Rev. Lett.*, **31**:273–276, (1973).

[21] W. Happer and A. C. Tam. Effect of rapid spin exchange on the magnetic-resonance spectrum of alkali vapors. *Phys. Rev. A*, **16**:1877–1891, (1977).

[22] IK Kominis, TW Kornack, JC Allred, and Michael V Romalis. A subfemtotesla multichannel atomic magnetometer. *Nature*, **422(6932)**:596–599, (2003).

[23] HB Dang, Adam C Maloof, and Michael V Romalis. Ultrahigh sensitivity magnetic field and magnetization measurements with an atomic magnetometer. *Applied Physics Letters*, **97(15)**:151110, (2010).

[24] Elena Boto, Ryan M Hill, Molly Rea, Niall Holmes, Zelekha A Seedat, James Leggett, Vishal Shah, James Osborne, Richard Bowtell, and Matthew J Brookes. Measuring functional connectivity with wearable MEG. *NeuroImage*, **230**:117815, (2021).

[25] Ryan M Hill, Elena Boto, Niall Holmes, Caroline Hartley, Zelekha A Seedat, James Leggett, Gillian Roberts, Vishal Shah, Tim M Tierney, Mark W Woolrich, et al. A tool for functional brain imaging with lifespan compliance. *Nature Communications*, **10(1)**:1–11, (2019).

[26] Matti Hämäläinen, Riitta Hari, Risto J. Ilmoniemi, Jukka Knuutila, and Olli V. Lounasmaa. Magnetoencephalography—theory, instrumentation, and applications to noninvasive studies of the working human brain. *Rev. Mod. Phys.*, **65**:413–497, (1993).

[27] P Gloor, G Ball, and N Schaul. Brain lesions that produce delta waves in the EEG. *Neurology*, **27(4)**:326–326, (1977).

[28] Wolfgang Klimesch. EEG alpha and theta oscillations reflect cognitive and memory performance: A review and analysis. *Brain Research Reviews*, **29(2-3)**:169–195, (1999).

[29] Wolfgang Klimesch, Michael Doppelmayr, Harald Russegger, Thomas Pachinger, and J Schwaiger. Induced alpha band power changes in the human EEG and attention. *Neuroscience Letters*, **244**(**2**):73–76, (1998).

[30] Michal Teplan et al. Fundamentals of EEG measurement. *Measurement Science Review*, **2**(**2**):1–11, (2002).

[31] Catherine Tallon-Baudry and Olivier Bertrand. Oscillatory gamma activity in humans and its role in object representation. *Trends in Cognitive Sciences*, **3**(**4**):151–162, (1999).

[32] K Kamada, Y Ito, and T Kobayashi. Human MCG measurements with a high-sensitivity potassium atomic magnetometer. *Physiological measurement*, **33**(**6**):1063, (2012).

[33] David Cohen. Magnetoencephalography: evidence of magnetic fields produced by alpha-rhythm currents. *Science*, **161**(**3843**):784–786, (1968).

[34] David Cohen. Magnetoencephalography: detection of the brain's electrical activity with a superconducting magnetometer. *Science*, **175**(**4022**):664–666, (1972).

[35] R. C. Jaklevic, John Lambe, A. H. Silver, and J. E. Mercereau. Quantum interference effects in josephson tunneling. *Phys. Rev. Lett.*, **12**:159–160, (1964).

[36] Robert Wyllie, Matthew Kauer, GS Smetana, Ronald T Wakai, and Thad G Walker. Magnetocardiography with a modular spin-exchange relaxation-free atomic magnetometer array. *Physics in Medicine & Biology*, **57**(**9**):2619, (2012).

[37] Robert Wyllie, Matthew Kauer, Ronald T Wakai, and Thad G Walker. Optical magnetometer array for fetal magnetocardiography. *Optics Letters*, v37(**12**):2247–2249, (2012).

[38] Elena Boto, Sofie S Meyer, Vishal Shah, Orang Alem, Svenja Knappe, Peter Kruger, T Mark Fromhold, Mark Lim, Paul M Glover, Peter G Morris, et al. A new generation of magnetoencephalography: Room temperature measurements using optically-pumped magnetometers. *NeuroImage*, **149**:404–414, (2017).

[39] Savely G Karshenboim, Francesco S Pavone, F Bassani, M Inguscio, and Theo W Hänsch. *The hydrogen atom: Precision physics of simple atomic systems*. Springer, (2007).

[40] Igor I Sobelman. *Atomic spectra and radiative transitions*. Springer Science & Business Media, (1979).

[41] John Pritchard. Experimental Atomic & Quantum Optics, SUPA Graduate Class, (2018).

[42] Tim M Tierney, Niall Holmes, Stephanie Mellor, José David López, Gillian Roberts, Ryan M Hill, Elena Boto, James Leggett, Vishal Shah, Matthew J Brookes, et al. Optically pumped magnetometers: From quantum origins to multi-channel magnetoencephalography. *NeuroImage*, **199**:598–608, (2019).

[43] Christopher J Foot. *Atomic physics*. OUP Oxford, (2004).

[44] RW Parsons, VI Metchnik, and RJ Dyne. The collision broadening of spectral lines. *Australian Journal of Physics*, **21**(**1**):13–20, (1968).

[45] A Paul Alivisatos, AL Harris, NJ Levinos, ML Steigerwald, and LE Brus. Electronic states of semiconductor clusters: Homogeneous and inhomogeneous broadening of the optical spectrum. *The Journal of chemical physics*, **89**(**7**):4001–4011, (1988).

[46] Louis George Henyey. The doppler effect in resonance lines. *Proceedings of the National Academy of Sciences*, **26**(1):50–54, (1940).

[47] Xianglei Huang and Yuk Ling Yung. A common misunderstanding about the Voigt line profile. *Journal of the Atmospheric Sciences*, **61**(**13**):1630–1632, (2004).

[48] Louis Galatry. Simultaneous effect of Doppler and foreign gas broadening on spectral lines. *Phys. Rev.*, **122**(**4**):1218, (1961).

[49] Hoon Yu and Jai Seung Yoo. Spin polarization of 87Rb atoms with Xe gas and high-pressure buffer gas in a cubic cell. *AIP Advances*, **9**(**3**):035209, (2019).

[50] Jonathan Levine. A simplified calculation of power-broadened linewidths, with application to resonance ionization mass spectrometry. *Spectrochimica Acta Part B: Atomic Spectroscopy*, **69**:61–66, (2012).

[51] NV Vitanov, BW Shore, L Yatsenko, K Böhmer, T Halfmann, T Rickes, and K Bergmann. Power broadening revisited: theory and experiment. *Optics Communications*, **199**(**1-4**):117–126, (2001).

[52] Marcis Auzinsh, Dmitry Budker, and Simon Rochester. *Optically polarized atoms: Understanding light-atom interactions.* Oxford University Press, (2010).

[53] Xiaoxu Zhang, Xingqiao Ma, Yiping Chen, Qiongying Ren, and Hua Zhao. Numerical analysis of the optical pumping process coupled with 23Na D2 manifold modeled as a partially resolved hyperfine structure. *AIP Advances*, **10**(**4**):045333, (2020).

[54] AW Ali and HR Griem. Theory of resonance broadening of spectral lines by atom-atom impacts. *Phys. Rev.*, **140**(**4A**):A1044, (1965).

[55] Haotian Chi, Wei Quan, Junying Zhang, Lijiang Zhao, and Jiancheng Fang. Advances in anti-relaxation coatings of alkali-metal vapor cells. *Applied Surface Science*, **501**:143897, (2020).

[56] Ryuzo Kawabata, Kyoya Fukuda, and Akihiko Kandori. Optimized condition for buffer gas in optical-pumped magnetometer operated at room temperature. *Japanese Journal of Applied Physics*, **49**(**8R**):082401, (2010).

[57] Sheng Li, Jingbiao Chen, and Hong Guo. An investigation on radiation trapping and quenching in optically pumped atomic vapor cell. *IEEE Journal of Quantum Electronics*, **55**(**4**):1–5, (2019).

[58] Scott Jeffery Seltzer. *Developments in Alkali-Metal Atomic Magnetometers.* PhD thesis, Princeton University, (2008).

[59] Greg A Pitz, Douglas E Wertepny, and Glen P Perram. Pressure broadening and shift of the cesium D1 transition by the noble gases and $N_2$, $H_2$, HD, $D_2$, $CH_4$, $C_2H_6$, $CF_4$, and $^3$He. *Phys. Rev. A*, **80**(**6**):062718, (2009).

[60] Greg A Pitz, Andrew J Sandoval, Tiffany B Tafoya, Wade L Klennert, and David A Hostutler. Pressure broadening and shift of the rubidium D1 transition and potassium D2 transitions by various gases with comparison to other alkali rates. *Journal of Quantitative Spectroscopy and Radiative Transfer*, **140**:18–29, (2014).

[61] Wolfgang Demtröder. *Laser spectroscopy 1: Basic principles.* Springer, (2014).

[62] Matthew D Rotondaro and Glen P Perram. Collisional broadening and shift of the rubidium D1 and D2 lines ($5^2S_{12} \rightarrow 5^2P_{12}$, $5^2P_{32}$) by rare gases, $H_2$, $D_2$, $N_2$, $CH_4$ and $CF_4$. *Journal of Quantitative Spectroscopy and Radiative Transfer*, **57**(**4**):497–507, (1997).

[63] MV Romalis, E Miron, and GD Cates. Pressure broadening of Rb D1 and D2 lines by $^3$He, $^4$He, $N_2$, and Xe: Line cores and near wings. *Phys. Rev. A*, **56**(**6**):4569, (1997).

[64] Andrew Andalkar and RB Warrington. High-resolution measurement of the pressure broadening and shift of the Cs D1 and D2 lines by $N_2$ and He buffer gases. *Phys. Rev. A*, **65**(**3**):032708, (2002).

[65] BR Bulos, A Marshall, and W Happer. Light shifts due to real transitions in optically pumped alkali atoms. *Phys. Rev. A*, **4**(**1**):51, (1971).

[66] BS Mathur, H Tang, and W Happer. Light shifts in the alkali atoms. *Phys. Rev.*, **171**(**1**):11, (1968).

[67] Kate A Whittaker, James Keaveney, Ifan G Hughes, and Charles S Adams. Hilbert transform: Applications to atomic spectra. *Phys. Rev. A*, **91**(**3**):032513, (2015).

[68] Alfred Kastler. Displacement of energy levels of atoms by light. *JOSA*, **53**(**8**):902–910, (1963).

[69] Daniel A Steck. Rubidium-87 D line data. (2001).

[70] Daniel A Steck. Cesium D line data. (2003).

[71] TG Tiecke. *Properties of potassium.* PhD thesis, University of Amsterdam, (2010).

[72] S Appelt, A Ben-Amar Baranga, CJ Erickson, MV Romalis, AR Young, and W Happer. Theory of spin-exchange optical pumping of $^3$He and $^{129}$Xe. *Phys. Rev. A*, **58**(**2**):1412, (1998).

[73] Richard G Brewer. Study of atom—wall collisions by optical pumping. *The Journal of Chemical Physics*, **38**(**12**):3015–3020, (1963).

[74] H Warren Moos and Richard H Sands. Study of spin-exchange collisions in vapors of Rb85, Rb87, and Cs133 by paramagnetic resonance. *Phys. Rev.*, **135**(**3A**):A591, (1964).

[75] Hyatt M Gibbs and Robert J Hull. Spin-exchange cross sections for Rb87-Rb87 and Rb87-Cs133 collisions. *Phys. Rev.*, **153**(**1**):132, (1967).

[76] W Happer and H Tang. Spin-exchange shift and narrowing of magnetic resonance lines in optically pumped alkali vapors. *Phys. Rev. Lett.*, **31**(**5**):273, (1973).

[77] W Happer and AC Tam. Effect of rapid spin exchange on the magnetic-resonance spectrum of alkali vapors. *Phys. Rev. A*, **16**(**5**):1877, (1977).

[78] Giovanni Moruzzi and Franco Strumia. *The Hanle effect and level-crossing spectroscopy.* Springer Science & Business Media, (2013).

[79] Natasha Castagna and Antoine Weis. Measurement of longitudinal and transverse spin relaxation rates using the ground-state Hanle effect. *Phys. Rev. A*, **84**(**5**):053421, (2011).

[80] Mahmoud E Yousif. The Faraday effect explained. *IOSR J. of Appl Phys (IOSR-JAP), e-ISSN*, pages 2278–4861, (2017).

[81] V Shah and Michael V Romalis. Spin-exchange relaxation-free magnetometry using elliptically polarized light. *Phys. Rev. A*, **80**(**1**):013416, (2009).

[82] MathWorks. FFT to PSD Estimation. (2021).

[83] JN Qin, X Zhang, C Chen, and YZ Wang. Zero-crossing magnetic field modulation at high frequency for triaxial-vectorial serf atomic magnetometer. *arXiv preprint arXiv:2001.08994*, (2020).

[84] Mengmeng Wei, Wenbin Yu, Min Zhou, Wei Huang, Yuanxing Liu, and Xinye Xu. Three techniques for measuring the transverse relaxation time of cesium atoms. *AIP Advances*, **13**(**3**):035327, (2023).

[85] Carolyn O'Dwyer, Stuart J Ingleby, Iain C Chalmers, Paul F Griffin, and Erling Riis. A feed-forward measurement scheme for periodic noise suppression in atomic magnetometry. *Review of Scientific Instruments*, **91**(**4**):045103, (2020).

[86] Rachel Dawson. *Development of a Single Beam SERF Magnetometer using Caesium Atoms for Medical Applications.* PhD thesis, University of Strathclyde, (2023).

[87] R Dawson, C O'Dwyer, M S Mrozowski, E Irwin, J P McGilligan, D P Burt, D Hunter, S Ingleby, P F Griffin, and E Riis. Portable Single-Beam

Caesium Zero-Field Magnetometer for Biomagnetic Sensing. *Journal of Optical Microsystems*, **3**(**04**):044501, (2023).

[88] R Dawson, C O'Dwyer, E Irwin, M S Mrozowski, D Hunter, S Ingleby, E Riis, and P F Griffin. Automated Machine Learning Strategies for Multi-Parameter Optimisation of a Caesium-Based Portable Zero-Field Magnetometer. *Sensors*, **23**(**8**):4007, (2023).

[89] Marcin Mrozowski. *Systems Engineering for Optically Pumped Magnetometry.* PhD thesis, University of Strathclyde, (2023).

[90] Dmitry Budker and Michael Romalis. Optical magnetometry. *Nature physics*, **3**(**4**):227–234, (2007).

[91] Susannah Dickerson, Jason M Hogan, David MS Johnson, Tim Kovachy, Alex Sugarbaker, Sheng-wey Chiow, and Mark A Kasevich. A high-performance magnetic shield with large length-to-diameter ratio. *Review of Scientific Instruments*, **83**(**6**):065108, (2012).

[92] S-K Lee and MV Romalis. Calculation of magnetic field noise from high-permeability magnetic shields and conducting objects with simple geometry. *Journal of Applied Physics*, **103**(**8**):084904, (2008).

[93] Formlabs. Formlabs High Temp Resin Spec Sheet. (2021).

[94] Andres F Restrepo Alvarez, Edinson Franco-Mejia, and Carlos R Pinedo-Jaramillo. Study and analysis of magnetic field homogeneity of square and circular helmholtz coil pairs: A taylor series approximation. *2012 VI Andean Region International Conference*, pages 77–80, (2012).

[95] MS Mrozowski, IC Chalmers, SJ Ingleby, PF Griffin, and E Riis. Ultra-low noise, bi-polar, programmable current sources. *arXiv preprint arXiv:2207.10348*, (2022).

[96] Andrea Vilardi, Davide Tabarelli, Laura Botti, Andrea Bertoldi, and Leonardo Ricci. Measurement and modelling of enhanced absorption hanle effect resonances in 85Rb. *Journal of Physics B: Atomic, Molecular and Optical Physics*, **42**(**5**):055003, (2009).

[97] R Slocum and B Marton. Measurement of weak magnetic fields using zero-field parametric resonance in optically pumped he 4. *IEEE Transactions on Magnetics*, **9**(**3**):221–226, (1973).

[98] Yan Yin, Binquan Zhou, Yaxiang Wang, Mao Ye, Xiaolin Ning, Bangcheng Han, and Jiancheng Fang. The influence of modulated magnetic field on light absorption in serf atomic magnetometer. *Review of Scientific Instruments*, **93**(**1**):013001, (2022).

[99] Theo Scholtes, Stefan Woetzel, Rob IJsselsteijn, Volkmar Schultze, and Hans-Georg Meyer. Intrinsic relaxation rates of polarized Cs vapor in miniaturized cells. *Applied Physics B*, **117**:211–218, (2014).

[100] Yao Chen, Libo Zhao, Ning Zhang, Mingzhi Yu, Yintao Ma, Xiangguang Han, Man Zhao, Qijing Lin, Ping Yang, and Zhuangde Jiang. Single beam Cs-Ne SERF atomic magnetometer with the laser power differential method. *Optics Express*, **30**(**10**):16541–16552, (2022).

[101] Yangying Fu, Xiaohu Liu, and Jie Yuan. Light narrowing of cesium magnetic-resonance lines in a radio-frequency atomic magnetometer. *AIP Advances*, **9**(**1**):015304, (2019).

[102] New Focus. Large-Area Balanced Photoreceivers. (2020).

[103] Dmitry Budker, Wojciech Gawlik, DF Kimball, SM Rochester, VV Yashchuk, and A Weis. Resonant nonlinear magneto-optical effects in atoms. *Reviews of Modern Physics*, **74**(**4**):1153, (2002).

[104] Binbin Zhao, Junjian Tang, Hongying Yang, Lin Li, Yaohua Zhang, Ying Liu, and Yueyang Zhai. High-sensitivity pump–probe atomic magnetometer based on single fiber-coupled. *Optics & Laser Technology*, **159**:109025, (2023).

[105] K Pandey, CC Kwong, MS Pramod, and D Wilkowski. Linear and nonlinear magneto-optical rotation on the narrow strontium intercombination line. *Phys. Rev. A*, **93**(**5**):053428, (2016).

[106] Wojciech Gawlik and Szymon Pustelny. Nonlinear magneto-optical rotation magnetometers. *High Sensitivity Magnetometers*, **19**:425–450, (2017).

[107] SP Krzyzewski, AR Perry, V Gerginov, and S Knappe. Characterization of noise sources in a microfabricated single-beam zero-field optically-pumped magnetometer. *Journal of Applied Physics*, **126**(**4**):044504, (2019).

[108] S Morales, MC Corsi, W Fourcault, F Bertrand, G Cauffet, C Gobbo, F Alcouffe, F Lenouvel, M Le Prado, F Berger, et al. Magnetocardiography measurements with 4he vector optically pumped magnetometers at room temperature. *Physics in Medicine & Biology*, **62**(**18**):7267, (2017).

[109] Vishal K Shah and Ronald T Wakai. A compact, high performance atomic magnetometer for biomedical applications. *Physics in Medicine & Biology*, **58**(**22**):8153, (2013).

[110] Yaxiang Wang, Ge Jin, Junjian Tang, Weiyong Zhou, Bangcheng Han, BinQuan Zhou, and Tao Shi. Optimized gas pressure of an Rb vapor cell in a single-beam serf magnetometer. *Optics Express*, **30**(**1**):336–348, (2022).

[111] QuSpin. Quspin zero field magnetometer. (2024).

[112] JC Allred, RN Lyman, TW Kornack, and Michael V Romalis. High-sensitivity atomic magnetometer unaffected by spin-exchange relaxation. *Phys. Rev. Lett.*, **89**(**13**):130801, (2002).

[113] Twinleaf. Johnson Noise of Magnetic Shields. (2022).

[114] Nathional Instruments. PCIe-6353 and USB-6353 Specifications. (2022).